ISSN 2782-2192 (Print)
ISSN 2782-2206 (Online)

Journal of Advanced Materials and Technologies

J·A·M·T

Vol. 9, No. 1.
2024

TSTU Publishing

ISSN 2782-2192 (Print)
ISSN 2782-2206 (Online)
DOI: 10.17277/issn.2782-2192

Journal of Advanced Materials and Technologies

Vol. 9, No. 1.
2024

Том 9, № 1.
2024

16+

Journal of Advanced Materials and Technologies

Scientific Journal

"Journal of Advanced Materials and Technologies" is a peer-reviewed scientific journal of research in materials science and related issues in materials physics and mechanics.

"Journal of Advanced Materials and Technologies" publishes original articles, reviews, short reports written by both renowned scientists and young researchers that contribute to the development of modern materials science.

The journal promotes research and exchange of information in the field of theoretical and practical research into materials science, modeling of processes involved in the creation of new materials, including nanomaterials, their properties and application.

The journal papers and metadata are available at Chemical Abstracts, CAS (American Chemical Society), Google Scholar, WorldCat, ROAR (Registry of Open Access Repositories), OpenAIRE (OpenAIRE - Open Access Infrastructure for Research in Europe), BASE (Bielefeld Academic Search Engine), RePEc: Research Papers in Economics, EBSCO.

ISSN 2782-2192 (Print), ISSN 2782-2206 (Online)

Rename information	Advanced materials & technologies (2016-2021) Print ISSN 2414-4606, Online ISSN 2541-8513
The journal was founded	2016
Publication frequency	Quarterly
Founders	Tambov State Technical University (TSTU), Merzhanov Institute of Structural Macrokinetics and Materials Sciences of Russian Academy of Sciences (ISMAN)
Postal address	TSTU: Bld. 2, 106/5, Sovetskaya St., Tambov, 392000 ISMAN: 8, Academician Osipyan St., Moscow region, Chernogolovka, 142432
Editorial office address	Bld. 2, 106/5, Sovetskaya St., Tambov, 392000
Contacts	Phone + 7 4752 63 03 91; amt.journal@yandex.ru
Printing House	TSTU Publishing, 112A, Michurinskaya St., Tambov, 392032 Phone + 7 4752 63 03 91; + 7 4752 63 07 46
Website ***E-mail*** ***Phone***	http://amt.tstu.ru/ amt.journal@yandex.ru +7 4752 63 92 93
Subscription	The electronic version of the Journal is freely available on the journal's website, as well as in open access databases. The subscription index for the Journal printed version in the unified catalog "Press of Russia" is 80453
Editor-in-Chief	Mikhail I. Alymov, D. Sc. (Engineering), Professor, Corresponding Member of the Russian Academy of Sciences

Journal of Advanced Materials and Technologies

Научный журнал

«Journal of Advanced Materials and Technologies» – научный рецензируемый журнал, посвященный исследованиям в области материаловедения и примыкающих вопросов физики и механики материалов.

Журнал «Journal of Advanced Materials and Technologies» публикует оригинальные статьи, обзоры, краткие сообщения, содействующие развитию современной науки о материалах, подготовленные как известными учеными, так и молодыми специалистами.

Миссия журнала – обмен актуальной научной информацией в области теоретических и практических исследований и моделирования процессов, связанных с получением, определением свойств новых материалов, в том числе наноразмерных, и их применения.

Средство массовой информации периодическое печатное издание, журнал «Journal of Advanced Materials and Technologies» зарегистрировано Федеральной службой по надзору в сфере связи, информационных технологий и массовых коммуникаций. Регистрационный номер СМИ ПИ № ФС 77-74804 от 25.01.2019.

Журнал входит в перечень рецензируемых научных изданий (перечень ВАК Минобрнауки РФ) от 16 декабря 2021 г. по научным специальностям: 1.4.15 – Химия твердого тела; 2.6.6 – Нанотехнологии и наноматериалы; 2.6.13 – Процессы и аппараты химических технологий; 2.6.17 – Материаловедение.

Материалы журнала размещены в РИНЦ, Chemical Abstracts, CAS (American Chemical Society), Академия Google (Google Scholar), WorldCat, СОЦИОНЕТ, ROAR (Registry of Open Access Repositories), OpenAIRE (OpenAIRE - Open Access Infrastructure for Research in Europe), BASE (Bielefeld Academic Search Engine), RePEc: Research Papers in Economics, EBSCO.

ISSN 2782-2192 (Print), ISSN 2782-2206 (Online)

Сведения о переименовании	«Advanced materials & technologies» (2016–2021) Print ISSN 2414-4606, Online ISSN 2541-8513
Журнал основан	2016 г.
Периодичность	4 раза в год
Учредители	Федеральное государственное бюджетное образовательное учреждение высшего образования «Тамбовский государственный технический университет» (ФГБОУ ВО «ТГТУ»), Федеральное государственное бюджетное учреждение науки Институт структурной макрокинетики и проблем материаловедения им. А. Г. Мержанова Российской академии наук (ИСМАН)
Адреса учредителей	ФГБОУ ВО «ТГТУ»: 392000, Тамбовская область, г.о. город Тамбов, г. Тамбов, ул. Советская, д. 106/5, помещ. 2, ИСМАН: 142432, Московская область, г. Черноголовка, ул. Академика Осипьяна, д. 8
Адрес издателя	ФГБОУ ВО «ТГТУ»: 392000, Тамбовская область, г.о. город Тамбов, г. Тамбов, ул. Советская, д. 106/5, помещ. 2
Адрес редакции ***Контакты***	392000, Тамбовская область, г.о. город Тамбов, г. Тамбов, ул. Советская, д. 106/5, помещ. 2 Тел.: + 7 4752 63 03 91; amt.journal@yandex.ru
Адрес типографии	392032, Тамбовская обл., г. Тамбов, ул. Мичуринская, д. 112А Тел.: + 7 4752 63 03 91; + 7 4752 63 07 46
Сайт	http://amt.tstu.ru/
E-mail	amt.journal@yandex.ru
Телефон	+7 4752 63 92 93
Подписка	Подписку на печатную версию журнала можно оформить по объединенному каталогу «Пресса России». Подписной индекс – 80453
Главный редактор	Алымов Михаил Иванович, д. т. н., профессор, член-корреспондент РАН

EDITORS

СОВЕТ РЕДАКТОРОВ

CONTENTS

СОДЕРЖАНИЕ

Original papers
Nobelistics

УДК 06.068+657:616.43 DOI: 10.17277/jamt.2024.01.pp.008-011

Information flows in the human brain. Roger Guillemin is 100 years old

© Viacheslav M. Tyutyunnik[a,b]✉

[a] *Tambov State Technical University, Bld. 2, 106/5, Sovetskaya St., Tambov, 392000, Russian Federation,*
[b] *International Nobel Information Centre (INIC), 30-6, Pervomaiskaya Sq., Tambov, 392002, Russian Federation*

✉ vmtyutyunnik@gmail.com

Abstract: The paper presents brief biographical information for the 100th anniversary of Roger Guillemin, a distinguished American scientist who won the 1977 Nobel Prize in Physiology or Medicine. He shared half of the prize with Andrew W. Schally “for their discoveries concerning the peptide hormone production of the brain”; the other half went to Rosalyn S. Yalow “for the development of radioimmunoassays of peptide hormones”. The paper briefly describes the main scientific achievements of R. Guillemin in the development of neuroendocrinology. He isolated somatotropin (growth hormone), identified molecules of thyrotropin-releasing hormone thyreoliberin, which controls all thyroid functions, as well as dozens of other molecules from the hypothalamus. His research has led to the development of treatments for diseases ranging from infertility to pituitary tumors. With his discoveries of certain information flows in the human brain, he contributed to deciphering the code of human life. Guillemin's early training in the construction of radio receivers and transmitters was of great importance, and his serious experience with computers has led him to become one of the pioneers in digital painting. R. Guillemin retired from active scientific life only three years ago.

Keywords: Nobel Prize winner in physiology or medicine Roger Guillemin; human brain; neuroendocrinology; information flows.

For citation: Tyutyunnik VM. Information flows in the human brain. Roger Guillemin is 100 years old. *Journal of Advanced Materials and Technologies*. 2024;9(1):008-011. DOI: 10.17277/jamt.2024.01.pp.008-011

Информационные потоки в мозге человека. Роже Гиймену – 100 лет

© В. М. Тютюнник[a,b]✉

[a] *Тамбовский государственный технический университет,*
ул. Советская, 106/5, пом. 2, Тамбов, 392000, Российская Федерация,
[b] *Международный Информационный Нобелевский Центр (МИНЦ),*
Первомайская площадь, 30-6, Тамбов, 392002, Российская Федерация

✉ vmtyutyunnik@gmail.com

Аннотация: Представлены краткие биографические сведения к 100-летию выдающегося американского ученого, лауреата Нобелевской премии по физиологии или медицине 1977 года Роже Гиймена. Он разделил половину премии с Эндрю В. Шалли «за открытия, касающиеся производства пептидных гормонов в мозге», вторую половину получила Розалин С. Яллоу «за разработку радиоиммунного анализа пептидных гормонов». Даны описания основных научных достижений Р. Гиймена в создании нейроэндокринологии. Он выделил соматотропин (гормон роста), идентифицировал молекулы тиреотропин-высвобождающего гормонатиреолиберина, который контролирует все функции щитовидной железы, а также десятки других молекул из гипоталамуса. Его исследования привели к разработке методов лечения самых разных заболеваний – от бесплодия до опухолей гипофиза. Своими открытиями некоторых информационных потоков в мозге человека он способствовал расшифровке кода человеческой жизни. Большое значение в этом имела

юношеская подготовка Гиймена в области конструирования радиоприемников и передатчиков, а его серьезный опыт в работе с компьютерами привел к тому, что он стал одним из пионеров в цифровой живописи. Р. Гиймен лишь три года назад отошёл от активной научной жизни.
Ключевые слова: лауреат Нобелевской премии по физиологии или медицине Роже Гиймен; мозг человека; нейроэндокринология; информационные потоки.

Для цитирования: Tyutyunnik VM. Information flows in the human brain. Roger Guillemin is 100 years old. *Journal of Advanced Materials and Technologies*. 2024;9(1):008-011. DOI: 10.17277/jamt.2024.01.pp.008-011

In Nobel studies, there are several cases where Nobel laureates lived to see their centenary, with almost all of them occurring in the 21st century, and one of the reasons for the increase in creative longevity is the activities of the laureates themselves, including the 1977 Nobel Prize in Physiology or Medicine laureate Roger Guillemin (Fig. 1). He shared half the prize with Andrew W. Schally "for his discoveries concerning the production of peptide hormones in the brain", and the other half went to Rosalyn Yallow "for the development of a radioimmunoassay for peptide hormones". The results of their research have made a significant contribution to increasing human life expectancy.

Roger Guillemin [1, 2] was born on January 11, 1924 in the city of Dijon, the capital of Burgundy (France). Despite the occupation of Dijon by the Germans from 1940 to 1944, he managed to graduate from primary school and lyceum, receive a medical education and, in 1949, a doctorate in endocrinology. Having met Hans Selye, Guillemin received a scholarship from his foundation and moved to the Institute of Experimental Medicine and Surgery at the University of Montreal (Canada). It was there that he completed his doctoral research, and in 1953 he earned his PhD in physiology. Then he moved to the USA, until 1970 he taught at Baylor College of Medicine in Houston (Texas), moved to the Salk Institute for Biological Research in San Diego (California), where he founded the world's first laboratory of neuroendocrinology, developed his main discoveries and is still listed as an emeritus professor [3]. There he celebrated his 100th birthday (Fig. 2). R. Guillemin is the generally recognized founder of neuroendocrinology, a study of the interaction of the endocrine and nervous systems, i.e. regulation by the brain of the body's hormonal activity. His research into brain hormones led to the development of treatments for diseases ranging from infertility to pituitary tumors. In fierce competition with a native of Poland, E.V. Schally ("Many years of aggression and cruel revenge" [4, 5]), which is even called the "third neuroscientific war" [4], R. Guillemin managed to discover somatostinum, a regulator of the functioning of the pituitary gland and pancreas, isolate endorphins - brain molecules that act as opium alkaloids, identify cellular growth factors, discover the role of the brain in regulating hormones – molecules that act as chemical messengers between different parts of the body and regulate body functions.

These studies were incredibly painstaking and lengthy, without much hope of success. Suffice it to say that in four years (1964-1967) in Houston,

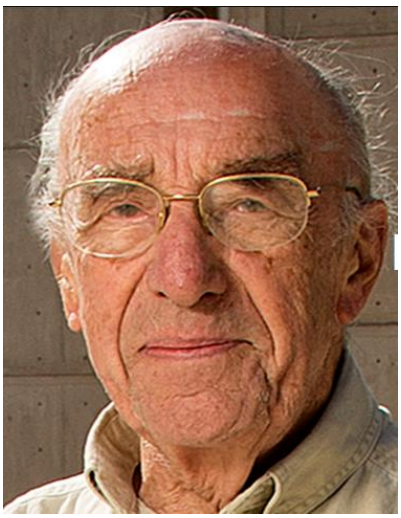

Fig 1. R. Guillemin at the age of 90 (© Courtesy of Salk Institute)

Fig. 2. R. Guillemin at the celebration of his 100th birthday (© Courtesy of Salk Institute)

more than 5 million pieces (50 tons) of sheep hypothalamus had to be collected, and the purification and determination of the chemical structure of the first neurohormone thyrotropin-releasing factor (TRF) took seven years and was successfully completed in 1969 Subsequently, R. Guillemin calculated that 1 kg of purified TRF cost 2.5 times more than the same weight of soil delivered from the Moon. This success led to the isolation of somatotropin (growth hormone), the identification of the thyrotropin-releasing hormone (TRH) molecule, thyrotropin-releasing hormone, which controls all functions of the thyroid gland. The use of the radioimmunoassay method developed by R. Yalow played a huge role in further work. Later, R. Guillemin and E. Schally (both received American citizenship in the 1960s) and their colleagues isolated other molecules from the hypothalamus (now many dozens of them are known) that control all functions of the pituitary gland, for example, gonadotropin-releasing hormone (GnRH) – A hormone from the hypothalamus that causes the pituitary gland to release gonadotropins, causing the release of hormones from the testes or ovaries. This discovery led to advances in the treatment of infertility and prostate cancer. It became clear that the human brain is the most important gland of the body.

Fig. 3. Four Nobel Prize laureates in physiology or medicine (from left to right; years of award in brackets) at one conference: R. Dulbecco (1975), R. Guillemin (1977), R. Holley (1968) and F. Crick (1962) (© Courtesy of Salk Institute)

Thus, R. Guillemin joined a small circle of outstanding scientists, each of whom, with their discoveries of individual information flows in the human brain [6], contributed to deciphering the code of human life (Fig. 3).

R. Guillemin was an amazingly versatile personality. Even in childhood and adolescence, he persistently developed not only his brain, but also his hands, creating, for example, radio receivers and transmitters. In his mature years, he transferred his many years of experience with computers from neuroendocrinology to art and became one of the pioneers in digital painting; he is also known as an avid collector of French and American paintings and sculptures, Papuan and pre-Columbian ceramics. Several keyboards and stringed instruments form part of the pleasant furnishings of his happy home. Having retired from active scientific work, R. Guillemin spent the last three years in Del Mar (California) and devoted all his time to his family. He had five daughters, a son, four grandchildren and two great-grandchildren. His wife Lucienne, to whom he was married for 69 years, died in 2021 at the age of 100!

At the centennial celebration, the current president of the Salk Institute, Gerald Joyce, said: “Roget is one of the world's greatest minds and at the same time one of the kindest people you will ever meet” [3].

Unfortunately, when the article was already in print, the sad news came about the death of Roger Guillemin on February 21, 2024.

Funding

This study received no external funding.

Conflict of interests

The authors declare no conflict of interest.

References

1. Klavdiyeva MM. To the centenary of Nobel laureate Roger Guillemin. Guillemin and his influence on Soviet neuroendocrinologists. *Istoriko-biologicheskiye issledovaniya*. 2023;4:96-121. DOI:10.24412/2076-8176-2023-4-96-121 (In Russ.)

2. Karyakin OB. Roger Guillemin, Andrew Victor Schally, Rosalyn Sassman Yalow. *Cancer Urology*. 2021;4:176-180. DOI:10.17650/1726-9776-2021-17-4-176-180 (In Russ.)

3. Roger Guillemin. Available from: https:// www.salk.edu/ru/news-release/salk-distinguished-

professor-emeritus-roger-guillemin-nobel-prize-laureate-celebrates-100th-birthday/ [Accessed 11 January 2024].

4. Paevsky A. *Nobel laureates: Roger Guillemin.* The third neuroscientific war. Available from: https://indicator.ru/medicine/nobelevskie-laureaty-rozhe-giimen.htm [Accessed 11 January 2024] (In Russ.)

5. Sapolsky R. *Why zebras don't have heart attacks: The Psychology of Stress*. St. Petersburg: Piter; 2019. 700 p. (In Russ.)

6. Fedorov VA, Hargittai I, Tyutyunnik VM. The Global information and cosmological problem: 2020 Nobel Prize Winner in Physics Roger Penrose. *Journal of Advanced Materials and Technologies*. 2022;3:168-171. DOI:10.17277/jamt.2022.03.pp.168-171

Information about the authors / Информация об авторах

Viacheslav M. Tyutyunnik, D. Sc. (Eng.), Professor, Tambov State Technical University; Director General, International Nobel Information Centre, Tambov, Russian Federation; ORCID 0000-0002-2099-5730; e-mail: vmtyutyunnik@gmail.com

Тютюнник Вячеслав Михайлович, доктор технических наук, профессор, Тамбовский государственный технический университет; генеральный директор, Международный Информационный Нобелевский Центр, Тамбов, Российская Федерация; ORCID 0000-0002-2099-5730; e-mail: vmtyutyunnik@gmail.com

Received 14 February 2024; Accepted 4 March 2024; Published 26 April 2024

Original papers
Nanostructured, nanoscale materials and nanodevices

УДК 546.26-162; 66.094.3; 661.66 DOI: 10.17277/jamt.2024.01.pp.012-022

Metal oxide catalysts for low-temperature template CCVD synthesis of carbon nanotubes

© Anatoliy P. Prudchenko[a]✉, Oksana Yu. Polyakova[a], Julia S. Protasevich[a]

[a] *L. M. Litvinenko Institute of Physical Organic and Coal Chemistry, 70, Rosa Luxemburg St., Donetsk, Donetsk People's Republic, 283048, Russian Federation*

✉ prudchenko.a@yandex.ru

Abstract: Using the method of polymerized complex precursors (PCP) and a wide range of chelating agents, we synthesized metal oxide catalysts (MOCs) with a general composition of Me_2Co / $CaCO_3$ (CaO, MgO, NaCl, Me – Fe, Ni) and a molar ratio of Me_2Co / carrier from 0.06 : 1 to 0.55 : 1; the effectiveness of such MOCs in the synthesis of carbon nanotubes by catalytic chemical vapor deposition was determined from the gas phase (CCVD synthesis). The dependence of the specific yield and morphology of the carbon product on the MOCs composition and the nature of the chelating agent, being a decisive factor in the process of preorganization of the catalyst structure, has been established. The use of catalysts for the growth of CNTs with the composition of Ni_2Co / $CaCO_3$ (CaO) allows the CCVD process to be carried out at low temperatures (450–500 °C) in contrast to 800 °C for MOCs with the composition of Fe_2Co / $CaCO_3$ (CaO) and leads to the formation of structurally homogeneous arrays of multi-walled carbon nanotubes. At the same time, the specific yield of CNTs decreases with an increase in the temperature of the process, but an increase in the mole fraction of active metals in the catalyst leads to an increase in the specific yield of CNTs. Yet, the dependence has the form of a curve with a tendency to reach a plateau, which indicates an increase in the processes of agglomeration of metal nanoparticles, increasing their size and, due to this, reducing the possibility of nucleation of carbon nanotubes. It has been suggested that low-temperature CCVD synthesis using MOC composition Ni_2Co / $CaCO_3$ (CaO, MgO, NaCl) is realized due to the unique magnetic and electronic properties of the Ni – NiO system, which makes it possible to initiate the process of nucleation and then growth of nuclei of catalytic nickel particles at temperatures exceeding the Curie point Ni (> 360 °C).

Keywords: carbon nanotubes; CCVD synthesis; metal oxide catalysts; chelating agent.

For citation: Prudchenko AP, Polyakova OYu, Protasevich JuS. Metal oxide catalysts for low-temperature template CCVD synthesis of carbon nanotubes. *Journal of Advanced Materials and Technologies*. 2024;9(1):012-022. DOI: 10.17277/jamt.2024.01.pp.012-022

Металлоксидные катализаторы для низкотемпературного темплатного CCVD синтеза углеродных нанотрубок

© А. П. Прудченко[a]✉, О. Ю. Полякова[a], Ю. С. Протасевич[a]

[a] *Институт физико-органической химии и углехимии им. Л. М. Литвиненко, ул. Розы Люксембург, 70, Донецк, Донецкая народная республика, 283048, Российская Федерация*

✉ prudchenko.a@yandex.ru

Аннотация: Методом полимеризованных комплексных предшественников (ПКП) с использованием широкого ряда хелатных агентов синтезированы металлоксидные катализаторы (МОК) общего состава Me_2Co / $CaCO_3$ (CaO, MgO, NaCl, Me – Fe, Ni) с мольным соотношением Me_2Co / носитель от 0,06 : 1 до 0,55 : 1, определена эффективность действия таких МОК в синтезе углеродных нанотрубок методом каталитического химического осаждения углерода из газовой фазы (CCVD – Catalytic Chemical Vapor Deposition). Установлена зависимость удельного выхода и морфологии углеродного продукта от состава МОК и природы хелатного агента как решающего фактора в процессе предорганизации структуры катализатора. Применение катализаторов роста углеродных нанотрубок (УНТ) состава Ni_2Co / $CaCO_3$ (CaO) позволяет проводить CCVD процесс при низких

температурах (450…500 °C) в отличие от 800 °C для МОК состава Fe_2Co / $CaCO_3$ (CaO) и приводит к образованию однородных по структуре массивов многостенных углеродных нанотрубок. При этом удельный выход УНТ уменьшается с ростом температуры процесса, а увеличение мольной доли активных металлов в катализаторе хотя и приводит к росту удельного выхода УНТ, но зависимость имеет вид кривой с тенденцией к выходу на плато, что свидетельствует об усилении процессов агломерации наночастиц металлов, увеличении их размеров и снижении за счет этого возможности нуклеации углеродных нанотрубок. Сделано предположение, что низкотемпературный CCVD синтез с использованием МОК состава Ni_2Co / $CaCO_3$ (CaO, MgO, NaCl) реализуется благодаря уникальным магнитным и электронным свойствам системы Ni – NiO, позволяющим инициировать процесс зародышеобразования, а затем и роста зародышей каталитических частиц никеля при температурах, превышающих точку Кюри Ni (> 360 °C).

Ключевые слова: углеродные нанотрубки; CCVD синтез; металлоксидные катализаторы; хелатные агенты.

Для цитирования: Prudchenko AP, Polyakova OYu, Protasevich JuS. Metal oxide catalysts for low-temperature template CCVD synthesis of carbon nanotubes. *Journal of Advanced Materials and Technologies*. 2024;9(1):012-022. DOI: 10.17277/jamt.2024.01.pp.012-022

1. Introduction

Iijima's discovery of carbon nanotubes (CNTs) in 1991, followed by the isolation and study of graphene (by A. Geim and I. Novoselov in 2004), the establishment of their extraordinary properties and the resulting possible practical applications stimulated a huge amount of research into determining the patterns of processes of producing carbon nanomaterials (CNMs) with specified properties [1–3]. At the same time, the researchers' attention was focused on finding optimal conditions for the synthesis of such CNMs as graphene, nanocarbon (NC), and CNTs.

The most common and commercially attractive method for producing CNTs is CCVD (*Catalytic Chemical Vapor Deposition*) – a process that is characterized by simplicity of instrumentation, low process temperatures (600–1100 °C); it does not require creating reduced or increased pressure, and can be scaled up to industrial installations [3]. However, in our opinion, the simplicity and advantages are apparent compared to other methods of CNTs synthesis – laser ablation and synthesis in an arc discharge. The problem is that the result of CCVD synthesis depends on many parameters – elemental composition, dispersion and texture of metal oxide catalysts (MOCs), the nature of the catalyst support, carbon precursor, carrier gas, gas flow rate and their ratio, process temperature and even design features reactor. As a result, a huge number of researchers are working to find general patterns of the mechanism of formation of CNTs.

Our major interest is the problem of the MOCs synthesis, which makes it possible to produce CNTs with a high degree of selectivity in low-temperature CCVD synthesis, which is quite an urgent problem [1, 4–6]. The disadvantage of most catalysts for this process (mainly based on Fe, Co) is the fact that they begin to work in the high temperature zone (800–1000 °C), where the formation of a non-catalytic flow product is most likely [7, 8]. Therefore, reducing the temperature of CCVD synthesis of CNTs is an important technological task and enables to bring the conditions for CNTs growth closer to the conditions of processes occurring in planar technology [9]. One solution to this issue is the introduction of Ni or (Ni – Co) into the MOCs composition, which reduces their surface tension, as well as the use of oxides with low surface energy as a substrate [10]. Thus, MOCs of the composition Ni / SiO_2 make it possible to reduce the synthesis temperature to 625 °C [10], those of Ni / MgO reduce it to 600–650 °C [11–13] and even to 550 °C, using camphor as a carbon precursor [14]. In [9], Ti and Ni films deposited by electron beam sputtering onto a substrate of oxidized single-crystalline silicon made it possible to achieve CNTs growth in a flow of argon, acetylene and ammonia at 500 °C. In a more complex process with atomic deposition of Ni on a ZrO_2 substrate and plasma enhanced chemical vapor deposition (PECVD) synthesis of CNTs, the temperature can be reduced to 340 °C [15], but issues arise with scalability. Taking into account the rather modest information on this issue, an important task, in our opinion, remains the further development of such catalytic systems that would operate under mild conditions and allow the CNTs production with the required quality parameters.

We developed a method using polymerized complex precursors (PCP) to synthesize MOCs of the general composition Me_2Co / $CaCO_3$ (CaO, MgO, NaCl, Me – Fe, Ni) and studied their effectiveness in the CCVD synthesis of CNTs. The PCP method for the MOCs synthesis was chosen because it allowed

one to obtain highly dispersed and highly porous MOCs powders with low bulk density and high catalytic activity. In essence, the MOCs synthesis technique we use is a superposition of the two most commonly used methods – the sol-gel method and the thermal decomposition method. The difference is that the PCP method makes it possible to implement the stage of preorganization of the spatial structure of the catalyst due to the intermediate stage of the formation of a highly porous polymer-organic matrix of the precatalyst, isolated in solid form.

2. Materials and Methods

2.1. Reagents

Metaloxide catalysts (MOCs–PCP) of the general composition Me_2Co / $CaCO_3$ (CaO, MgO, NaCl, Me – Fe, Ni) with a molar ratio Me, Co / carrier equal to 0.12 : 1 were prepared by the PCP method using nitrates of crystalline metal hydrates Fe^{3+}, Co^{2+}, Ni^{2+}, Ca^{2+}, Mg^{2+}, sodium chloride; chelating agents – sucrose, fructose, glucose, ethylene glycol (EG), pure; diethylene glycol (DEG), pure; glycerol (GLY), pure; 1,2 – propylene glycol (PG), pure; 1,4 – butylene glycol (BG), pure; polyethylene glycol (PEG); polyvinyl alcohol (PVA), pure; pentaerythritol (PET), pure; food gradecitric acid (CA); glycine (GLYC), pure; and distilled water. MOCs-PCP obtained using two chelating agents, one of which is citric acid, are designated EG + CA, DEG + CA, GLY + CA, PG + CA, BG + CA, PVS + CA, PET + CA, GLYC + CA.

2.2 A method for the synthesis of supported MOCs for the CNTs growth using the PCP method

The essence of the PCP method is to use the ability of 3d-group metal cations to form stable complexes with carbohydrates (mono-, di- and polysaccharides, polyalcohols, oxy- and amino acids, etc.) of the composition $Me(NO_3)_xL$, where L is organic ligand [16]. Thermolys is of such a complex above 130 °C leads, as a result of the polyesterification reaction, to the formation of a three-dimensional polymer organic matrix in which the metal ions that make up the catalyst are evenly distributed throughout its entire volume. Subsequent controlled burning of the organic part leads to the formation of a nanodispersed system of mixed oxide structures, which are precursors for catalysts for the growth of multi-walled carbon nanotubes (MWCNTs).

The synthesis of metal oxide catalysts was carried out in several successive stages, presented in Table 1.

Thus, the method we developed earlier [17] is as follows: solutions of nitrates of active metals and carriers in the required stoichiometric ratios using the minimum possible amount of water were mixed with a carbohydrate solution (sucrose, glucose, fructose) at a molar ratio of carbohydrate : Me from 5 : 1 to 10 : 1. After dissolving and mixing all components, the mixture was heated to 70–80 °C with stirring until a violent reaction began with the release of brown NO_2 vapors, as a result of which the color of the reaction mass changed from light brown to dark

Table 1. Stages of MOC synthesis using the PCP method

Stage	Temperature, °C	Time, min	Process
1. Dissolution of components, homogenization	70–80	15	Formation of the carbohydrate – Me^{n+}, redox reaction
2. Production of viscous syrups	100–115	10	Dehydration
3. Formation of a solid precatalyst matrix	130–200	180	Thermal oxidation under gentle conditions
4. Precatalyst decomposition	250–450	20	Thermal oxidation of the carbon matrix
5. Annealing	550–650	180	Removal of residual organic carbon matrix
6. Mechanical activation	25	5	Increasing the reactivity of MOCs

green or blue (cobalt). After gas evolution ended, the mixture was kept at 105–115 °C to remove excess water and prepare viscous syrup. Next, a small portion of the syrup was placed in a porcelain cup with a capacity of 350 cm^3 and kept for three hours in a muffle furnace at 200 °C. During this time, the mixture increased significantly in volume (50–100 times) and hardened into fine-celled foam. The foam thus obtained was placed in a muffle furnace and controlled annealed at T = 300–650 °C for 3 hours. As a rule, when the furnace temperature reached 260–270 °C, spontaneous combustion of the foam occurred; combustion spread from the outer surface to the center of the mixture and led to a decrease in the volume of the sample. Next, the product was annealed at 500–650 °C for three hours. MOC, as a product of this process, was a light, highly porous coral-like mass with a well-developed surface, the frame of which consists of highly dispersed $CaCO_3$ particles (CaO, MgO, NaCl) and oxides of active metals.

2.3. CCVD synthesis

The CCVD synthesis of CNMs was carried out in a tubular quartz reactor at 500–800 °C and flow rates of carrier gas (Ar) and carbon precursor gas (propane – butane mixture in compliance with Russian Standard 27578-87) 60 and 30 $cm^3 \cdot min^{-1}$, respectively. The process time is 60 min. The laboratory installation diagram is shown in Fig. 1.

Specific yield of carbon product (η_C, $g \cdot g_{cat}^{-1}$), as a relative quantity characterizing the efficiency of the process, was calculated as the ratio of the weight of the resulting carbon product to the weight of the template (catalyst) according to equation (1):

$$\eta_C = \frac{m_C}{m_T}, \qquad (1)$$

where m_C is weight of carbon product, g; m_T is template mass (for CNTs synthesis m_T is the template weight with a deposited metal oxide catalyst, determined taking into account the mass loss in the "zero" experiment, g.

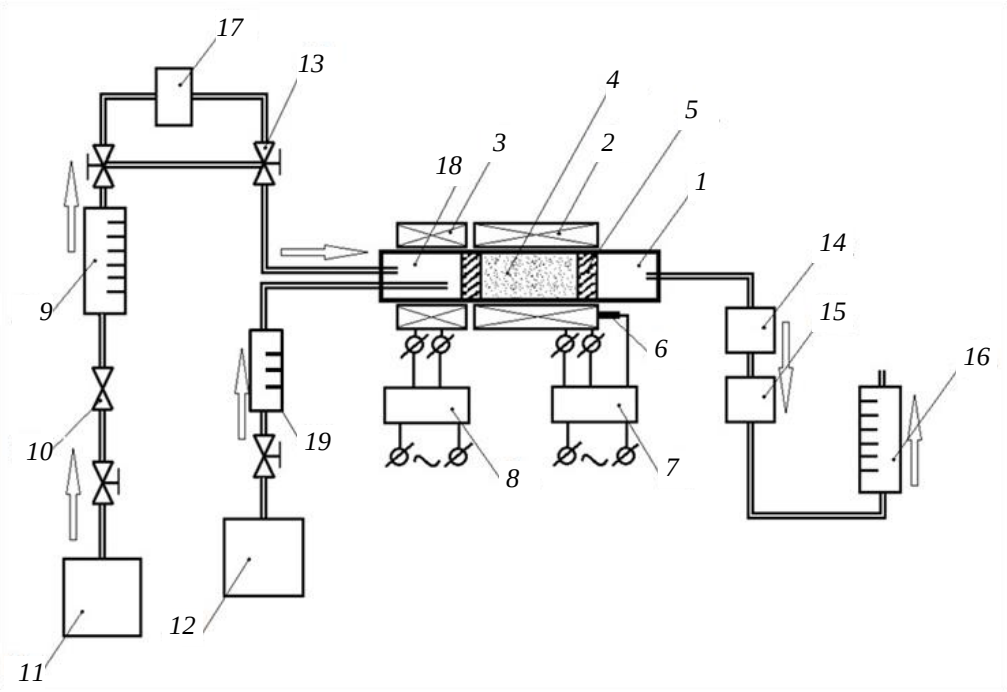

Fig. 1. Diagram of a laboratory installation for CNTs CCVD synthesis:
1 – tubular quartz reactor; *2* – pyrolysis zone heating furnace; *3* – preheating furnace; *4* – template; *5* – porous carbon inserts; *6* – thermocouple; *7* – measuring and regulating device; *8* – preheating furnace voltage regulator; *9* – rotameter; *10* – needle valve; *11* – carrier gas cylinder; *12* – carbon precursor gas cylinder; *13* – manual adjustment valve; *14*, *15* – absorbers; *16* – bubble gas flow meter; *17* – liquid supply system; *18* – steam–gas mixture input and mixing unit; *19* – rotameter for supplying carbon precursor gas

2.4. Isolation of CNMs

CNMs were isolated by treating the carbon-mineral product with 30 % HCl or 30 % HNO_3 or a mixture of them in a ratio of 3 : 1 (by volume). The mixture was heated and kept at boiling for 2 hours, then cooled to room temperature, left for 24 hours, then filtered on a glass filter, washed with deionized water to pH ≈ 7, with acetone, and dried at 105 °C to constant weight.

2.5. Analytical methods

The structural features of CNMs were studied by X-ray diffraction (XRD) using a DRON-3 diffractometer using CuK_α radiation, with a wavelength λ_α = 1,54181 Å (*U* = 30 kV, *I* = 20 мА).

Studies of the morphology of carbon nanotubes and template nanomaterials were carried out using transmission and scanning electron microscopy using a JEM-200A microscope from JEOL (Japan) and a JSM-6490LV scanning electron microscope (Japan) with an energy-dispersive INCA Penta FETx3 attachment (OXFORD Instruments, UK).

3. Results and Discussion

The method we have developed for the synthesis of metal oxide catalysts for the CNTs growth by the PCP method involves the stage of preorganization of the catalyst structure by creating a solid 3d pre-catalyst matrix (a system of mixed oxide phases) with a developed system of meso- and macropores. Therefore, not only the precursors of carrier oxides and active metals, but also the chelating agents used can play an important role in this process.

To compare the efficiency of catalysts obtained using various chelating agents, catalysts of the composition Me_2Co / $CaCO_3$ (CaO, Me – Fe, Ni) with the same molar ratio of Me_2Co / $CaCO_3$ equal to 0.12 : 1 were synthesized (section 2.1). CCVD synthesis of CNMs was carried out according to the method described above in section 2.2 in a tubular quartz reactor at 500 and 800 °C and flow rates of carrier gas (Ar) and carbon precursor gas (propane – butane mixture) of 60 and 30 $cm^3 \cdot min^{-1}$, respectively. The process took 60 min.

Data on the specific yield of CNMs in the CCVD process and the bulk density of the corresponding MOCs are presented in Table 2.

According to the data presented in Table 2, catalysts obtained by the PCP method, compared with catalysts obtained by other methods, are characterized by low bulk density values (ρ = 0.01–0.25 $g \cdot cm^{-3}$) [18].

Table 2. Specific yield of CNMs

Chelates names	Specific yield of CNMs η_C, $g \cdot g_{cat}^{-1}$	Bulk density of CNTs catalyst ρ, $g \cdot cm^{-3}$
Sol	0.118	0.985
Sucrose	2.82	0.032
Fructose	2.75	0.069
Glucose	3.17	0.085
EG	0.13	0.217
EG + CA	1.07	0.104
DEG	0.25	1.109
DEG + CA	1.89	0.049
GLYC	0.11	0.146
GLYC + CA	0.88	0.133
PG	0.63	0.216
PG + CA	1.35	0.104
BG	1.31	0.164
BG + CA	1.76	0.163
PEG	1.36	0.184
PEG + CA	3.31	0.061
PET	1.15	0.558
PET + CA	4.28	0.051
PVA	0.56	0.182
PVA + CA	1.29	0.340
GLYC + CA	1.35	0.157
Sucrose*	5.13	0.023
Fructose*	5.59	0.056
EG + CA*	3.16	0.048
GLYC + CA*	2.48	0.065
BG + CA*	1.65	0.163
PEG + CA*	2.90	0.061
PVA*	4.18	0.182

N o t e : Items marked in the table with * refer to catalysts of general composition Ni_2Co / $CaCO_3$.

Bulk density is the most important parameter of catalysts for heterophase processes, since it clearly affects the progress of the process (gas diffusion rate, heat transfer, resistance to gas flows), especially in vertical versions of reactor equipment.

Table 2 and the dependence presented in Fig. 2 clearly indicate the dependence of the specific yield of CNMs on the nature of the ligand used in the process of pre-organization of the catalyst for the growth of CNTs.This means that, firstly, in terms of their efficiency, such MOCs are an order of magnitude higher than MOCs synthesized using traditional sol-gel technology; secondly, the productivity of MOCs obtained using two ligands (the second is citric acid) is significantly higher than that for monoligand samples; thirdly, the specific yield of CNMs obtained in the CCVD process using Ni_2Co / $CaCO_3$ catalysts is either the same or significantly higher compared to iron-cobalt MOCs, but such indicators are achieved at much lower synthesis temperature parameters (500 *vs*. 800 °C).

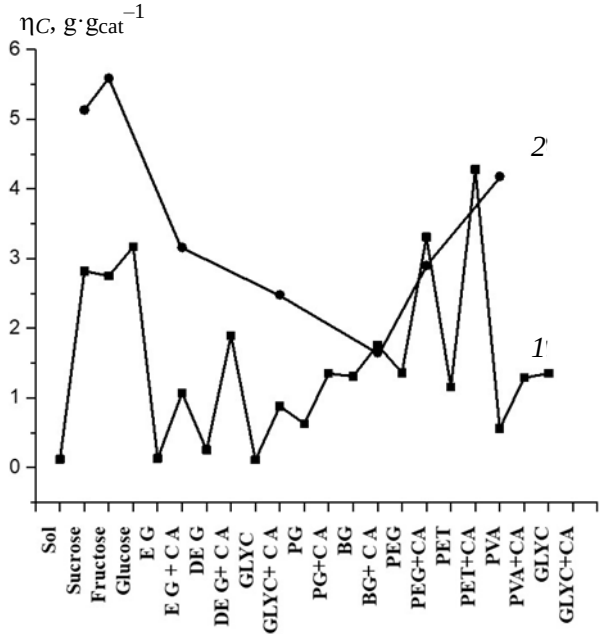

Fig. 2. The dependence of the efficiency of the MOCs – PCP of the total composition of Me_2Co / $CaCO_3$ (CaO) (Me – Fe, 800 °C, curve *1*, Me – Ni, 500 °C, curve *2*) in the CCVD synthesis of CNTs on the nature of chelating agents

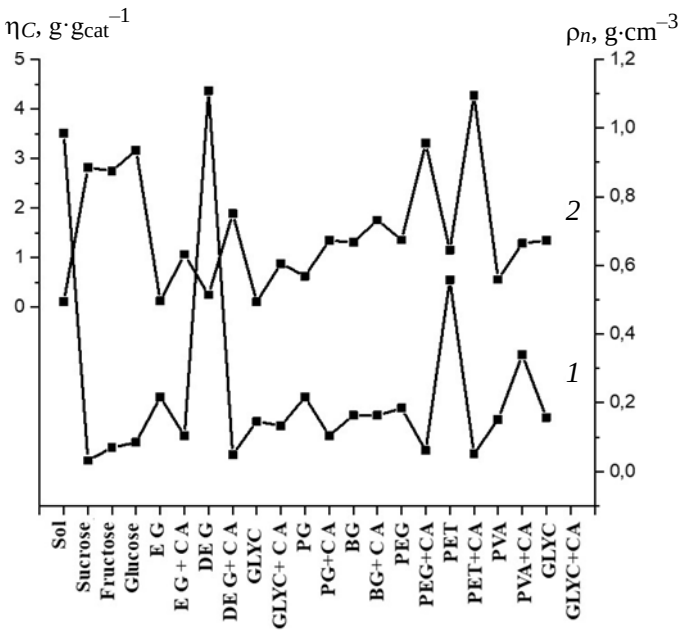

Fig. 3. Dependence diagrams of bulk density (*1*) and specific yield of CNMs (*2*) on the nature of the ligand

This type of dependence with minima for monoligand and extrema for bigand compositions correlates well with the dependence of such a significant indicator for heterogeneous catalysts as bulk density on the nature of the ligand, as shown in Fig. 3.

From a comparative analysis of the data presented in Fig. 3, it follows that MOCs with lower ρ are more effective compared to MOCs with higher ρ (the minima on curve *1* coincide with the maxima on curve *2* and vice versa). It has been established that the use of a second chelating ligand (citric acid) in almost all cases leads to the production of MOCs with low ρ. This fact is explained by the fact that when using citric acid, the degree of homogenization of metal ions in the MOCs matrix increases due to an additional complexing agent, as well as an increase in the depth of the polyesterification process and the formation of a cross-linked spatial network of the pre-catalyst. Ultimately, this leads to the formation of homo- or heterogeneous clusters of active metal particles of small sizes and homogeneous composition in the reducing atmosphere of the reactor [19]. The latter circumstance is a decisive factor in the process of initiation and growth of carbon nanotubes, since it determines both the morphological parameters of CNTs and the possibility of their formation.

When studying the morphology of carbon products of CCVD synthesis of CNMs on catalysts obtained using various ligands, in most cases their morphological similarity was found, as shown in Fig. 4*a*–*c*, and the product is coils of MWCNTs with a diameter of 15–50 nm with a structure like "matryoshka". The differences lie in the relative content of MWCNTs of different diameters, since when moving from saccharides to polyalcohols, the proportion of particles with a diameter greater than 40–50 nm increases. In addition, the magnetic susceptibility of MWCNT samples increases due to the encapsulation of metal particles in the internal space of the nanotubes, as well as at the growth end of the nanotube as a result of the formation of a carbon cap around the active metal particle. This phenomenon is especially characteristic of CNM samples obtained on MOC–PVA + CA (Fig. 4*d*, *e*, arrows indicate the places of encapsulation of metal particles) and MOC–PET + CA (Fig. 4*f*), although in the latter case the main a number of CNTs have open ends. Encapsulated metal particles are inaccessible to acids and cannot be removed during the isolation of MWCNTs, which is confirmed by the presence of intense reflections in the XRD-patterns at $2\theta = 44.56°$ and 64.92°, characteristic of α-iron [20]. The diffraction pattern of MWCNTs is shown in Fig. 5.

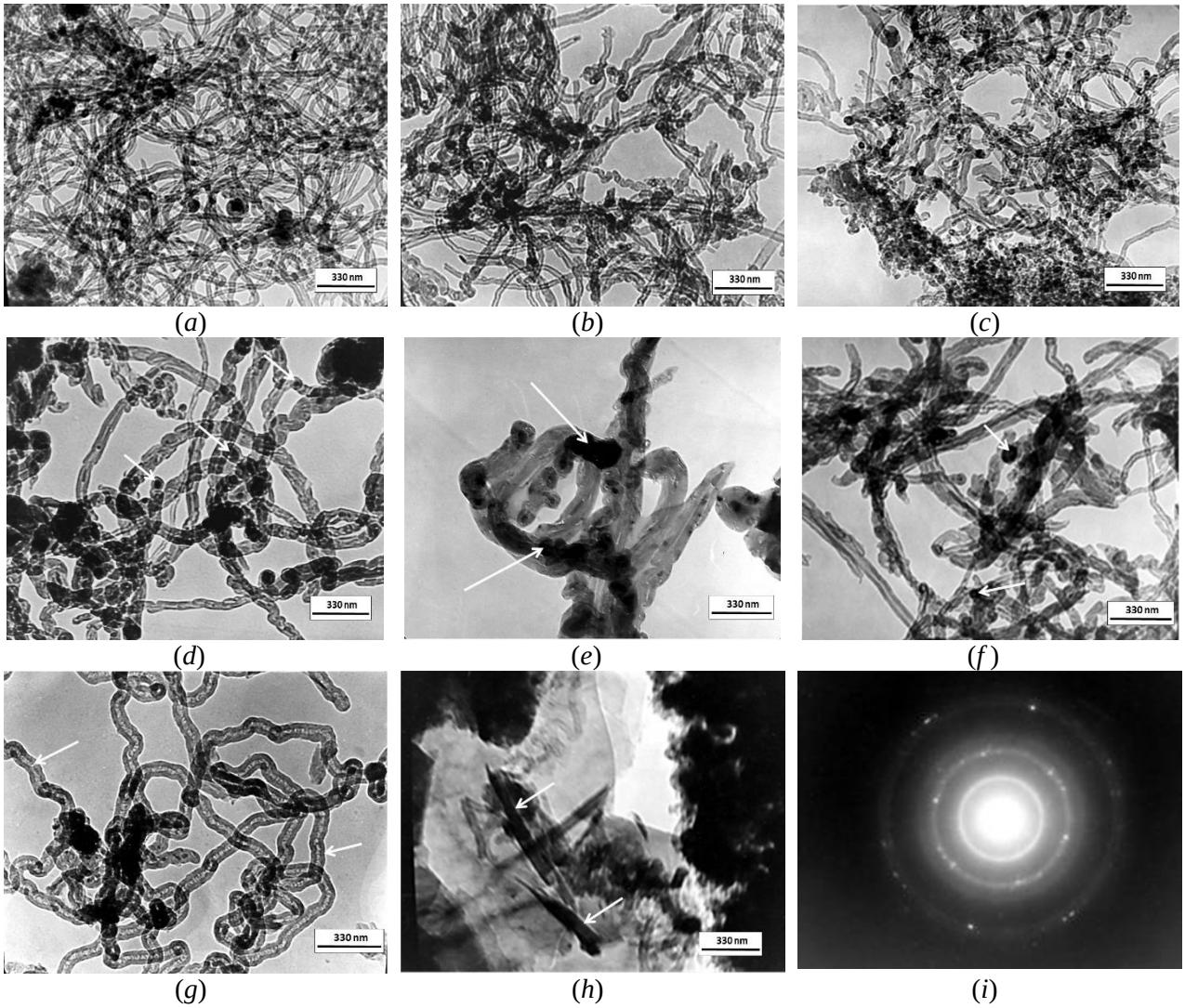

Fig. 4. TEM-images of the products of CCVD synthesis of CNMs on the MOC – PCP obtained using ligand compounds: *a* – sucrose; *b* – diethylene glycol; *c* – polyethylene glycol; *d*, *e* – polyvinyl alcohol; *f* – pentaerythritol; *g*, *h* – diethylene glycol at T = 850 °C; *i* – electronogram of CNM, obtained on MOC – DEG + CA at 850 °C (*a* – *h* – magnification 30.000×)

It should be noted that these samples are also characterized by the presence of particles with other morphological features – spiral and bamboo-shaped, which indicates an increase in the defectiveness of the graphene network of CNTs due to the appearance of fragments in the form of penta- and heptagons. The use of general Ni_2Co / $CaCO_3$ catalysts obtained using fructose as a chelating agent leads to the formation of thick-walled CNTs of uniform composition with an internal channel of very small diameter (~ 5–6 nm). It was also established that when the temperature of the CCVD process increases to 850 °C, nanotubes with internal constrictions appear in the carbon products of the CNTs synthesis on MOC–DEG + CA (Fig. 4*g*), nanotubes with internal constrictions appear (Fig. 4*g*), as well as carbon nanoparticles formed by a mechanism different from the formation of CNTs and having a "papier-mâché" or nanoscroll type structure (Fig. 4*h*). The appearance of such structures becomes clear from the discovery of flat 2D-structures of few-layer imperfect nanographene in carbon products, which is confirmed by the presence in the electron diffraction pattern of the corresponding sample of reflections related to the structure of graphite (Fig. 4*i*). The latter is probably associated with an increase in the contribution of the non-catalytic flow, which, for the process of carbon deposition on calcium carbonate, increases exponentially in a given temperature range [8].

Based on the data obtained, the best indicators for the quality and specific yield of CNTs in the CCVD process at T = 500 °C were obtained on MOC

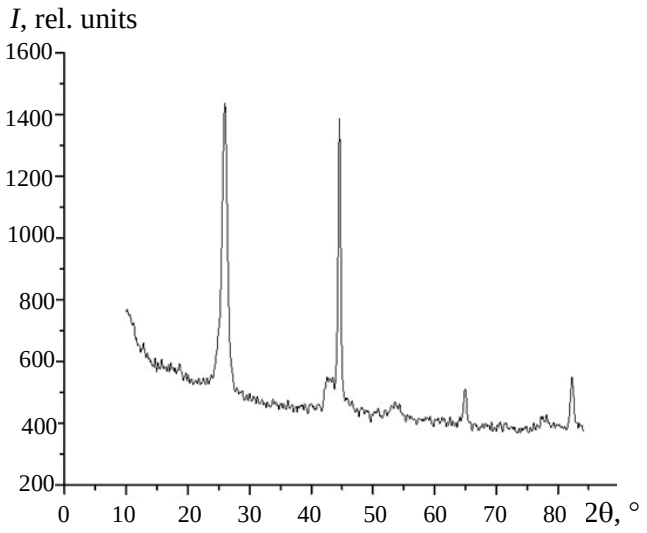

Fig. 5. Diffractogram of multi-walled carbon nanotubes obtained at the MOC–PVS

of the Ni_2Co / $CaCO_3$ composition using sucrose and fructose as a chelating agent, therefore we used the PCP (chelate - sucrose) method metal oxide catalysts (MOCs – PCP) of the general composition Ni_2Co / $CaCO_3$ (CaO, MgO, NaCl) with a molar ratio of Ni_2Co / $CaCO_3$ from 0.06 : 1 to 0.55 : 1 were obtained. To study the dependence of the specific yield of CNTs on the temperature of CCVD synthesis, MOCs with a molar ratio of Ni_2Co / $CaCO_3$ 0.12 : 1 were used.

The carbon products obtained after the CCVD process and removal of the template are CNTs coils with a diameter of 20–40 nm with a low content of amorphous carbon (AC) (Fig. 6*a*).

From the obtaineddata, it follows that when using this combination of active metals in the composition of MOCs and using $CaCO_3$ as a carrier, the process of CNTs synthesis begins already at T = 450 °C and occurs most efficiently at T = 500 °C. An increase in the process temperature leads to a decrease in the specific yield of CNTs (Fig. 6*b*), and this is also typical for MOCs, where sodium chloride was used as a carrier.

An increase in the mole fraction of active metals in the composition of MOCs while maintaining a fairly high specific yield leads to a decrease in process productivity, which is expressed in the tendency for the dependence η_C – Ni_2Co / $CaCO_3$ (NaCl), mol×mol^{-1} to reach a plateau (Fig. 7*a*, *b*).

Specific yield (η_C, g·g$_{cat}^{-1}$) of CNMs in CCVD synthesis using MOCs with the composition Ni_2Co / carrier (carrier: $CaCO_3$, MgO, NaCl) at the same molar ratios of components and synthesis conditions (Pr-But = 30 cm^3·min^{-1}, Ar = 60 cm^3·min^{-1}, t = 1 h, T = 500 °C) decreases in the next row: 5.13($CaCO_3$) > 0.62(MgO) > 0.15(NaCl). The introduction of at hird metal Fe in to the bimetal licmix ture Ni, Co leads to a decrease in the specific yield of CNTs at the molar ratio Fe : Ni : Co = 1 : 1 : 1 and 2 : 2 : 1 to 1.02 and 1.23, respectively. Monometallic catalysts with the composition Me / $CaCO_3$ (Me = Ni, Co, Fe) also have low productivity, which leads to a decrease in specific yield to 2.08 for Ni, 0.55 for Co and 0.62 for Fe.

Thus, from the data obtained, it follows that the most powerful factor influencing the performance of Ni–Co based MOCs, as well as for the Fe–Co system [21], is the nature of the catalyst carrier. The productivity of the CCVD process decreases when moving from a more basic oxide to a less basic

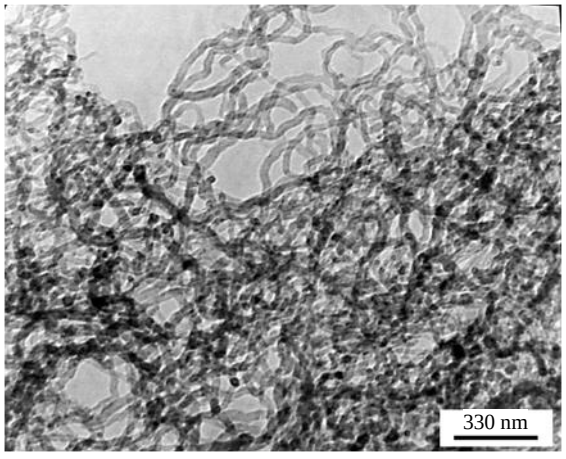

(*a*)

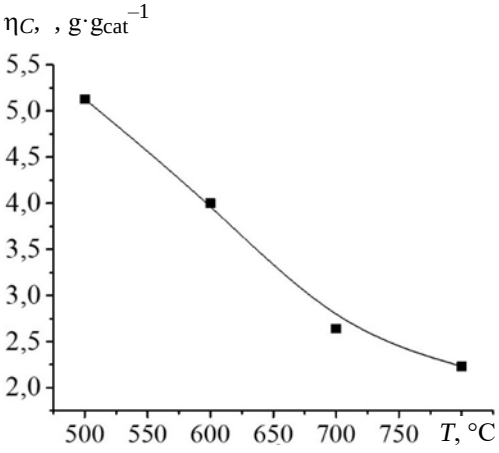

(*b*)

Fig. 6. TEM-image of CNTs obtained in low-temperature CCVD synthesis:
a – Ni_2Co / $CaCO_3$ (0.12 : 1 mol × mol^{-1}, Pr-But = 30 cm^3·min^{-1}, Ar = 60 cm^3·min^{-1}, T = 500 C, t = 1 h, chelate sucrose);
b – dependence of the specific yield of CNTs on the temperature of CCVD synthesis (Ni_2Co / $CaCO_3$ (CaO), Pr-But = 30 cm^3·min^{-1}, Ar = 60 cm^3·min^{-1}, t = 1 h, chelate sucrose)

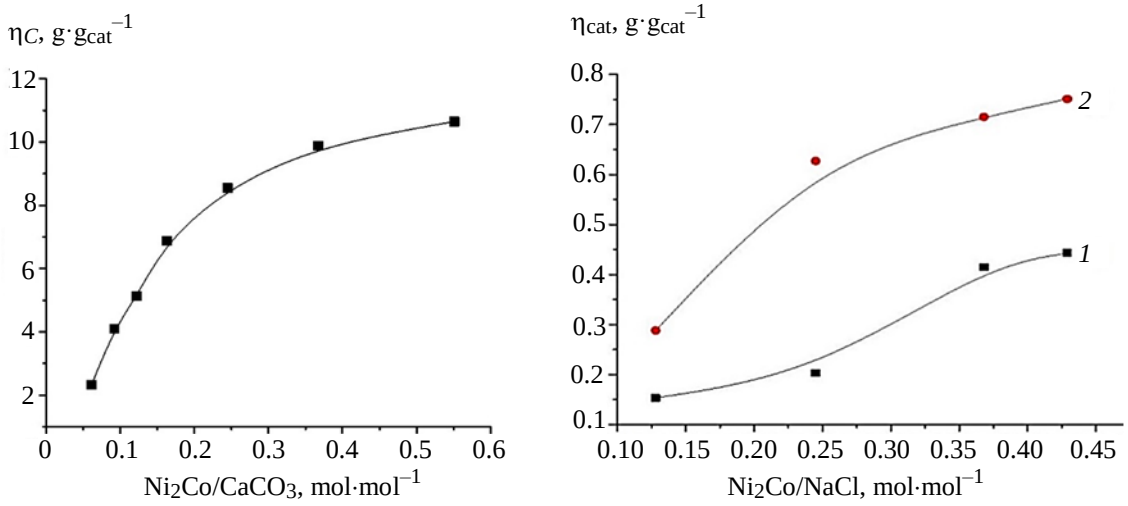

Fig. 7. Dependence of the specific yield of CNTs in the CCVD synthesis on the molar fraction of active metals: *a* – Ni_2Co / $CaCO_3$; Pr-But = 30 $cm^3 \cdot min^{-1}$, Ar = 60 $cm^3 \cdot min^{-1}$, t = 1 h, T = 500 °C; *b* – Ni_2Co / NaCl, $mol \cdot mol^{-1}$, Pr-But = 30 $cm^3 \cdot min^{-1}$, Ar = 60 $cm^3 \cdot min^{-1}$, t = 1 h, T = 650 °C – curve *1*; 750 °C – curve *2*

oxide or ionic carrier. This fact confirms our assumption that the catalyst support is directly involved in the process of electron transfer from the catalyst to hydrocarbons and back at the phase interface.

Due to the fact that the solubility of carbon in metals, as a decisive factor in the process of nucleation and formation of CNTs, decreases in the series Fe > Co > Ni [9], the type of temperature dependence becomes quite understandable – a rapid increase in the amount of pyrolytic carbon with limited solubility and the rate of carbon diffusion in the volume of the catalytic particle leads to the deposition of carbon on the outer surface of metal particles, their carbonization and, as a consequence, a decrease in process productivity. This process becomes more pronounced the higher the temperature of the CCVD process.

In contrast to Fe, Co MOCs, where the dependence η_C – Fe, Co / $CaCO_3$ (CaO), $mol \cdot mol^{-1}$ showed an extremum with a subsequent decrease in MOC productivity as the mole fraction of active metals increased, Ni, Co MOCs tend to decrease in efficiency (Fig. 7*a*, *b*), but this occurs to a moderate extent and is predictable. However, in our opinion, in both cases a size effect is manifested – as the content of active metals increases, the processes of agglomeration of reduced particles intensify, their enlargement to sizes with a critical radius of curvature, after which the CNTs formation becomes impossible. On the other hand, the unique decrease in temperature of the CCVD process of CNTs synthesis may be associated with the characteristics of the Ni, Co catalyst. Firstly, these metals, according to their state diagrams, are unlimitedly soluble in each other and form substitutional solid solutions over a wide range of concentrations. Secondly, the Ni–NiO system is one of the few that can exist in both oxidized (oxides) and reduced (metal) forms [19]. Thirdly, in the Ni–NiO system there are phase transitions of the second order: in NiO at 250 °C (523 K) an antiferromagnet – paramagnetic transition occurs, in Ni at 360 °C (633 K – the Curie point of Ni) – ferromagnet – paramagnetic. At T > 360 °C, such systems are paramagnetic and contain nickel particles of a certain size (more than 1 nm). This state of the system promotes not only the formation of embryos, but also their growth. Moreover, if at $T < T_C$ (Curie temperature – T_C) the oxidation of hydrocarbon occurs due to the oxygen of the NiO crystal lattice, then at $T > T_C$ the properties of the active center of the catalyst are determined by the set of Ni atoms formed during the reduction of nickel oxide. In our opinion, Co also plays a significant role in the reduction process of Ni due to the similarity of the electronic structure of the atoms and also the possibility of reduction through the hydrogen spillover mechanism. The validity of this assumption is confirmed by the fact that, as stated above, monometallic catalysts based on Ni and Co have much lower productivity compared to bimetallic Ni–Co and the principle of additivity of contributions is not observed.

4. Conclusion

Thus, based on the data obtained, it has been established that the use of the PCP method using chelating agents of various natures in the MOC synthesis for the CCVD synthesis of CNTs makes it possible to implement the process of preorganization of the spatial structure of the catalyst due to the formation of an intermediate highly porous polymer-organic pre-catalyst matrix. The latter, as well as the uniform distribution of active metal ions in the MOC matrix, lead to a significant increase in the efficiency of catalysts compared to the sol–gel method. The high efficiency of MOCs of the composition Ni_2Co / $CaCO_3$ in the CCVD synthesis of CNTs has been established; it has been shown that, in contrast to Fe, Co – MOCs (synthesis start temperature 800 °C), for these catalysts the process begins already at 450–500 °C and leads to an increase in the specific yield of the target product by 2–3 times. The influence of the stage of preorganization of the MOC structure using chelates of different nature is manifested in the formation of carbon products that differ in morphology. It has been suggested that low-temperature CCVD synthesis using MOCs of the composition Ni_2Co / $CaCO_3$ (CaO, MgO, NaCl) is realized due to the unique magnetic and electronic properties of the Ni–NiO system, which makes it possible to initiate the process of nucleation and then growth of nuclei of catalytic nickel particles at temperatures exceeding the Curie point of Ni (> 360 °C).

5. Funding

The research was supported by the Ministry of Science and Higher Education of the Russian Federation, the budget theme “Carbon nanoparticles with a given morphology: synthesis, structure and physicochemical properties, FRES-2023-0006”.

6. Conflict of interests

The authors declare no conflict of interest.

References

1. Elisev AA, Lukashin AV. *Functional materials.* Moscow: Fizmatlit; 2010. 456 p. (In Russ.)

2. Gusev AI. *Nanomaterials, nanostructures, nanotechnologies.* Moscow: Fizmatlit; 2007. 416 p. (In Russ.)

3. Bulyarsky SV. *Carbon nanotubes: technology, properties control, application*. Ulyanovsk: Strezhen; 2011. 432 p. (In Russ.)

4. Allaedini Gh, Masrinda Tasirin Si, Aminayi P, Yaakob Za. Carbon nanotubes via different catalysts and the important factors that affect their production: A review on catalyst preferences. *International Journal of Nano Dimension.* 2016;7(3):186-200.

5. Shah KA, Tali BA. Synthesis of carbon nanotubes by catalytic chemical vapour deposition: A review on carbon sources, catalysts and substrates. *Materials Science in Semiconductor Processing.* 2016;41:67-82. DOI:10.1016/j.mssp.2015.08.013

6. Allaedini Gh, Tasirin SM, Aminayi P. Synthesis of CNTs via chemical vapor deposition of carbon dioxide as acarbon source in the presence of NiMgO. *Journal of Alloys and Compounds.* 2015;647:809-814. DOI:10.1016/j.jallcom.2015.06.012

7. Vanyorek L, Loche D, Katona H, Casula MF, et al. Optimization of the catalytic chemical vapor deposition synthesis of multiwall carbon nanotubes on $FeCo(Ni)/SiO_2$ aerogel catalysts by statistical design of experiments. *Journal of Physical Chemistry.* 2011;115(13):5894-5902. DOI:10.1021/jp111860x

8. Prudchenko AP, Padun OM, Khripunov SV, Alemasova NV, Protasavich YuS. Regularities of the process of template synthesis of porous carbon materials using the CVD method. *Vestnik Luganskogo natsional'nogo universiteta imeni Vladimira Dalya.* 2018;5(11):299-303.(In Russ.)

9. Bulyarsky SV, Kitsyuk EP, Lakalina AV, Pavlova AA, Ryazanov RM. Solubility of carbon in a nickel catalyst during the growth of carbon nanotubes. *Mikroelektronika = Russian Microelectronics*. 2020;49(1): 27-32. DOI:10.31857/S0544126920010056 (In Russ.)

10. Noda LK, Gonc NS, Valentini A, Probst LFD, Almeida RM. Effect of Ni loading and reaction temperature on the formation of carbon nanotubes from methane catalytic decomposition over Ni/SiO_2. *Journal of Materials Science.* 2007;42:914-922. DOI:10.1007/s10853-006-0009-8

11. Magrez A, Seo JW, Smajda R, Mionić M, Forró L. Catalytic CVD synthesis of carbon nanotubes: towards high yield and low temperature growth. *Materials.* 2010;3(11):4871-4891. DOI:10.3390/ma3114871

12. Besperstova GS, Neverova MA, Stepanov AM, Burakova EA, Tkachev AG. The influence of the catalyst composition on the characteristics of synthesized carbon nanotubes. *Fundamental'nyye issledovaniya.* 2018;12:9-14. (In Russ.)

13. Mishchenko SV, Tkachev AG. *Carbon nanomaterials. Production, properties, application.* Moscow: Mechanical Engineering; 2008. 320 p. (In Russ.)

14. Kumar M, Ando Y. Chemical vapor deposition of carbon nanotubes: A review on growth mechanism and mass production. *Journal of Nanoscience and Nanotechnology.* 2010;10(6):3739-3758. DOI:10.1166/jnn.2010.2939

15. Ying Xi, Zubair A, Zichao Ma, Changjian Zh, et al. Low temperature synthesis of high-density carbon nanotubes on insulating substrate. *Nanomaterials.* 2019;9(3):473. DOI:10.3390/nano9030473

16. Stefanescu M, Ștefănescu O, Stoia M, Lazau C. Thermal decomposition of some metal-organic precursors: Fe_2O_3 nanoparticles. *Journal of Thermal Analysis and*

Calorimetry. 2007;88(1):27-32. DOI:10.1007/s10973-006-8003-6

17. Prudchenko AP, Savoskin MV, Khripunov SV, Padun OM, et al. Template synthesis of carbon nanotubes in the CCVD process: the influence of the catalyst application method on the morphology of particles and the specific yield of CNTs. *Innovative prospects of Donbass: Proceedings of the 5th International Scientific and Practical Conference.* 2019;4:40-44. (In Russ.)

18. Prudchenko AP, Savoskin MV, Polyakova OYu, Burkhovetsky VV, et al. Regularities of the process of template synthesis of carbon nanotubes and nanocarbon by CVD method. The influence of marokinetic factors of the process, the structure of the catalyst and the carrier on the morphology of carbon products. *Vestnik Luganskogo natsional'nogo universiteta imeni Vladimira Dalya.* 2021;5(47):23-28. (In Russ.)

19. Goncharuk VV, Kamalov GL, Kovtun GA. *Catalysis. Mechanisms of homogeneous and heterogeneous catalysis, cluster approaches.* Kyiv: Naukova Dumka; 2002. 541 p. (In Russ.)

20. *Crystallographic and crystal chemical database of minerals and their structural analogues.* Available from: http://mincryst.iem.ac.ru/rus/ [Accessed 09 September 2023] (In Russ.)

21. Prudchenko AP, Polyakova OYu. Template synthesis of carbon nanotubes in the CCVD process: the influence of the nature of the catalyst carrier on the morphology of carbon products. *Graphene and related structures: synthesis, production and application: materials of the IV International Scientific and Practical Conference / under general ed. organizing committee. Tambov: Publishing house IP Chesnokova A.V.* 2021; 77-81. (In Russ.)

Information about the authors / Информация об авторах

Anatoliy P. Prudchenko, Cand. Sc. (Chem.), Senior Researcher, L.M. Litvinenko Institute of Physical Organic and Coal Chemistry, Donetsk, Donetsk People's Republic, Russian Federation; ORCID 0009-0002-5664-4932; e-mail: prudchenko.a@yandex.ru

Oksana Yu. Polyakova, Junior Research Fellow, L.M. Litvinenko Institute of Physical Organic and Coal Chemistry, Donetsk, Donetsk People's Republic, Russian Federation; ORCID 0009-0002-4189-4947; e-mail: oksi-polyakova@mail.ru

Julia S. Protasevich, Engineer, L.M. Litvinenko Institute of Physical Organic and Coal Chemistry, Donetsk, Donetsk People's Republic, Russian Federation; ORCID 0009-0001-8704-887X; e-mail: us.protasevich@mail.ru

Прудченко Анатолий Павлович, кандидат химических наук, старший научный сотрудник, Институт физико-органической химии и углехимии им. Л. М. Литвиненко, Донецк, Донецкая Народная Республика, Российская Федерация; ORCID 0009-0002-5664-4932; e-mail: prudchenko.a@yandex.ru

Полякова Оксана Юрьевна, младший научный сотрудник, Институт физико-органической химии и углехимии им. Л. М. Литвиненко, Донецк, Донецкая Народная Республика, Российская Федерация; ORCID 0009-0002-4189-4947; e-mail: oksi-polyakova@mail.ru

Протасевич Юлия Станиславовна, ведущий инженер, Институт физико-органической химии и углехимии им. Л. М. Литвиненко, Донецк, Донецкая Народная Республика, Российская Федерация; ORCID 0009-0001-8704-887X; e-mail: us.protasevich@mail.ru

Received 15 November 2023; Accepted 10 January 2024; Published 26 April 2024

Original papers
Nanostructured, nanoscale materials and nanodevices

УДК 537.533.2; 535.375.54 DOI: 10.17277/jamt.2024.01.pp.023-036

Structural and field emission characteristics of carbon-containing cathodes

© Evgeny P. Sheshin[a]✉, Nataliya D. Kundikova[bc], Viktor B. Kireev[a], Kirill N. Belov[c], Fung Dyk Many[a], Alexey S. Berdnikov[c], Danila N. Prosekov[c]

[a] *Moscow Institute of Physics and Technology (NRU), 9, Institutsky Lane, Dolgoprudny, 141701, Russian Federation;*
[b] *Institute of Electrophysics, Ural Branch of the Russian Academy of Sciences, 106, Amundsen St., Ekaterinburg, 620016, Russian Federation;*
[c] *South Ural State University (NRU), 76, Lenin Av., Chelyabinsk, 454080, Russian Federation*

✉ sheshin.ep@mipt.ru

Abstract: Field emission and structural characteristics of carbon nanotube fibers, polyacrylonitrile fibers, pyrolytic graphite and micrograined dense graphite were experimentally studied before and after their operation as a field emission cathode using registration of the current-voltage characteristics, optical microscopy, scanning electron microscopy and Raman spectroscopy in the spectral range from 1000 to 2000 cm^{-1}. The experiments showed large and small structural rearrangements of carbon-containing cathodes and their surfaces in the process of field emission. In addition to lines of the Raman spectra with frequency maxima in the known ranges: *G* (1581–1599 cm^{-1}), *D* (1363–1374 cm^{-1}) and *D'* (1619–1626 cm^{-1}), characteristic of carbon materials, a line was detected in the range 1450–1480 cm^{-1}, which is observed in the starting materials of pyrolytic graphite, carbon nanotube fibers and persists after operation, and also appears in a sample of micro-grained dense graphite after operation as a cathode. The relative integral intensity of line *D* in pyrolytic graphite, micrograined dense graphite, and carbon nanotube fibers undergoes the greatest change. In pyrolytic graphite and carbon nanotube fibers its increase is observed, and in micrograined dense graphite its decrease is observed after operation as a cathode. This made it possible to use the relative integral intensity of the *D*-line to quantify the change in the surface properties of carbon materials as a result of field emission when using these materials as cathodes, in particular to assess changes in crystallite sizes. Thus, the possibility of using Raman spectra to control the surface structure of carbon-containing materials has been demonstrated, which significantly facilitates the possibility of further analysis of the relationship between the surface structure and its emission characteristics. The prospects for improving the field emission characteristics of carbon-containing cathodes were discussed.

Keywords: field emission; field emission cathode; field emission current; volt-ampere characteristics; optical microscopy; raster (scanning) electron microscopy; Raman spectra; carbon-containing materials; nanostructured materials; surface structure.

For citation: Sheshin EP, Kundikova ND, Kireev VB, Belov KN, Many Fung Dyk, Berdnikov AS, Prosekov DN. Structural and field emission characteristics of carbon-containing cathodes. *Journal of Advanced Materials and Technologies*. 2024;9(1):023-036. DOI: 10.17277/jamt.2024.01.pp.023-036

Структурные и автоэмиссионные характеристики углеродсодержащих катодов

© Е. П. Шешин[a]✉, Н. Д. Кундикова[bc], В. Б. Киреев[a], К. Н. Белов[c], Фунг Дык Мань[a], А. С. Бердников[c], Д. Н. Просеков[c]

[a] *Московский физико-технический институт (НИУ), Институтский пер., 9, Долгопрудный, 141701, Российская Федерация;*
[b] *Институт электрофизики УрО РАН, ул. Амундсена, 106, Екатеринбург, 620016, Российская Федерация;*
[c] *Южно-Уральский государственный университет (НИУ), пр. Ленина, 76, Челябинск, 454080, Российская Федерация*

✉ sheshin.ep@mipt.ru

Аннотация: Проведено сопоставление автоэмиссионных и структурных характеристик поверхностей ряда углеродсодержащих, в том числе и наноструктурированных материалов, перспективных для использования при создании автокатодов со стабильными эмиссионными характеристиками. Исследовались волокна из углеродных

нанотрубок (УНТ-волокно), полиакрилонитрильные волокна, образцы пиролитического графита и мелкозернистого плотного графита (МПГ-6). Структура поверхности образцов исследовалась до и после их работы в качестве автокатода с использованием оптической микроскопии, растровой электронной микроскопии и спектроскопии комбинационного рассеяния. Эти результаты сопоставлялись с вольтамперными характеристиками соответствующих катодов. Оптическая и электронная микроскопия показали наличие крупномасштабных, а анализ спектров комбинационного рассеяния (СКР) – мелкомасштабных структурных перестроек катода и поверхности его материалов в процессе автоэмиссии. В спектральном диапазоне от 1000 до 2000 $см^{-1}$ в СКР кроме стандартно наблюдаемых характерных для углеродсодержащих материалов линий с максимумами частот в диапазонах 1363…1374 $см^{-1}$ (линия *D*), 1581…1599 $см^{-1}$ (линия *G*), 1619…1626 $см^{-1}$ (линия *D'*) обнаружена линия в интервале 1450…1480 $см^{-1}$ для пиролитического графита и УНТ-волокна – до и после эксплуатации, а для МПГ-6 – после эксплуатации этих материала в качестве автокатодов. Обсуждены изменения в СКР относительной интегральной интенсивности линии *D*, которая увеличивается для пиролитического графита и УНТ-волокна и уменьшается для МПГ-6 в процессе их эксплуатации в качестве автокатодов. Величина относительной интегральной интенсивности линии *D* использована для оценок размеров кристаллитов и их изменений в ходе автоэмиссии, что обосновывает возможность использования СКР для контроля структуры поверхности углеродсодержащих материалов и анализа связи структуры поверхности и ее эмиссионных характеристик. Обсуждены перспективы улучшения автоэмиссионных характеристик углеродсодержащих катодов.

Ключевые слова: автоэмиссия; автоэмиссионный катод; ток автоэмиссии; вольтамперная характеристика; оптическая микроскопия; растровая (сканирующая) электронная микроскопия; спектры комбинационного рассеяния; углеродсодержащие материалы; наноструктурированные материалы; структура поверхности.

Для цитирования: Sheshin EP, Kundikova ND, Kireev VB, Belov KN, Many Fung Dyk, Berdnikov AS, Prosekov DN. Structural and field emission characteristics of carbon-containing cathodes. *Journal of Advanced Materials and Technologies*. 2024;9(1):023-036. DOI: 10.17277/jamt.2024.01.pp.023-036

1. Introduction

The development and utilization of novel electrovacuum devices that leverage the field emission effect, encompassing diverse radiation sources like UV lasers [1], IR, visible, and UV cathodoluminescent lamps [2], as well as low-power X-ray tubes [3] for a range of applications, such as disinfection or the production of efficient X-ray radiation sources for various needs, appear to be highly pertinent. Indeed, the exploration of carbon-based (and nanostructured) materials for field emission cathodes is a promising area of research due to their unique electrophysical properties and potential applications in cathodoluminescent devices. In particular, the efficiency of the corresponding devices is greatly affected by the durability and stability of the emission characteristics of a number of carbon materials, which depend on the field emission modes that determine the structural changes of the emitting surface [4–6].

Since the type and parameters of nanostructures of the electron-emitting surface of carbon materials are crucial for their field emission characteristics, their evolution during field emission processes determines the dynamics of the field emission current change when a constant accelerating voltage is applied, and hence the stability of the operation of field emission devices based on carbon-containing materials. This makes it particularly relevant to study the surface changes of such materials during field emission and to identify the relationships between the surface structure and field emission characteristics of the corresponding carbon materials.

It is well known that along with various types of optical and electron microscopy, Raman spectroscopy can provide valuable information on the fine structure of carbon materials surfaces [7–22].

It should again be emphasised that the durability and stability parameters of field emission cathodes directly determine the competitiveness of new electrovacuum devices using the field emission effect, in particular, for radiation sources in various spectral ranges.

We have previously obtained expressions for the efficiency of the corresponding radiation sources of different types [2, 4, 5].

For example, for sources of visible, X-ray and UV radiation, the following ratio for the efficiency is valid:

$$Ef = \left(\frac{P}{S \times B} + \frac{P_{e1}}{E \times D} \right) \equiv (A + B)^{-1}, \quad (1)$$

where *Ef* is the value of light radiation source efficiency equal to the ratio of useful effect (of light or energy flow) to total costs, including installation, operation and disposal costs; $A \equiv \frac{P}{S \times T}$; $B \equiv \frac{P_{e1}}{E \times D}$; *P* is the sum of installation and disposal costs applied to one moment of time; *S* is the light flow in lumens (for

visible light sources) or energy in a given spectral range (for UV or X-ray sources); T is the continuous service life of the radiation source; P_{e1} is the cost per kWh of input energy in the absence of other operating costs; E is the light output (for visible light sources) or energy efficiency (for UV or X-ray sources); D is a discount factor reflecting the operating mode of the radiation source.

Estimates show that to ensure the competitiveness of general-purpose field emission light sources, a period of continuous stable operation of the radiation source – T must be ensured in the order of several tens of thousands of hours (preferably 50,000 hours and more).

This means that special attention should be paid to the issues of stable and long-term operation of field emission cathodes and identification of promising materials and modes of their operation. In particular, for carbon-containing materials of field emission cathodes, in the course of their operation during the emission of electrons, the structure of their surface and, together with it, the emission properties of the field emission cathode are changed and constantly renewed [2, 4–7].

This paper summarizes our results on the study of promising carbon-containing materials for field emission cathodes, including a comparative analysis of their field emission and structural characteristics, which can change during electron emission under different modes of field emission cathode operation.

The objective of the work was to compare the evolution of surface and field emission characteristics during the long-term process of electron field emission for different materials, namely to compare the experimentally obtained field emission characteristics of field emission cathodes and structural characteristics of the cathode and its surface using optical, scanning electron microscopy and Raman spectroscopy before and after long-term operation of the material as an field emission cathode. In addition to the new experimental results, we also used previously obtained results already published in [4–7].

2. Materials and Methods

2.1. Carbon materials for the field emission cathodes under study

In this work, as well as in [4–7], we used such nanomaterials as CNT filaments (carbon nanotube fibers) (FGBNU "TISNUM", Troitsk, Russia), with a diameter of about 30 μm, obtained by agglomeration of nanotubes; PAN-fibers (polyacrylonitrile fibers) ("Uglekhimvolokno", Mytishchi, Russia), which is a bundle of 200–300 polyacrylonitrile filaments each with a diameter of about 6 μm; and massive carbon materials (JSC NIIgraphite, Moscow, Russia): MPG-6 (high-strength fine-grained dense graphite) with a density of about 1.7 g·cm^{-3}, and pyrolytic graphite with a density of about 2.2 g·cm^{-3}.

2.2. Determining field emission characteristics of cathodes

The methods of preparation of cathodes from the investigated materials were described earlier [4–6]. The field emission characteristics were measured according to the two-electrode scheme in a vacuum chamber at a pressure of 10^{-6} Torr at a distance of 1 cm between the cathode from the investigated material and the anode, which is an electrode with a cathodoluminophore with a diameter (6.5 cm) significantly exceeding the dimensions of the emitting surface of the cathode (for different materials – cathodes with characteristic linear dimensions of the emitting surface from 1 to 6 mm).

When a positive voltage was applied to the anode, electrons were emitted from the cathode, and the current-voltage characteristics (CVC) and current-time dependencies were measured for different carbon-containing material cathodes.

2.3. Analysis of the structural characteristics of carbon-containing materials for field emission cathodes

The structural characteristics of the surface of carbon-containing field emission cathode materials and their evolution during electron emission were investigated using optical, scanning electron microscopy (SEM) and Raman spectroscopy.

Optical images of the surface of carbon-containing field emission cathode materials were recorded using an "Olympus" microscope, which allows obtaining digital images with magnification in the range up to 100× times. The magnifications of 5×; 10×; 20×; 50× and 100× times and the image sizes of the surface areas at the corresponding magnifications were used:

5× times – 2.8 × 2.2 mm;
10× times – 1.4 × 1.1 mm;
20× times – 700 × 550 μm;
50× times – 280 × 225 μm;
100× times – 140 × 112 μm.

Electron images of the microstructure of materials before and after their use as field emission cathodes were obtained at an accelerating voltage of 30 kV using a JEOL JSM 7001F scanning electron microscope in the same way as previously in [4–6].

The image field size of the scanning electron microscope using a focal length of 8 to 10 mm with sufficient image sharpness could vary in the range from 1 μm to several hundreds of μm.

This study continues the work presented in [7], using the same technique of obtaining and analysing Raman spectra using a ZNL Integra Spectra Raman spectrometer. Processing of the obtained Raman spectra was carried out using the software Fityk [8], which made it possible to extract individual lines of the spectrum assuming that the shape of each line is described by a Lorentz function, and to determine the maximum frequency, width and relative integrated intensity of each line of the spectrum in the frequency range 1000–2000 cm^{-1}. The characteristics of each line were determined at different background levels (at least three different levels), averaged with the estimation of maximum deviations from the mean values, which did not exceed 10 % for all experiments performed.

In this work, we have analysed in detail the spectral range of Raman spectra in the frequency range 1000–2000 cm^{-1}, which corresponds to the presence of the well-known *G*, *D* and *D'* lines [9, 10, 13–17] characteristic of carbon materials. It is also known that certain changes in the graphite structure of such materials are also reflected in the Raman spectra at frequencies around 2700 cm^{-1} [11]. However, no significant influence of auto-electron emission on the Raman spectra was found for the examined samples in this range and, therefore, it was decided to analyse in detail the line parameters in the Raman spectra in the frequency range 1000–2000 cm^{-1}, where we observed changes in the Raman spectrum as a result of using the examined samples as auto-electron emitters.

3. Results and Discussion

3.1. Structural and field emission characteristics of carbon-containing materials and cathodes made from them

3.1.1. Characteristics of fine-grained dense graphite MFG-6 and pyrolytic graphite

When recording the CVC of fine-grained dense graphite MPG-6 (curve *1* in Fig. 1) and pyrolytic graphite (curve *2* in Fig. 1), it was shown [6] that the threshold electric field strength of field emission for different samples of both types of materials is close in value in the range of 3600–3800 $V \cdot cm^{-1}$. At the same time, already at electric field strength of about 4500 $V \cdot cm^{-1}$ the value of field emission current density per unit of the emitting surface of the cathode for pyrolytic graphite exceeds several times the value of field emission current density for fine-grained dense graphite MFG-6. Examples of CVCs for samples of field emission cathodes made of fine-grained dense graphite MFG-6 and pyrolytic graphite with approximately the same areas of electron-emitting surfaces were published earlier in [6].

For microscopic inspection and registration of Raman spectra for each of the materials several observation points were selected. An example of the choice of points for recording the RMS for different samples of fine-grained dense graphite MFG-6 is presented in Fig. 1.

For microscopic inspection and recording of Raman spectra for each of the materials several observation points were selected. An example of the choice of points for recording the Raman spectra for different samples of fine-grained dense graphite MPG-6 is presented in Fig. 1.

It should be noted that for different registration points for both MPG-6 and pyrolytic graphite samples, although there are some differences in the images (optical and electronic photographs) of the surface, but no pronounced structural rearrangements before and after the emission processes can be detected, while for Raman spectra such differences are undoubtedly observed, which may indicate some heterogeneity of the surface of the initial materials, and possible heterogeneity of the structures of the surfaces of the materials after their work as field emission cathodes. This may be caused not only by the initial differences, but also by possible differences (inhomogeneities) formed in the course of structural changes of the material surface in the process of electron field emission (differences in the dynamics of structural changes for different parts of the surface).

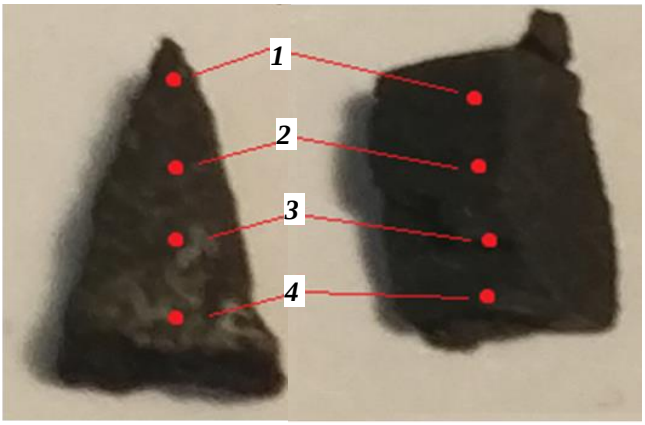

Fig. 1. Different samples of MPG-6:
on the left – sample used as an field emission cathode,
on the right – unused as an field emission cathode

Figures 2 and 3 show photographs, and Figs. 4, 5 show Raman spectra for different surface areas for fine-grained dense graphite MPG-6 (Figs. 2, 4) and pyrolytic graphite (Figs. 3, 5) before use as field emission cathodes and for samples of these materials already used as field emission cathodes.

Images of the surfaces of fine-grained dense graphite and pyrolytic graphite (Fig. 6) obtained by scanning electron microscopy also showed no significant differences for the different recording points both before and after the use of these materials as field emission cathodes. A typical view of the surfaces of these materials is presented in Fig. 6 (see also [4–6]).

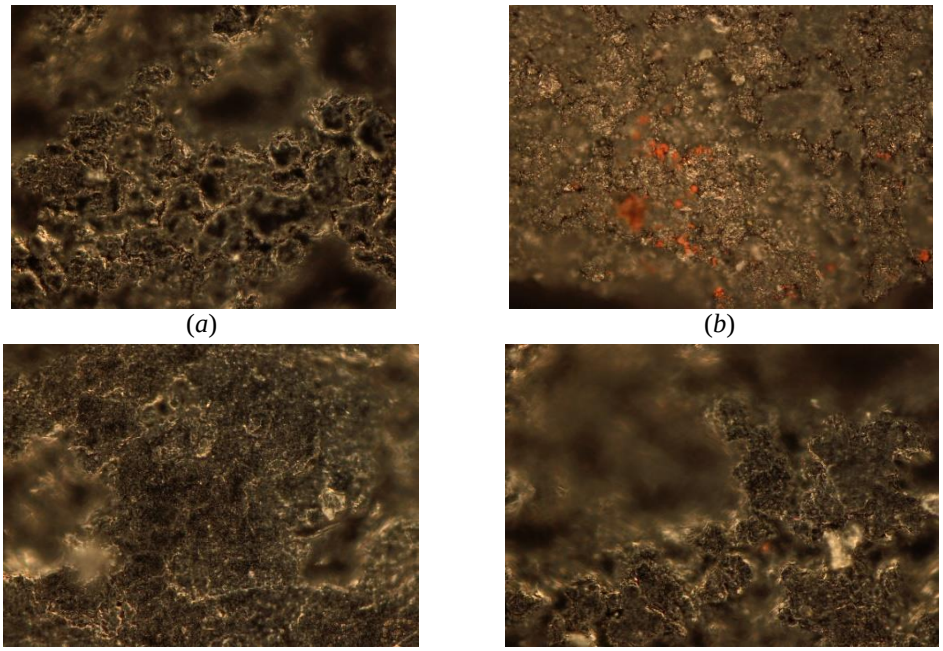

(*a*) (*b*) (*c*) (*d*)

Fig. 2. Surface views at 50× magnification of different sections of MPG-6 samples before use as an field emission cathode (*a*) and after use as an field emission cathode (*b*, *c*, *d*). Surface image size 280 × 225 μm

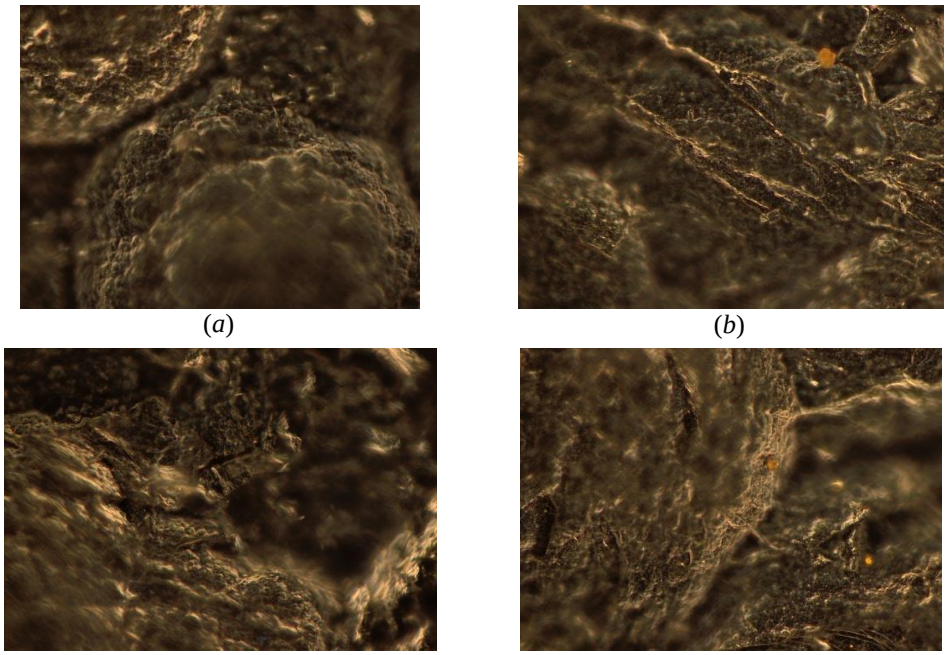

(*a*) (*b*) (*c*) (*d*)

Fig. 3. Surface view at 50× magnification of different sections of pyrolytic graphite samples before use as an field emission cathoede (*a*) and after use as an field emission cathode (*b*, *c*, *d*). Surface image size 280 × 225 μm

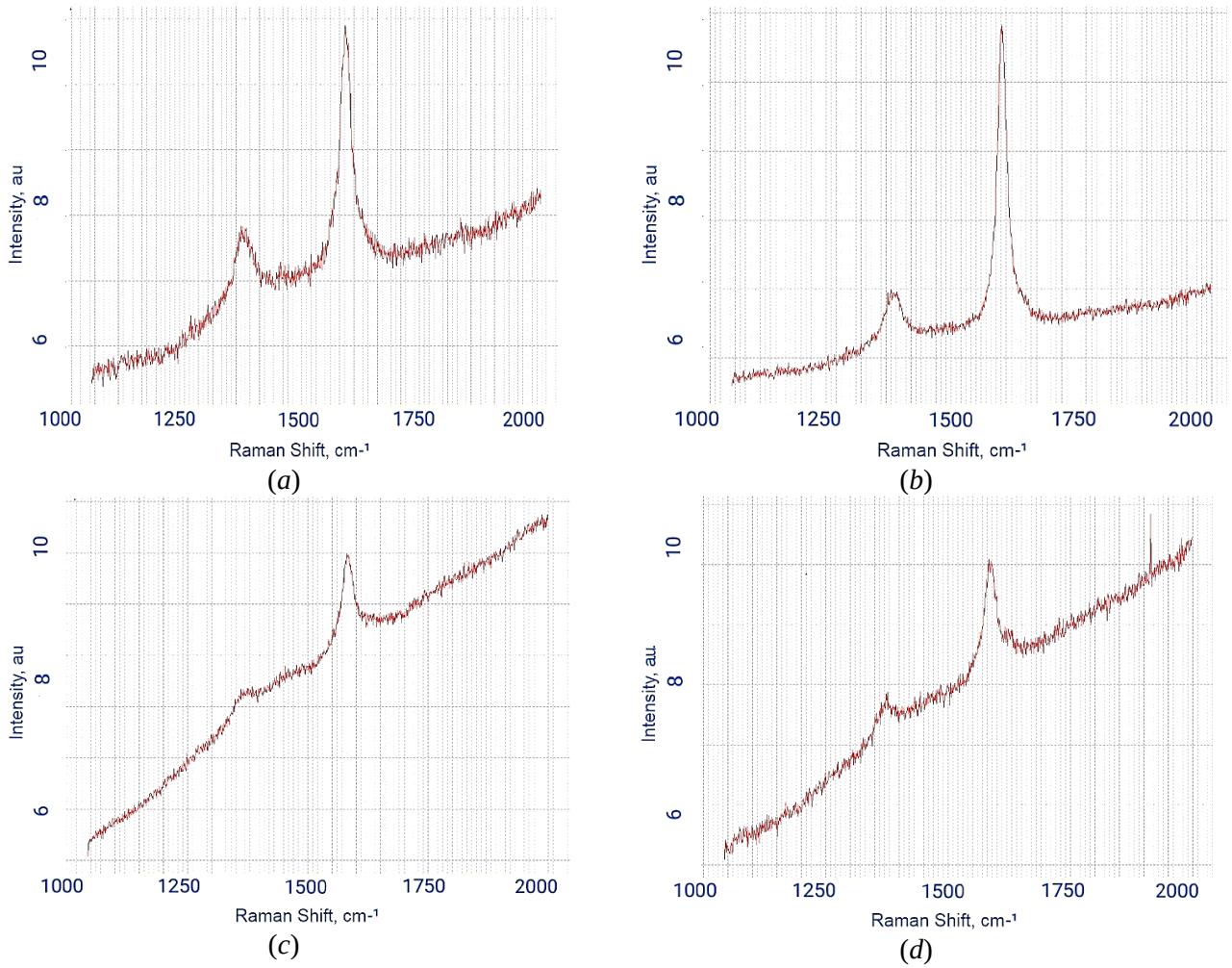

Fig. 4. Raman spectra of different sections of samples of fine-grained dense graphite MPG-6 before use as an field emission cathode (*a*, *b*) and after use as an field emission cathode (*c*, *d*) at points *1* (*a*, *c*) and 3 (*b*, *d*)

3.1.2. Characteristics of polyacrylonitrile fibers and carbon nanotube filaments

The structural and current-voltage characteristics of cathodes made of nanocarbon fibers and polyacrylonitrile fibers and the dynamics of emission current variation in time at different accelerating voltages in a two-electrode circuit were investigated. The data obtained earlier [4–6] and refined in this work show that the threshold electric field strength of field emission for samples from polyacrylonitrile fibers ranges from 1600 to 1850 V·cm^{-1}, and for carbon nanotube filaments from 500 to 600 V·cm^{-1}. At the same time, for carbon nanotube cathodes the CVC with increasing accelerating voltages, the emission current grows much faster than for polyacrylonitrile fibers. Moreover, for carbon nanotubes at a constant accelerating field strength of about 1300–1400 V·cm^{-1} the emission current increases compared to the initial value by 2–2.5 times within an hour and remains stable for several subsequent hours. In contrast, for cathodes made of polyacrylonitrile fibers at different accelerating voltages above the threshold values, a drop in the emission current over time is observed either immediately or after some increase (in the time interval of about an hour) and relative stabilisation within two to three subsequent hours. Photographs of the surfaces of the corresponding electrode materials obtained by optical microscopy and Raman spectra of such materials as carbon nanotubes and polyacrylonitrile fibers before and after their operation as field emission cathodes are presented, respectively, in Figs. 7, 8.

The analysis of optically and SEM-recorded images of carbon nanotube cathodes and polyacrylonitrile fibers cathodes obtained in [4–6] and in this work show that as a result of long-lasting electron field emission during prolonged operation of cathodes made of these materials there is a well-observed structural rearrangement of the cathode as a whole (Figs. 7, 8) and of individual fibers (Figs. 9, 10, combined from the data of our publications [4–6]).

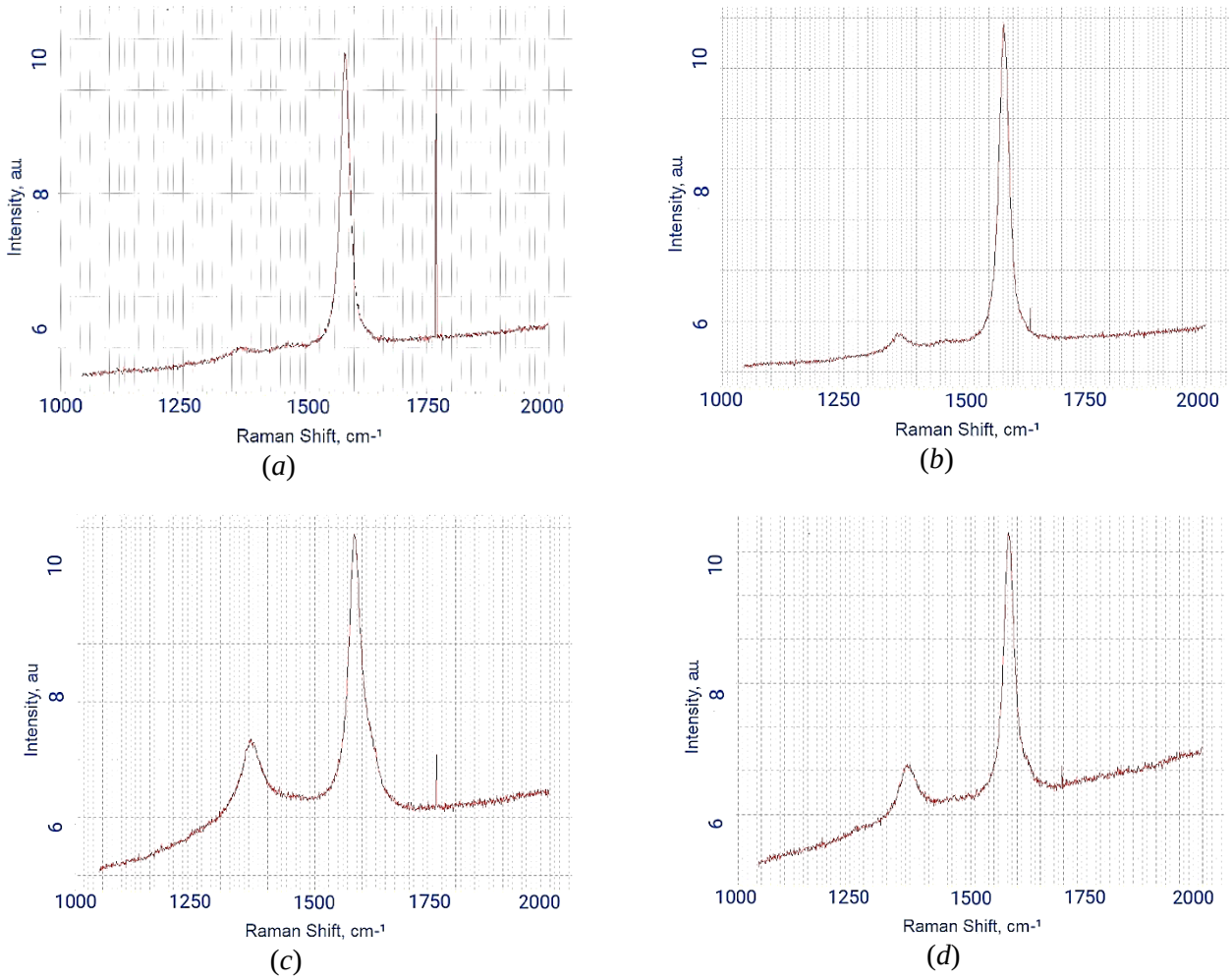

Fig. 5. Raman spectra of pyrolytic graphite samples before use as an field emission cathode (*a*, *b*) and after use as an field emission cathode (*c*, *d*) at points *1* (*a*, *c*) and *3* (*b*, *d*)

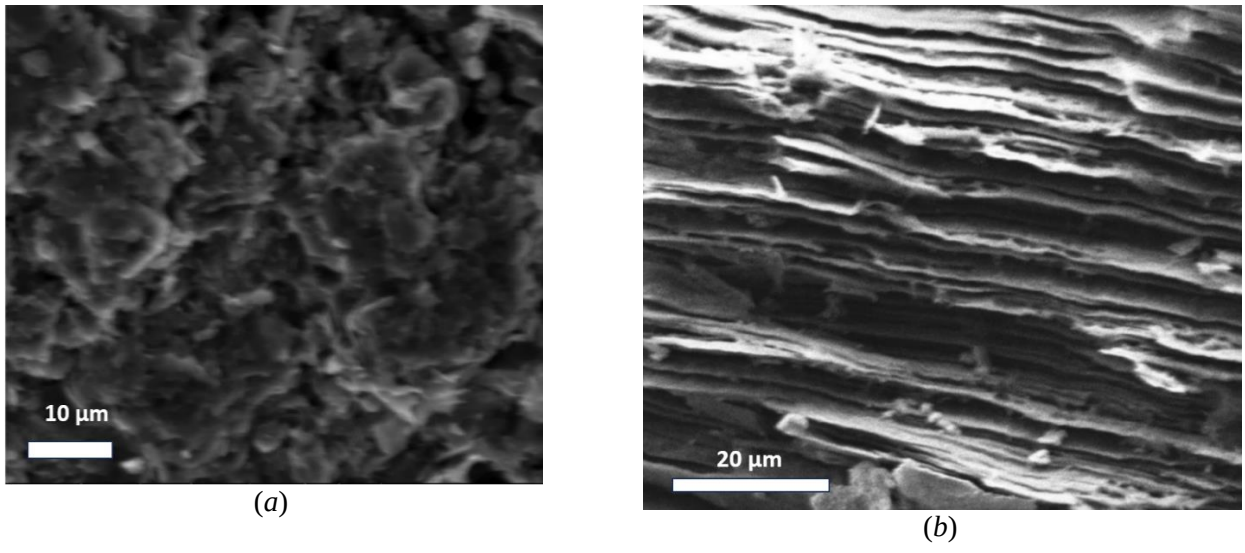

Fig. 6. Photos of cathode surfaces from arrays of fine-grained dense graphite MPG-6 (*a*) and pyrolytic graphite (*b*) obtained by SEM

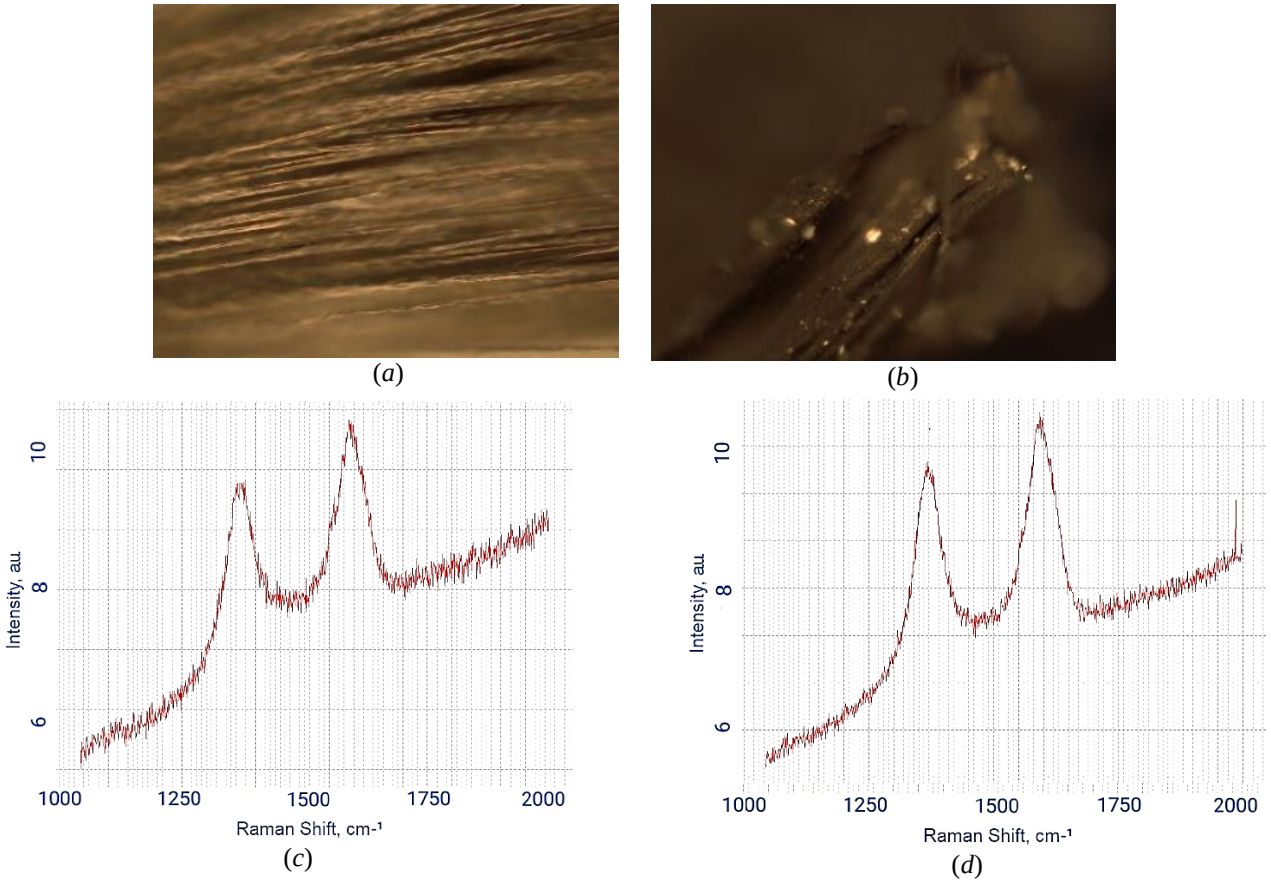

Fig. 7. Optical microscopy (*a* and *b*) (20× magnification) of a polyacrylonitrile fibers cathode and Raman spectra (*c* and *d*) of this fibers before (*a* and *c*) and after (*b* and *d*) its use as an field emission cathode material (The size of the surface section is 700 × 550 μm)

The images obtained by optical microscopy and SEM show that as a result of field emission processes polyacrylonitrile fibers melt, because during prolonged operation of these fibers as field emission cathodes at sufficiently high accelerating voltages they are heated above the melting point, which leads to their structural degradation and deterioration of their field emission properties. These conclusions are fully consistent with the above-described changes of the field emission current in time for field emission cathodes made of this material.

On the contrary, for the cathode based on carbon nanotube filaments, emission properties improve with time. This correlates well with the disordered structure of the field emission cathode and the destruction of carbon nanotubes during long-term field emission of electrons from this material, since a large number of new effective emission centers are apparently formed during disordered structure of the field emission cathode and destruction of carbon nanotubes. The change in the structure and the cathode itself and the structural rearrangement of the individual carbon nanotube are very well observed in the images of Figures 8 and 10, obtained by optical and scanning electron microscopy.

3.2. Discussion of the results obtained

The efficiency of using field emission cathodes in various electronic devices, and hence the relationship between field emission characteristics, operating modes and stability of field emission cathodes, especially those made of nanostructured carbon-containing materials, have been discussed in numerous publications, including [2–6, 23–30].

A comparison of the field emission characteristics of carbon-containing materials, in particular those studied in this work, demonstrates a certain inconsistency. On the one hand, cathodes made from arrays of carbon-containing materials such as fine-grained dense graphite MPG-6 and pyrolytic graphite have a threshold for the occurrence of emission current (the minimum electric field strength that ensures the occurrence of field emission current) significantly higher than that for cathodes made from nanostructured fibers, such like polyacrylonitrile fibers (about a three-fold difference) and especially for carbon nanotube filaments (about a six-fold difference).

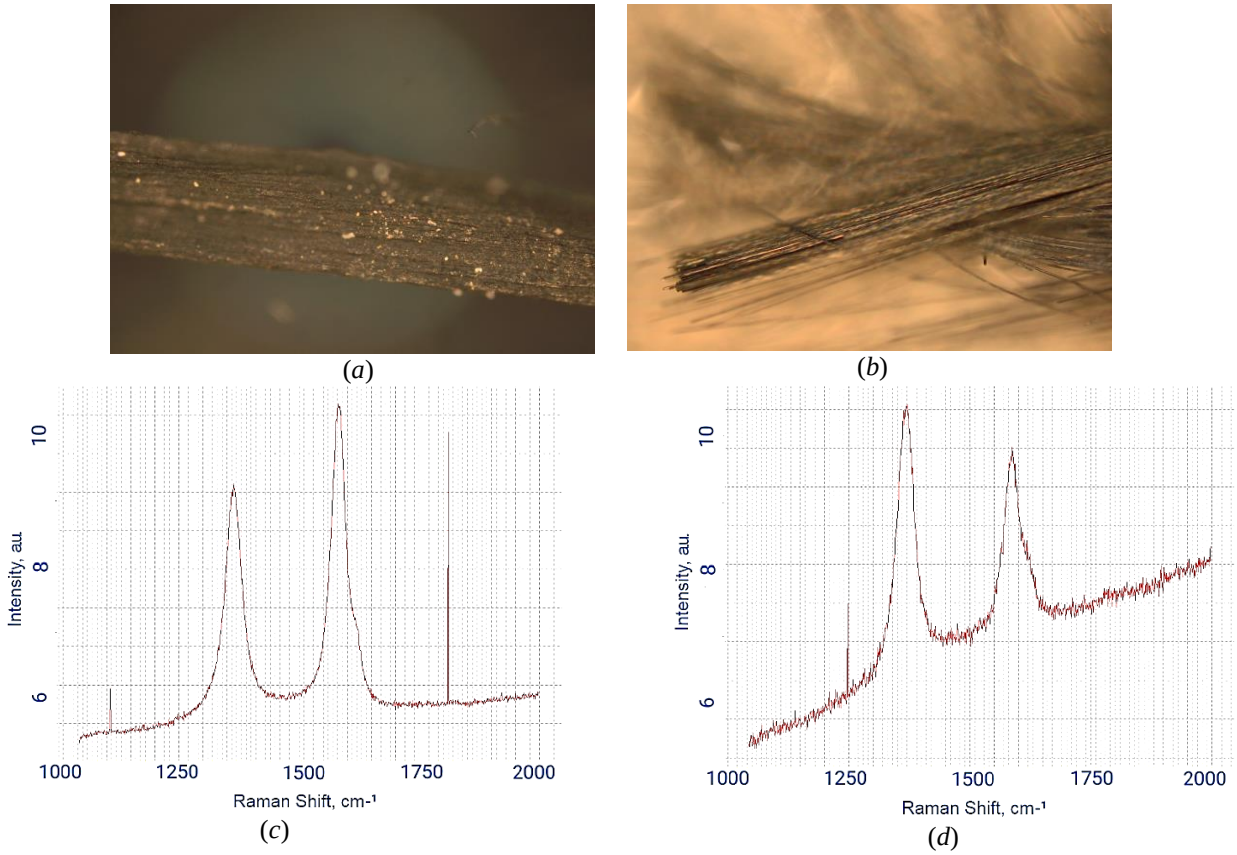

(*a*) (*b*) (*c*) (*d*)

Fig. 8. Optical microscopy (*a* and *b*) (10× magnification) of carbon nanotube cathode and Raman spectra (*c* and *d*) for carbon nanotubes (CNT filaments) before (*a* and *c*), after (*b* and *d*) their use as an field emission cathode material (The size of the surface section is 1.4 × 1.1 mm)

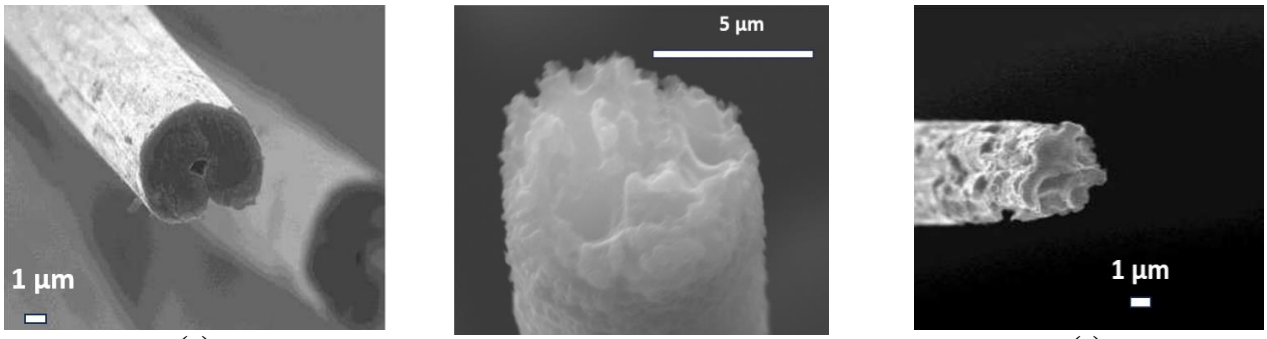

(*a*) (*b*) (*c*)

Fig. 9. SEM images of polyacrylonitrile fibers before (*a*) and after (*b*, *c* – at different emission process duration) the operation of fibers as part of the field emission cathode

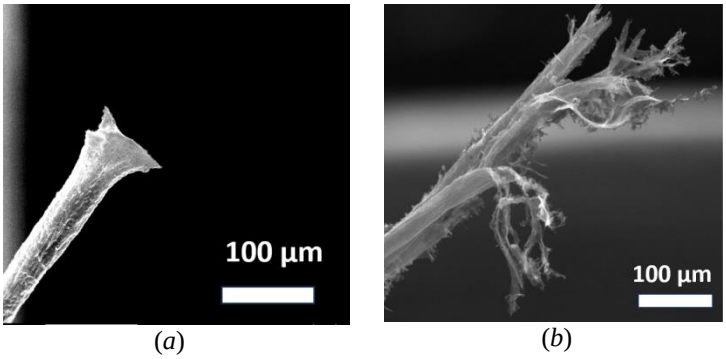

(*a*) (*b*)

Fig. 10. SEM images of individual carbon nanotubes before (*a*) and after (*b*) the operation of these nanotubes as part of the field emission cathode

Table 1. Raman spectra data for samples of carbon-containing field emission cathode materials in the range 1000–2000 cm^{-1}

Peak, cm^{-1}	Pyrographite		PAN-fibers		MPG-6		CNT-fibers	
	before work	after work	before work	after work	before work	after work	before work	after work
D	1364.9	1366.8	1370.1	1373.2	1366.1	1366.8	1363.6	1367.6
X	1458.1	1458.5	NA	NA	NA	1454.8	1476.2	1462.5
G	1581.7	1584.7	1592.6	1599.0	1583.0	1583.5	1582.1	1586.4
D′	нет	1624.4	нет	нет	1616.9	1625.3	1619.8	1621.1

On the other hand, the field emission characteristics of massive cathodes made of carbon-containing materials are much more stable in a wide range of accelerating field strengths, although the field emission current for carbon nanotube filaments can be increased by an order of magnitude in a much narrower range of accelerating electric field strengths than even for the best of field emission cathode massive materials – pyrolytic graphite.

It should also be noted that although higher field emission current densities can be achieved for field emission cathodes made of nanostructured fibers, it is clear that at such current densities, macroscopic disturbances in the structure of both the nanofiber cathode itself and individual fibers occur.

For polyacrylonitrile fibers, this is melting and degradation of their field emission properties. For individual carbon nanotubes, these are numerous breaks, which, within the interval of several hours of operation of the field emission cathode, not only do not deteriorate its initial field emission properties, but can even improve them. This, however, does not guarantee the stability of the field emission cathode for tens of thousands of hours required for the effective operation of many field emission devices [2, 3].

When analyzing the Raman spectra, which records summary is presented in Table 1, the main Raman scattering lines in the range 1000–2000 cm^{-1} were considered. The maximum frequencies of the lines detected in the Raman spectra were obtained, as in our work [7], by averaging over all recording points of samples of the corresponding materials that were not used in the operation of field cathodes (in the table, the columns “before use”), and those used as field cathodes (in the table there are columns “after use”). In this work, with an increase in the number of samples and recording points in the studied samples in comparison with work [7], the characteristic values of the previously obtained frequencies of the maxima of the corresponding spectral lines were confirmed with an accuracy of 0.5 cm^{-1}, which corresponds to the instrumental accuracy of the Raman spectrometer “Integra Spectrum” with a diffraction grating of 1800 lines·mm^{-1}.

According to the results presented in Table 1, along with the well-known *G*, *D*, and *D′* lines [9, 10] characteristic of carbon materials, the following has been observed:

– *G* line with a maximum in the range 1581–1599 cm^{-1}, due to vibrations of carbon atoms in strongly bonded hexagonal planes;

– *D* line with a maximum in the range 1363–1374 cm^{-1}, caused by violations of translational symmetry in the studied materials;

– *D′* line with a maximum in the range 1619–1626 cm^{-1}, caused by disorder effects between carbon layers;

in the Raman spectra of samples of such materials as pyrographite, carbon nanotubes, and fine-grained dense graphite MPG-6, after use in an field emission cathode, a characteristic spectral line in the frequency range of 1450–1480 cm^{-1} was observed, labelled by us in the table, as well as in [7], the X-line. In [12], a similar line was observed in Raman spectra for samples of polyacrylonitrile fibers (unlike our data) and was associated with vibrations of the methylene group.

The frequencies of the maxima of the corresponding spectral lines and their insignificant shifts as a result of using the materials as field emission cathodes were briefly discussed earlier [7].

The most interesting observed effect from Raman spectroscopy data for the studied materials is the change in the relative integrated intensity of the *D* line with respect to the *G* line. In [9], the relative integrated intensity of the *D* line for fine-grained graphite is related to the size of its crystallites. The results of measuring the relative integral intensity of the *D* line before and after prolonged electron emission for all investigated samples of carbon-containing materials tested as materials for field emission cathodes are presented in Fig. 11.

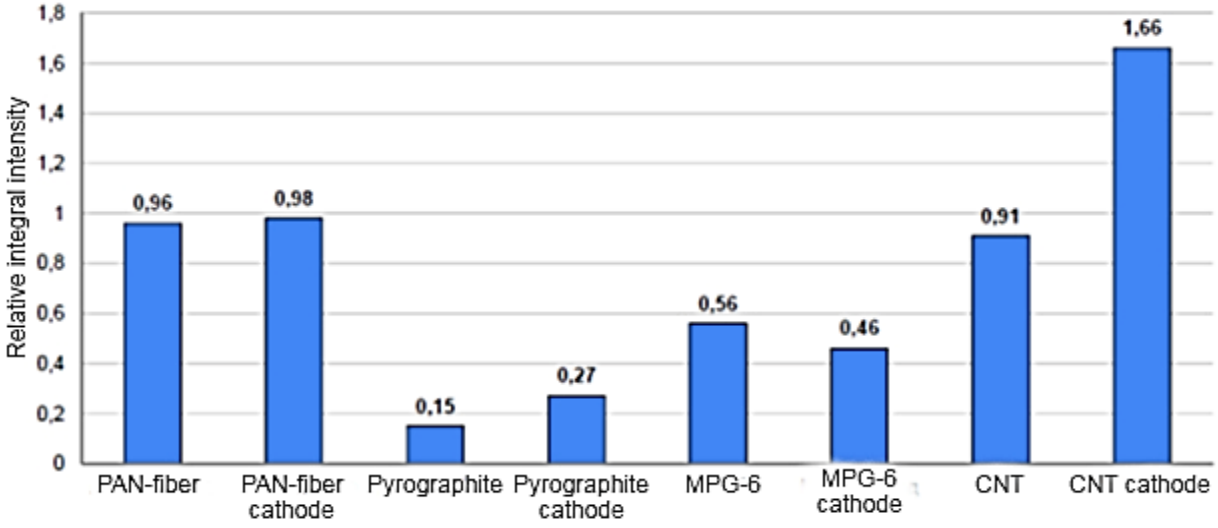

Fig. 11. Relative integral intensity of the *D* line before and after (cathode) long-term electron emission for all investigated samples of carbon-containing materials tested as materials for field emission cathodes

Voltampere characteristics and studies of current evolution over time show that a rather high current stability is observed in the range of voltages used for pyrolytic graphite and MPG-6, which is confirmed by relative macroscopic structural stability according to optical and scanning electron microscopy data. Nevertheless, the RSM data show that some small scale structural rearrangement occurs during operation of these materials, which is most likely related to the change in crystallite sizes.

The sizes of the average crystallites in this material before its operation as an field emission cathodes – 7.9 nm, and after – 9.6 nm – were estimated by the method proposed in [9] for fine-grained dense graphite using the data in Fig. 11.

Thus, the analysis of the relative integral intensity of the *D* line of Raman spectra of carbon materials allowed us to quantitatively estimate not only the average sizes of carbon crystallites in massive samples of MPG-6, but also the evolution of these sizes in the process of field emission.

Although the intensity of the *D* line in pyrographite is much lower than in fine-grained dense graphite MPG-6, it can be assumed that for this material the crystallite sizes are significantly smaller. This correlates with higher values of the field emission current under similar conditions and with the fact that pyrographite consists of layers of carbon crystallites, that pyrographite consists of layers with a thickness of about 1 μm, and the characteristic size of particles from which fine-grained dense graphite MPG-6 is compressed is about 50 μm, although, as our estimates show, the characteristic sizes of crystallites for these materials are much smaller. Moreover, the increase in the relative integral intensity of the D line as a result of prolonged electron emission may indicate for pyrographite a decrease in the size of emission centres during the operation of this material as an field emission cathode, although this question requires more detailed elaboration and additional studies.

The question of interpreting the significant increase in the relative integral intensity of the D line as a result of long-term electron emission for carbon nanotubes also remains open, since the legitimacy of applying the concept of crystallites to nanotubes raises some doubts. However, for fibers, structural analysis shows significant both large-scale and small-scale restructuring of the cathode and its surface. Moreover, PAN fiber sintering is observed in a number of modes, but for CNT fiber a strong macroscopic fiber disorder accompanied by the rupture of nanotubes and an improvement in field emission characteristics is characteristic, at least in a time interval of several hours.

Moreover, for each of the materials studied, it is possible to select operating modes and design solutions (for example, providing effective heat removal for field emission cathodes made of polyacrylonitrile fibers, preventing overheating and melting of this material) allowing the use of these materials to create effective field emission devices.

Of particular importance in this case is the study of their field emission characteristics, the dynamics of their changes and the associated structural rearrangements of their surface under various operating conditions of these materials as field cathode materials. Without knowledge of these characteristics, it is impossible to select appropriate operating modes that ensure the efficient use of these

materials in the creation of new field emission devices and devices.

Obtaining data on the field emission and structural characteristics of the surface of carbon-containing materials for field emission cathodes creates good prerequisites for optimizing the operation of field emission cathodes created on the basis of various carbon-containing materials, in particular, the use of a three-electrode circuit allows for various materials to provide the necessary field emission current by appropriately changing the voltage and distance between the cathode and mesh. By changing the shape, size of the cathode area, and the mode of excitation of the emission current, it is possible to provide the necessary density of this current, which allows avoiding excessive overheating and the occurrence of unacceptable mechanical stresses leading to destruction of the structures of the cathode materials.

4. Conclusion

The results obtained indicate that for carbon-containing materials, when used as field emission cathodes, both macroscopic and microscopic structural changes of the cathodes themselves and their surfaces occur, depending on the type of material and the mode of its operation. It is shown that measuring the relative integral intensity of the D line in Raman spectra makes it possible to evaluate the nature of the evolution of emission electron centers, and in some cases to estimate not only the sizes of carbon crystallites, but also the change in these sizes during the field emission process. It was found that for MPG-6 samples before and after using this material as the cathode of a field emission light source, the average crystallite size is different, and according to estimates, it is approximately 8 nm and 10 nm, respectively. The results obtained justify the possibility of using optical and scanning electron microscopy methods and methods of analyzing Raman spectra for a detailed study of the structure of field emission cathodes made of carbon materials and their surfaces, including the possibility of studying changes in their structure under different modes of their operation as cathodes of field emission radiation sources.

5. Funding

This study received no external funding.

6. Conflict of interests

The authors declare no conflict of interest.

References

1. Jmerik V, Kozlovsky V, Wang X. Electron-beam-pumped UVC emitters based on an (Al,Ga)N material system. *Nanomaterials*. 2023;13:1-42. DOI:10.3390/nano13142080

2. Bugaev AS, Kireev VB, Sheshin EP, Kolodyazhnyj AJ. Cathodoluminescent light sources: status and prospects. *Physics-Uspekhi*. 2015;58(8):792-818. DOI:10.3367/UFNe.0185.201508e.0853

3. Bugaev AS, Eroshkin PA, Romanko VA, Sheshin EP. Low-power X-ray tubes (the current state). *Physics-Uspekhi*. 2013;56(7):691-703. DOI:10.3367/UFNe.0183.201307c.0727

4. Kireev VB, Sheshin EP. Nanomaterials for effective auto-emission cathodoluminescent disinfecting light sources. *Scienceosphere*. 2022;4(1):1-12. DOI:10.5281/zenodo.6390489 (In Russ.)

5. Taikin AYu, Savichev IA, Popov MA, Anokhin EM, et al. Comparison and analysis of field emission characteristics of carbon cathodes based on PAN fiber and CNT filaments. *Journal of Advanced Materials and Technologies*. 2022;7(1):46-57. DOI:10.17277/jamt.2022.01.pp.046-057

6. Kireev VB, Sheshin EP. Field emission cathodoluminescent lamps: II. Nanostructured materials for field emission cathodes. *In Malkova MYu. (ed.) Engineering systems-2022: Proceedings of the International Conference. Engineering Systems-2022, 6-8 April 2022, Moscow,Russia*. Peoples' Friendship University of Russia; 2022. p.56-66. (In Russ.)

7. Belov KN, Berdnikov AS, Kireev VB, Kundikova ND, et al. Raman spectra of carbon materials used as cathodes of field emission radiation sources. *Bulletin of SUSU. Series "Mathematics. Mechanics. Physics"*. 2023;15(2):230206(41-47) DOI:10.14529/mmph230206 (In Russ.)

8. Wojdyr M. Fityk: A general-purpose peak fitting program. *Journal of Applied Crystallography*. 2010;43:1126-1128. DOI: 10.1107/S0021889810030499

9. Jawhari T, Roid A, Casado J. Raman spectroscopic characterization of some commercially available carbon black materials. *Carbon*. 1995;33(11):1561-1565.

10. Bokobza L, Bruneel J-L, Couzi M. Raman spectroscopy as a tool for the analysis of carbon-based materials (highly oriented pyrolitic graphite, multilayer graphene and multiwall carbon nanotubes) and of some of their elastomeric composites. *Vibrational Spectroscopy*. 2014;74:57-63. DOI:10.1016/j.vibspec.2014.07.009

11. Komlenok M, Kurochitsky N, Pivovarov P, Rybin M, Obraztsova E. Field electron emission from crumpled CVD graphene patterns printed via laser-induced forward transfer. *Nanomaterials*. 2022;12(11):1-8. DOI:10.3390/nano12111934

12. Panapoy M, Dankeaw A, Ksapabutr B. Electrical conductivity of PAN-based carbon nanofibers prepared by electrospinning method. *Thammasat International Journal of Science and Technology*. 2008;13:11-17.

13. Dyachkova TP, Khan YA, Burakova EA, Galunin EV, et al. Characteristics of epoxy composites containing carbon nanotubes/graphene mixtures. *Polymers (Basel)*. 2023;15(6):1-20. DOI:10.3390/polym15061476

14. Pimenta MA, Dresselhaus G, Dresselhaus MS, Cançado LG, et al. Studying disorder in graphite-based systems by Raman spectroscopy. *Physical Chemistry Chemical Physics*. 2007;9:1276-1290. DOI:10.1039/B613962K

15. Keszler AM, Nemes L, Ahmad SR, Fang X. Characterisation of carbon nanotube materials by Raman spectroscopy and microscopy – A case study of multiwalled and singlewalled samples. *Journal of Optoelectronics and Advanced Materials*. 2004;6:269-1274.

16. Hayashida K, Nagaoka S, Ishitani H. Growth and oxidation of graphitic crystallites in soot particles within a laminar diffusion flame. *Fuel*. 2014;128:148-154. DOI:10.1016/j.fuel.2014.03.008

17. Malard M, Pimenta MA, Dresselhaus G, Dresselhaus MS. Raman spectroscopy in graphene. *Physics Reports*. 2009;473:51-87. DOI:10.1016/j.physrep.2009.02.003

18. Gorelik VS, Sushchinskiĭ MM. Raman scattering of light in crystals. *Soviet Physics Uspekhi.* 1969;12:399-429. DOI:10.1070/PU1969v012n03ABEH003897

19. Kudelski A. Analytical applications of Raman spectroscopy. *Talanta*. 2008;76(1):1-8. DOI:10.1016/j.talanta.2008.02.042

20. Gorelik VS, Skrabatun AV, Bi D. Raman scattering of light in diamond microcrystals. *Crystallography Reports*. 2019;64:428-432. DOI:10.1134/S106377451903009X

21. Moris-Muttoni B, Raimbourg H, Champallier R, Augier R, et al. The effect of strain on the crystallinity of carbonaceous matter: Application of Raman spectroscopy to deformation experiments. *Tectonophysics*. 2023;869(230126):1-24. DOI:10.1016/j.tecto.2023.230126

22. Gibson RF, Ayorinde EO, Wen Y.-F. Vibrations of carbon nanotubes and their composites: A review. *Composites Science and Technology*. 2007;67(1):1-28. DOI:10.1016/j.compscitech.2006.03.031

23. Saito Y, Uemura S. Field emission from carbon nanotubes and its application to electron sources. *Carbon*. 2000;38(2):169-182. DOI: 10.1016/S0008-6223(99)00139-6

24. Wang ZL, Gao RP, De Heer WA, Poncharal P. In situ imaging of field emission from individual carbon nanotubes and their structural damage. *Applied Physics Letters*. 2002;80(5):856-858. DOI:10.1063/1.1446994

25. Silva SRP, Carey JD, Guo X, Tsang WM, Poa CHP. Electron field emission from carbon-based materials. *Thin Solid Films*. 2005;482(1–2):79-85. DOI:10.1016/j.tsf.2004.11.122

26. Le Normand F, Cojocaru CS, Fleaca C, Li JQ, et al. A comparative study of the field emission properties of aligned carbon nanostructures films, from carbon nanotubes to diamond. *The European Physical Journal Applied Physics*. 2007;38(2):15-27. DOI:10.1051/epjap:2007052

27. Kaur G, Pulagara NV, Kumar R, Lahiri I. Metal foam-carbon nanotube-reduced graphene oxide hierarchical structures for efficient field emission. *Diamond and Related Materials*. 2020;106:1-10. DOI:10.1016/j.diamond.2020.107847

28. Dwivedi N, Dhand C, Carey JD, Anderson EC, et al. The rise of carbon materials for field emission. *Journal of Materials Chemistry C*. 2021;9(8):620-659. DOI:10.1039/d0tc05873d

29. Ma Z, Li D, Zhang H, Wurz P, et al. Study of a low-energy collimated beam electron source and its application in a stable ionisation gauge. *Vacuum*. 2023;215:1-7. DOI:10.1016/j.vacuum.2023.112302

30. Xiao D, Du H, Sun L, Suo X, et al. Boosting the electron beam transmittance of field emission cathode using a self-charging gate. *Nature Communications*. 2024;15(764):1-10. DOI:10.1038/s41467-024-45142-0

Information about the authors / Информация об авторах

Evgeny P. Sheshin, D. Sc. (Phys. and Math.), Professor, Deputy Head Department of Vacuum Electronics, Head Laboratory of Vacuum and Microwave Electronics, Moscow Institute of Physics and Technology (National Research University) (MIPT), Moscow, Russian Federation; ORCID 0000-0003-2750-4797; e-mail: sheshin.ep@mipt.ru

Шешин Евгений Павлович, доктор физико-математических наук, профессор, заместитель заведующего кафедрой вакуумной электроники, заведующий лабораторией вакуумной и СВЧ-электроники, Московский физико-технический институт (Национальный исследовательский университет) (МФТИ), Москва, Российская Федерация; ORCID:0000-0003-2750-4797; e-mail: sheshin.ep@mipt.ru

Nataliya D. Kundikova, D. Sc. (Phys. and Math.), Professor, Head Department of Optoinformation, South Ural State University (National Research University) (SUSU), Chelyabinsk, Chief Researcher, Head Laboratory of Nonlinear Optics, Institute of Electrophysics, Ural Branch of the Russian Academy of Sciences, Ekaterinburg, Russian Federation; ORCID 0000-0002-5880-9393;e-mail: kundikovand@susu.ru

Viktor B. Kireev, Cand. Sc. (Phys. and Math.), Associate Professor, MIPT, Moscow, Russian Federation; ORCID 0000-0002-0699-2819; e-mail: kireev.vb@mipt.ru

Kirill N. Belov, Postgraduate, SUSU, Chelyabinsk, Russian Federation; ORCID 0009-0003-1915-5061; e-mail: belovkn@susu.ru

Fung Dyk Many, Postgraduate, MIPT, Moscow, Russian Federation; e-mail: phungducmanh@phystech.edu

Alexey S. Berdnikov, Student, SUSU, Chelyabinsk, Russian Federation; e-mail: berdnikovas@susu.ru

Danila N. Prosekov, Student, SUSU, Chelyabinsk, Russian Federation; e-mail: prosekov97@mail.ru

Кундикова Наталия Дмитриевна, доктор физико-математических наук, профессор, заведующий кафедрой оптоинформатики Южно-Уральского государственного университета (Национальный исследовательский университет) (ЮУрГУ), Челябинск, главный научный сотрудник, заведующий лабораторией нелинейной оптики, Институт электрофизики УрО РАН, Екатеринбург, Российская Федерация; ORCID 0000-0002-5880-9393; e-mail: kundikovand@susu.ru

Киреев Виктор Борисович, кандидат физико-математических наук, доцент, МФТИ, Москва, Российская Федерация; ORCID 0000-0002-0699-2819; e-mail: kireev.vb@mipt.ru

Белов Кирилл Николаевич, аспирант, ЮУрГУ, Челябинск, Российская Федерация; ORCID 0009-0003-1915-5061; e-mail: belovkn@susu.ru

Фунг Дык Мань, аспирант, МФТИ, Москва, Российская Федерация; e-mail: phungducmanh@ phystech.edu

Бердников Алексей Сергеевич, студент, ЮУрГУ, Челябинск, Российская Федерация; e-mail: berdnikovas@susu.ru

Просеков Данила Николаевич, студент, ЮУрГУ, Челябинск, Российская Федерация; e-mail: prosekov97@mail.ru

Received 13 December 2023; Accepted 16 February 2024; Published 26 April 2024

Original papers
Advanced structural materials, materials for extreme conditions

УДК 667.6 DOI: 10.17277/jamt.2024.01.pp.037-043

The influence of filler type on performance properties of thin-layer polymer composites

© Raisa G. Domnichenko[a], Olga V. Karmanova[b]✉, Sergey G. Tikhomirov[b]

[a] *Lugansk State University named after Vladimir Dal, 20 A, Youth quarter, Lugansk, 91034, Lugansk People's Republic, Russian Federation,*
[b] *Voronezh State University of Engineering Technologies, 19, Revolution Avenue, Voronezh, 394036, Russian Federation*

✉ karolga@mail.ru

Abstract: The study aims to establish the impact of environmental factors on the properties of operational stability of coatings based on aqueous dispersions, depending on the surface properties of the filler used. The dispersion of acrylic latex and epoxy resin preliminarily emulsified with sodium polyacrylate was taken as the basis. Dispersion was carried out at a temperature of 60°C. Crushed marble, sedimentary chalk, chemically precipitated chalk and grade kaolin were used as fillers. The hardener was polyethylenepolyamine. Compounding was carried out in a laboratory dissolver: a filler was introduced into the dispersion, and then it was dispersed. The hardener was introduced immediately before coating. As a result, the degree of influence on the coating properties was established. The process of hydrophilization of the coating surface due to the oxidation of the polymer phase was studied. The operational reliability of coatings under the action of aggressive factors depending on the filler was evaluated. It is shown that when calcium carbonate is replaced by kaolin, an increase in the resistance to defective coatings is observed, and adhesion remains at a high level. It has been established that the influence of environmental factors on the properties of the coating are arranged in the following order: thermal and moisture aging > action of electrolyte solutions > action of ultraviolet. Under ultraviolet light, hydrophilization of the coating surface occurs due to the oxidation of the polymer phase.

Keywords: water-dispersion coatings; kaolin; crushed marble; calcium carbonate; epoxy resin; thermal aging; electrolyte action; ultraviolet.

For citation: Domnichenko RG, Karmanova OV, Tikhomirov SG. The influence of filler type on performance properties of thin-layer polymer composites. *Journal of Advanced Materials and Technologies*. 2024;9(1):037-043. DOI: 10.17277/jamt.2024.01.pp.037-043

Влияние наполнителей на эксплуатационные свойства тонкослойных полимерных композитов

© Р. Г. Домниченко[a], О. В. Карманова[b]✉, С. Г. Тихомиров[b]

[a] *Луганский государственный университет имени Владимира Даля, кв. Молодежный, 20А, Луганск, 91034, Луганская Народная Республика, Российская Федерация,*
[b] *Воронежский государственный университет инженерных технологий, пр. Революции, 19, Воронеж, 394036, Российская Федерация*

✉ karolga@mail.ru

Аннотация: Работа посвящена исследованию влияния факторов окружающей среды на эксплуатационные свойства покрытий на основе водных дисперсий, полученных в присутствии наполнителей разного типа. В качестве полимерной основы использовали дисперсию акрилового латекса и эпоксидной смолы, предварительно эмульгированную с полиакрилатом натрия. Диспергирование осуществляли при температуре 60 °С. В качестве наполнителей использовали дробленый мрамор, осадочный мел, химически осаждённый мел, каолин. Отвердителем служил полиэтиленполиамин. Компаундирование осуществляли в лабораторном

дисольвере: в дисперсию вводили наполнитель, после чего осуществляли его диспергирование. Отвердитель вводили непосредственно перед нанесением покрытий. Исследовано влияние выбранных наполнителей на свойства получаемых покрытий. Изучен процесс гидрофилизации поверхности покрытия, протекающий за счет окисления полимерной фазы. Оценена эксплуатационная надежность покрытий при действии агрессивных факторов в зависимости от типа наполнителя. Показано, что при замене карбоната кальция каолином наблюдается повышение устойчивости покрытий к образованию дефектов, при этом адгезионные свойства сохраняется на высоком уровне. Установлено, что по влиянию на свойства покрытия факторы окружающей среды располагаются в ряду: тепло-влажностное старение > действие растворов электролитов > действие ультрафиолета. Под действием ультрафиолета имеет место гидрофилизация поверхности покрытия за счет окисления полимерной фазы.

Ключевые слова: водно-дисперсионные покрытия; каолин; дробленный мрамор; карбонат кальция; эпоксидная смола; тепловое старение; действие электролитов; ультрафиолет.

Для цитирования: Domnichenko RG, Karmanova OV, Tikhomirov SG. The influence of filler type on performance properties of thin-layer polymer composites. *Journal of Advanced Materials and Technologies*. 2024;9(1):037-043. DOI: 10.17277/jamt.2024.01.pp.037-043

1. Introduction

Coatings based on film-forming polymers obtained by removing the solvent or dispersion medium after application to the substrate differ in their performance properties from coatings made from melts. First of all, this applies to thin-layer coatings based on aqueous dispersions, with a film formed due to sequential processes of dispersion dehydration, deformation of dispersed particles of the polymer phase and their fusion [1, 2]. Obviously, at the fusion site the material will be characterized by structural defects, as well as an increased content of stabilizers and other targeted additives [3, 4]. A similar situation is observed at the boundary of the interphase contact with the filler surface, which, obviously, will affect the performance properties of such coatings, especially their resistance to external aggressive factors – ultraviolet radiation, moisture, temperature, electrolytes, etc. [5, 6].

The properties of cured coatings can be flexibly controlled through the use of mixed film formers. For example, there are known systems based on acrylic polymer – liquid glass, which exhibit a sufficient degree of vapor permeability and at the same time are impermeable to liquid [9]. Systems based on alkyd and polyurethane polymers demonstrate sufficient flexibility, while achieving a significant reduction in material costs compared to pure urethane ones. The properties of cured coatings can be flexibly controlled through the use of mixed film formers. For example, there are known systems based on acrylic polymer – liquid glass, which exhibit a sufficient degree of vapor permeability and at the same time are impermeable to liquid [9]. Systems based on alkyd and polyurethane polymers exhibit sufficient flexibility, while achieving a significant reduction in material costs compared to pure urethane ones.

The nature and condition of the film former determines such characteristics of the coating as wear resistance, mechanical strength, resistance to aggressive environments, corrosion resistance, moisture resistance, elasticity, hardness, etc. [10].

These characteristics and the corresponding consumer properties of film formers can be significantly changed by adding functional additives to the coating, of which fillers occupy the most significant place [11].

The use of fillers not only improves the performance characteristics of the coating, but also increases the profitability of the paint and varnish material (paints and varnishes), since the price of fillers varies within 0.20–0.25 % of the price of the film former, especially when using local carbonate and silicate-type raw materials for their receiving [12, 13].

In modern paints and varnishes, the degree of filling can be increased to 50–60 % wt. and provide significant savings on expensive polymer [14–16].

It should be noted that the type of filler and its quantity determine the protective properties of the coating: liquid and vapor permeability, mechanical properties (strength, hardness, elasticity), adhesive strength between the coating and substrates, as well as the operational reliability of paintwork materials, assessed by such indicators as water resistance, corrosion stability, resistance to atmospheric factors [17, 18].

The influence of fillers on the structure of the coating and changes in its properties is associated primarily with the nature of their distribution in the polymer matrix, as well as with the interaction of dispersed fillers with the film-forming substance [19–21]. Consequently, increasing the stability of the interphase contact of the film former with the filler surface is a task, the solution of which will make it possible to control the operational reliability of such thin-layer systems. The purpose of this study was to establish the influence of environmental factors on the properties and operational stability of coatings based on aqueous dispersions, depending on the surface properties of the filler used.

2. Materials and Methods

2.1. Initial components

As a basis for obtaining the compositions, we used a hybrid dispersion based on acrylic latex UcarDL 450 (Dow Chemical, Germany, supplier LOTOS Trading LLC, Troitsk) and epoxy resin ED-20 (FKP Sverdlov Plant, Dzerzhinsk), pre-emulsified in the presence of 3 wt. % sodium polyacrylate (NPP Spetsavia LLC, Tver region). As a filler, components widely used in industry were chosen based on crushed marble (Normcal-20, produced by SomCalcite, Turkey), sedimentary chalk MMS-1 (Volcheyarovsky quarry, Lugansk region), chemically precipitated chalk (CPC) (Reaktiv LLC, Slavyansk) and kaolin grade KS-1 (JSC Microcalcite, Magnitogorsk).

2.2. Coating formation

Compounding was carried out in a laboratory dissolver: the filler was introduced into the dispersion at a speed of 300–400 rpm, after which it was dispersed at a speed of 1200 rpm for 15 minutes. Before applying the coatings, the hardener polyethylenepolyamine – PEPA (PJSC "Uralchimplast", Nizhny Tagil) was introduced into them in an equivalent amount, which was calculated according to the method [7].

To determine the basic properties of the coating, it was formed by spraying paintwork onto the prepared plates in one layer and dried in three stages:

I: at a temperature of (20 ± 2) °C for 2 hours;

II: at a temperature of (90+2) °C in a drying cabinet for 1 hour;

III: at a temperature of (20+2) °C for 1 hour. The thickness of the single-layer film after drying is 50–70 microns.

2.3. Instruments and research methods

The structure of fillers and polymer coatings was studied using a Specord IR 75 infrared spectrophotometer (Carl Zeiss, Germany). For dispersed fillers, tableted samples with KBr were used. For film formers and composite materials, spectra of free films with a thickness of 40–50 microns were obtained.

The specific surface area of dispersed materials was determined using a NOVA 2200 device (Quantachrome Corp. USA). Dispersity and granulometric composition were studied by optical microscopy using a JSM-5610 LV electron microscope with an EDX JED-2201 chemical analysis system (JEOL, Japan). The contact angle of the surface with liquids was determined using a DIP-6 measuring microscope with a goniometric attachment (JSC LOMO, St. Petersburg).

The oil absorption capacity of the fillers was determined in accordance with Russian Standard 21119.8-75 (ISO 787-5-80). The method consists of gradually adding linseed oil to a sample of the test product, grinding them with a stick until a homogeneous mass is formed and determining the amount of oil consumed.

The moisture absorption of the free film was determined in accordance with Russian Standard 21513-76 on samples 3 cm wide, weighing 0.3–0.5 g. Samples in bottles were weighed on an analytical balance with an accuracy of 0.0001 g, after which they were placed in a desiccator with a relative humidity (95 ± 2) % and after 24 hours weighed again to constant weight. Moisture absorption was calculated using the formula:

$$a = \frac{m_2 - m_1}{m_1 - m_0} \cdot 100,$$

where m_0 is weight of empty bottle, g; m_1 is weight of the bottle with film before testing, g; m_2 is weight of the bottle with film after keeping in a desiccator, g.

The adhesion of films to a metal substrate was determined by the method of grid cuts according to Russian Standard 15140-78 using a RMI-5 tensile testing machine (Polimermash Group LLC, St. Petersburg). The impact strength of coatings was determined using a U-1 device (Non-Destructive Control LLC, Yekaterinburg).

3. Results and Discussion

It has been found that carbonate fillers differ in the content of impurities. In particular, X-ray fluorescence analysis showed that the calcium content in the Normcal-20 sample was 99.1 wt. %, which was higher than that of the MMC-1 sample (98.0 wt. %).); the amount of silicon in Normcal-20 was up to 0.8 wt. % versus 1.2 and 0.9 wt. % for MMC-1 and CPC, respectively.

Based on the IR spectra, the corresponding differences in the parameters of the absorption bands responsible for the vibrations of the main structure-forming bonds of the carbonate anion were identified (Fig. 1): a noticeable shift in the maximum of the band for Normcal-20: a decrease in the wave number $1/\lambda = 1425$ cm^{-1} to 1495 cm^{-1} for CPC. The ratio of their intensities (I_0/I) decreased accordingly from 45.33 to 35.25. The energy spectrum of vibrations of

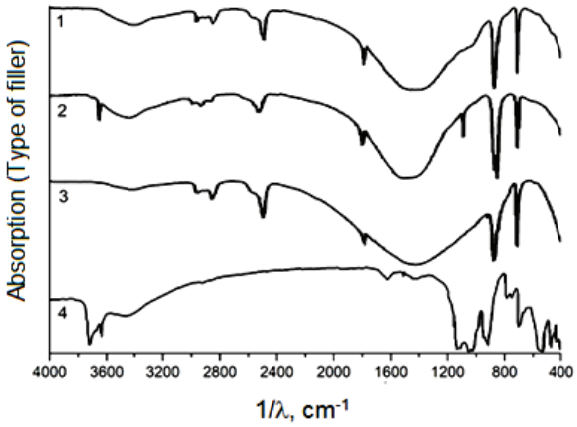

Fig. 1. IR-spectra of fillers:
1 – MMC-1; *2* – CPC; *3* – Normcal-20; *4* – kaolin KS-1

structural bonds also narrowed. The half-width of these same absorption bands decreased by 400 cm^{-1} for CPC and 235 cm^{-1} for MMC-1 chalk. The change in the parameters of the remaining bands was less pronounced.

The presence of hydroxyl groups on the surface was detected only in the case of chemically deposited chalk (absorption band at 3643 cm^{-1} with intensity ratio $I_0/I = 0.23$) (Fig. 1).

The maximum amount of adsorbed water ($I_0/I = 0.34$) was found in the CPC composition, and the minimum was found in Normcal-20 ($I_0/I = 0.09$). Judging by the position of the absorption bands responsible for the stretching vibrations of adsorbed water, it is noted that it is most firmly bound by the surfaces of CPC and MMC-1 (band at 3423 cm^{-1}). For ground marble, the absorption maximum is shifted by 18 cm^{-1} to the region of higher frequencies.

The IR spectrum of kaolin (Fig. 1) of the KS-1 grade contains absorption bands responsible for vibrations of surface and structural hydroxyl groups bound by silicon and aluminum atoms, as well as water [8]. It is these functional groups and compounds, as is known [9], that, together with the chemical composition and structural-chemical structure, determine the basic physicochemical properties of the surface of kaolins, namely: bands at 3680 and 3640 cm^{-1} are stretching vibrations of internal surface structural hydroxyl groups; maximum at 3613 cm^{-1} is vibrations of internal OH groups of the kaolin set; the maxima at 926 and 900 cm^{-1} are due to deformation vibrations of the structural hydroxyl groups of kaolinite associated with octahedral Al^{3+} cations; the bands at 3440 and 1605 cm^{-1} belong to stretching and bending vibrations of adsorbed water, respectively.

The analysis of the granulometric composition of natural mineral fillers showed that the content of the fraction from 0 to 5 microns in the composition of MMS-1 was 61.5 wt. %, and for kaolin KS-1 it was 28.7 wt. %.

It was found that the minimum specific surface area (Table 1) was observed in Normcal-20, which is 3 times less than that of MMC-1, 5 times less than that of CPC and 8.5 times less than that of kaolin KS-1.

The noted features of the composition and structure of the studied fillers influence their physicochemical properties in the dispersed state (Table 1).

It was found that kaolin had the lowest water contact angle with respect to water ($\theta = 43°$). Calcium carbonates are more hydrophilic and are characterized by close values of contact angles, taking into account the error in measuring this indicator by the Washburn method, which does not exceed 3 degrees. The development of the surface and its polarity determine the physicochemical properties of the filler. The values of the dielectric loss tangent confirm the higher surface energy of kaolin compared to carbonates, of which sedimentary chalk and crushed marble turned out to be the least active. In particular, the moisture absorption of kaolin was greater compared to calcium carbonates: with Normcal-20 – 4.7 times; with CPC – 2.5 times.

In terms of oil absorption capacity, kaolin was somewhat inferior to chemically precipitated chalk and was almost twice as high as Normcal-20 and MMC-1.

The ultraviolet radiation factor is one of the main factors determining weather resistance. Under test conditions (intensity of total ultraviolet radiation 54 $W \cdot m^{-2}$, exposure 20 hours at 60 °C and relative humidity 35 %) the performance properties of epoxy-acrylic coatings changed significantly (Table 2).

The effect of UV radiation on coatings was photo-oxidation of the polymer part, which was accompanied by an increase in its polarity, and, consequently, in contact angles. This effect was more pronounced for composites with carbonate filler, which can be explained by the greater activity of the kaolin surface in terms of neutralizing peroxide radicals [8, 9]. An increase in the defectiveness of coatings also led to an increase in water absorption by 30–35 % for carbonates and by 16 % for kaolin. Accordingly, the impact strength indicator also decreased, but the most vulnerable under test conditions was adhesion, which for all coatings decreased by 21–23 %. Noteworthy is the fact that the adhesion index of coatings filled with kaolin decreased to a greater extent compared to the index of coatings obtained in the presence of other fillers.

Table 1. Physical and chemical properties of the surface of dispersed fillers

Type of filler	Properties*					
	θ, degree	S_{ads}, $m^2 \cdot g^{-1}$	tgδ	*W*, wt. %	*A*, $g \cdot g^{-1}$	*X*, $g \cdot (100\ g)^{-1}$
Sedimentary chalk MMS-1	26	2.15	0.018	1.56	0.70	23
Chemically precipitated chalk	31	3.18	0.035	1.70	1.65	57
Crushed marble Normcal-20	30	1.40	0.019	0.90	0.41	19
Kaolin KS-1	43	15.08	0.193	4.20	–	44

* θ is water contact angle; S_{ads} is BET specific surface area; tgδ is dielectric loss tangent; *W* is moisture absorption; *A* is water adsorption; *X* is oil absorption capacity.

Table 2. Changes in the physical and technical properties of filled epoxy-acrylic coatings under the influence of UV radiation

Type of filler	Properties*			
	θ, degree	Δ, wt. %	*P*, N·m	σ_A, MPa
Sedimentary chalk MMS-1	60 / 50	1.4 / 2.1	19.5 / 18.6	7.26 / 5.77
Crushed marble Normcal-20	65 / 59	1.3 / 2.0	20.6 / 18.6	7.32 / 5.85
Kaolin KS-1	83 / 76	2.1 / 2.5	23.8 / 22.0	7.64 / 5.51

* θ is water contact angle; *W* is moisture absorption in 24 hours; *P* is impact strength; σ_A is adhesion; in the denominator – data after testing, in the numerator – initial data.

Table 3. Corrosion resistance of filled epoxy-acrylic coatings

Type of filler	Properties			
	θ, degree	*W*, wt. %	*P*, N·m	σ_A, MPa
Sedimentary chalk MMS-1	60 / 58	1.4 / 1.5	19.5 / 19.3	7.26 / 6.84
Crushed marble Normcal-20	65 / 63	1.3 / 1.4	20.6 / 19.1	7.32 / 6.45
Kaolin KS-1	83 / 77	2.1 / 2.2	23.8 / 21.9	7.64 / 6.92

Table 4. Changes in the properties of filled epoxy-acrylic coatings in the process of thermal and moisture aging

Type of filler	Properties			
	θ, degree	W, wt. %	P, N·m	σ_A, MPa
Sedimentary chalk MMS-1	60 / 57	1.4 / 1.5	19.5 / 18.9	7.26 / 7.20
Crushed marble Normcal-20	65 / 61	1.3 / 1.6	20.6 / 19.0	7.32 / 7.23
Kaolin KS-1	83 / 80	2.1 / 2.4	23.8 / 22.4	7.64 / 7.61

When exposed to sodium chloride coatings of 3 wt. % for 120 hours, there was a weaker hydrophilization of their surface than in the case of UV radiation (Table 3).

At the same time, there was no significant change in the defectiveness of the structure, which is confirmed by a slight change in the water absorption index (within the error limits of the method). The same patterns of changes in properties were observed for indicators of impact strength and adhesion. For kaolin compositions, adhesion remained at a fairly high level, decreasing by only 9 %.

It has been established that the aging of the coating under the influence of the heat and humidity

factor (24 hours at a temperature of 100 °C and relative humidity 100 %, Russian Standard 9.401) was least pronounced compared to the action of UV radiation and immersion in an electrolyte solution (Table 4).

The change in the values of water contact angles was on the limit of the measurement error, that is, under the influence of heat and humidity aging, significant destruction of the polymer did not occur. Water absorption of coatings increased, probably due to the accumulation of diffusing water at the interfaces. This effect was most pronounced (19 %) when using filler with a minimum surface activity – crushed marble. The adhesion index of coatings to the substrate remained at a high level with virtually no changes.

4. Conclusion

Thus, it has been found that, according to the degree of influence on the properties of coatings, the effects of external factors are arranged in increasing order: heat and humidity aging > the effect of electrolyte solutions (3 wt. % NaCl) > the effect of ultraviolet radiation. Moreover, only in the latter case significant hydrophilization of the coating surface due to oxidation of the polymer phase was observed.

The operational reliability of coatings under the influence of the listed aggressive factors depends, among other things, on the type of filler used. It has been shown that when replacing calcium carbonate with a relatively inactive surface with kaolin, an increase in resistance to increasing defectiveness of coatings under the influence of all three considered factors is observed, and adhesion remains at a high level. In general, we can conclude that increasing the orienting ability of the filler surface is one of the ways to increase the operational reliability of polymer compositions.

5. Funding

This study received no external funding.

6. Conflict of interests

The authors declare no conflict of interest.

References

1. Smolka P, Musilová L, Mráček A, Sedláček T. Stability of aqueous polymeric dispersions for ultra-thin coating of bi-axially oriented polyethylene terephthalate films. *Coatings*. 2017;7(12):234. DOI:10.3390/coatings7120234

2. The main task is to provide the industry with raw materials. *Lakokrasochnyye materialy i ikh primeneniye.* 2022;11(549):22-23 (In Russ.)

3. Steward PA, Hearn J, Wilkinson MC. An overview of polymer latex film formation and properties. *Advances in Colloid and Interface Science*. 2000;86(3):195-267. DOI:10.1016/S0001-8686(99)00037-8

4. Jiao C, Sun L, Shao Q, Song J, et al. Advances in waterborne acrylic resins: Synthesis principle, modification strategies, and their applications. *ACS Omega*. 2021;6(4):2443-2449. DOI:10.1021/acsomega.0c05593

5. Vojtovich VA, Hryapchenkova IN. And water-dispersioned will be called revolutionary. *Lakokrasochnye materialy i ikh primenenie*. 2023;5(554):20-24 (In Russ.)

6. Ma YK, Rigolet S, Michelin L, Paillaud JL, Mintova S, et al. Facile and fast determination of Si/Al ratio of zeolites using FTIR spectroscopy technique. *Microporous and Mesoporous Materials*. 2021;311:110683. DOI:10.1016/j.micromeso.2020.110683

7. Maier C, Calafut T. Fillers and reinforcements. In: *Polypropylene*. NY: Plastics Design Library; 1998. p. 49-56.

8. Rudawska A. Experimental study of mechanical properties of epoxy compounds modified with calcium carbonate and carbon after hygrothermal exposure. *Materials*. 2020;13(23):5439. DOI:10.3390/ma13235439

9. Rothon R, Paynter C. Calcium carbonate fillers. In: *Fillers for Polymer Applications*. UK: Springer Cham; 2017. p. 149-160. DOI:10.1007/978-3-319-28117-9_35

10. Hu Z, Zen X, Gong J, Deng Y. Water resistance improvement of paper by superhydrophobic modification with microsized $CaCO_3$ and fatty acid coating. *Colloids and Surfaces A: Physicochemical and Engineering Aspects*. 2009;1-3(351):65-70.

11. Kovrizhkina NA, Kuznetsova VA, Silaeva AA, Marchenko SA. Ways to improve the properties of paint coatings by adding different fillers (review). *Aviation materials and technologies*. 2019;4(57):41-48. DOI: 10.18577/2071-9140-2019-0-4-41-48

12. Didik OM. Chemically precipitated calcium carbonate (chalk) as a high-quality functional additive for solvent-diluentable and water-dispersive paints. *Lakokrasochnye materialy i ikh primenenie*. 2018;7-8:50-51. (In Russ.)

13. Stroganov VF, Amel`chenko MO, Ligina TZ, Naumkina NI. Possibility of regulating technological and operational properties of styrene-acrylic paints when using kaolins of various types of activation. *Izvestiya Kazanskogo gosudarstvennogo arkhitekturno-stroitel'nogo universiteta*. 2016;2(36):207-211. (In Russ.)

14. Fujitani T. Stability of pigment and resin dispersions in waterborne paint. *Progress in Organic Coatings*. 1996;1-4(29):97-105. DOI:10.1016/S0300-9440(96)00661-3

15. Miniotatie R. *Vapour permeability and water absorption of different exterior paint systems*. Available from: https://webpages.tuni.fi/nsb2011/sites/www.tut.fi.nsb2011/files/b5_02_miniotaite.pdf [Accessed 10 January 2024]

16. Alvarez V, Paulis M. Effect of acrylic binder type and calcium carbonate filler amount on the properties of paint-like blends. *Progress in Organic Coatings*. 2017;112:210-218. DOI:10.1016/j.porgcoat.2017.07.023

17. Geurts J, Bouman J, Overbeek A. New waterborne acrylic binders for Zero VOC paints. *Journal of Coatings Technology and Research*. 2007;1(5):57-63. DOI:10.1007/s11998-007-9036-x

18. Rudawska A. Experimental study of mechanical properties of epoxy compounds modified with calcium carbonate and carbon after hygrothermal exposure. *Materials.* 2020;13(23):5439. DOI:10.3390/ma13235439

19. Saikia BJ, Parthasarathy G. Fourier transform infrared spectroscopic characterization of kaolinite from Assam and Meghalaya, Northeastern India. *Journal of Modern Physics*. 2010;1(4):206-210. DOI:10.4236/jmp.2010.14031

20. Rissa K, Lepistö T, Yrjölä K. Effect of kaolin content on structure and functional properties of water-based coatings. *Progress in Organic Coatings*. 2006;55(2):137-141. DOI:10.1016/j.porgcoat.2005.09.009

21. Merezhko N, Sirenko S, Shulga O. Analysis of properties of modified kaolins and water-dispersion paints developed on their base. *Eastern-European Journal of Enterprise Technologies*. 2016;5(6):11-16. DOI:10.15587/1729-4061.2016.79358

Information about the authors / Информация об авторах

Raisa G. Domnichenko, Senior Lecturer, Lugansk State University named after Vladimir Dal, Lugansk, Lugansk People's Republic, Russian Federation; ORCID 0009-0003-9919-3083; e-mail: raisa-domnichenko@yandex.com

Olga V. Karmanova, D. Sc. (Eng.), Professor, Voronezh State University of Engineering Technologies, Voronezh, Russian Federation; ORCID 0000-0003-2226-6582; e-mail: karolga@mail.ru

Sergey G. Tikhomirov, D. Sc. (Eng.), Professor, Voronezh State University of Engineering Technologies, Voronezh, Russian Federation; ORCID 0000-0002-8192-0049; e-mail: tikhomirov_57@mail.ru

Домниченко Раиса Григорьевна, старший преподаватель, Луганский государственный университет им. Владимира Даля, Луганск, Луганская Народная Республика, Российская Федерация; ORCID 0009-0003-9919-3083; e-mail: raisa-domnichenko@yandex.com

Карманова Ольга Викторовна, доктор технических наук, профессор, Воронежский государственный университет инженерных технологий, Воронеж, Российская Федерация; ORCID 0000-0003-2226-6582; e-mail:karolga@mail.ru

Тихомиров Сергей Германович, доктор технических наук, профессор, Воронежский государственный университет инженерных технологий, Воронеж, Российская Федерация; ORCID 0000-0002-8192-0049; e-mail: tikhomirov_57@mail.ru

Received 30 January 2024; Accepted 29 February 2024; Published 26 April 2024

Original papers
Manufacturing processes and systems

УДК 621.6.04.001.5 DOI: 10.17277/jamt.2024.01.pp.044-059

Mechanisms and kinetics of particle separation by size and density in an activated gravity flow of granular material

© Oleg O. Ivanov[a], Viktor N. Dolgunin[b]✉, Konstantin A. Kudi[c]

[a] *ANO "Vdokhnoviteli", 1, Trudovaya St., Korolev, Moscow region, 141071, Russian Federation,*
[b] *Tambov State Technical University, 1, Leningradskaya St., Tambov, 392000, Russian Federation,*
[c] *PJSC "MTS Bank", Bld. 1, 18, Andropova Av., Moscow, 115432, Russian Federation*

✉ dolgunin-vn@yandex.ru

Abstract: A study was carried out to examine the effects of interaction and efficiency of the particle separation process by size and density in fast gravity flows activated by longitudinal momentum by acting the particles of the open surface of the flow with a rough conveyor belt. It has been established that the momentum effect leads to a zone formation in the central part of the flow. The zone has extremely high values of the shear rate and the gradient of the voids fraction, ensuring an intensive occurrence of the quasi-diffusion separation effect. In the region adjacent to the base of the flow, momentum action leads to a decrease in the proportion of voids and an increase in the shear rate, which contributes to the intensification of particle size segregation. In the flow region adjacent to the surface of the momentum action, high values of the voids fraction and the temperature of the granular medium provide favorable conditions for the occurrence of quasi-diffusion effects of mixing and separation. As a result of momentum action, the separation efficiency increases if the direction of the quasi-diffusion separation and segregation flows coincides (separation by density), and the efficiency decreases when the directions of these flows are different (separation by size). With increasing intensity of the momentum action, the zone of intense shear deepens, and the efficiency of density separation increases, reaching its maximum value when the zone deepens by 0.5–0.55 of the layer thickness. With a further increase in the intensity of the momentum action, the separation efficiency decreases due to the expansion of the flow region in which the effect of quasi-diffusion mixing dominates. The conclusions based on the experimental results are confirmed by the method of mathematical modeling of the dynamics of particle separation by density in an activated gravity flow.

Keywords: granular material; activated gravity flow; longitudinal momentum; separation by size and density; segregation; quasi-diffusion separation; shear rate; void volume fraction.

For citation: Ivanov OO, Dolgunin VN, Kudi KA. Mechanisms and kinetics of particle separation by size and density in an activated gravitational flow of granular material. *Journal of Advanced Materials and Technologies*. 2024;9(1):044-059. DOI: 10.17277/jamt.2024.01.pp.044-059

Механизмы и кинетика сепарации частиц по размеру и плотности в активированном гравитационном потоке зернистого материала

© О. О. Иванов[a], В. Н. Долгунин[b]✉, К. А. Куди[c]

[a] *АНО «Вдохновители», ул. Трудовая, 1, Королев, Московская область, 141071, Российская Федерация,*
[b] *Тамбовский государственный технический университет,*
ул. Ленинградская, 1, Тамбов, 392000, Российская Федерация
[c] *ПАО «МТС-Банк», пр. Андропова, 18, корп. 1, Москва, 115432, Российская Федерация*

✉ dolgunin-vn@yandex.ru

Аннотация: Проведено исследование эффектов взаимодействия и эффективности процесса сепарации частиц по размеру и плотности в быстрых гравитационных потоках, активированных продольными импульсами путем воздействия на частицы открытой поверхности потока шероховатой лентой конвейера. Установлено, что импульсное воздействие приводит к формированию в центральной части потока зоны с экстремально большими

значениями скорости сдвига и градиента доли пустот, обеспечивающими интенсивное протекание эффекта квазидиффузионной сепарации. В области, прилегающей к основанию потока, импульсное воздействие приводит к снижению доли пустот и повышению скорости сдвига, что способствует интенсификации сегрегации частиц по размеру. В области потока, прилегающей к поверхности импульсного воздействия, высокие значения доли пустот и температуры зернистой среды обеспечивают благоприятные условия для протекания квазидиффузионных эффектов перемешивания и сепарации. В результате импульсного воздействия эффективность сепарации повышается, если направление потоков квазидиффузионной сепарации и сегрегации совпадает (сепарация по плотности), и эффективность снижается при различном направлении названных потоков (сепарация по размеру). С повышением интенсивности импульсного воздействия зона интенсивного сдвига углубляется, и эффективность сепарации по плотности увеличивается, достигая максимального значения при углублении зоны на 0,5…0,55 толщины слоя. При дальнейшем повышении интенсивности импульсного воздействия эффективность сепарации снижается вследствие расширения области потока, в которой доминирует эффект квазидиффузионного перемешивания. Выводы по результатам эксперимента подтверждены методом математического моделирования динамики сепарации частиц по плотности в активированном гравитационном потоке.

Ключевые слова: зернистый материал; активированный гравитационный поток; продольные импульсы; сепарация по размеру и плотности; сегрегация; квазидиффузионная сепарация; скорость сдвига; объемная доля пустот.

Для цитирования: Ivanov OO, Dolgunin VN, Kudi KA. Mechanisms and kinetics of particle separation by size and density in an activated gravitational flow of granular material. *Journal of Advanced Materials and Technologies*. 2024;9(1):044-059. DOI: 10.17277/jamt.2024.01.pp.044-059

1. Introduction

In most practically important cases, flows of granular materials in technological processes and natural phenomena occur in the mode of rapid shear deformations [1–3]. Under conditions of rapid shear deformations, a specific mechanism for the formation of stresses appears, the magnitude of which is determined by the intensity of the exchange of impact momentum between particles of the material through the shear surface [2, 4, 5]. If shear deformations are caused by the action of gravity, then the corresponding flows are called fast gravity flows. Examples of this kind of flows can be the movement of materials on gravity slopes during transportation and the formation of embankments in tanks and bunkers, rotating pipes and drums, as well as natural processes of transforming the relief of the earth's surface (mudflows, rockfalls, underwater movements of rocks, expansion of dunes, etc.).

Fast gravity flows of granular materials, in general, are characterized by high heterogeneity of structural and kinematic parameters [6–8]. Thin-layer gravity flows on a rough slope are characterized by particularly high heterogeneity due to the relatively large contribution of boundary effects at the base and open surface of the flow [8, 9].

The intense interaction of particles under conditions of fast gravity flows is accompanied by the effects of their mixing and separation [6, 8, 9], the physical mechanisms and kinetics of which depend not only on the structural and kinematic characteristics of the flow, but also on the degree of heterogeneity of the latter. This is quite fully confirmed by the results of studies of the dynamics of the particle separation process according to a set of properties in a fast gravity flow presented in [6, 8, 10, 11]. As a result of the research, an equation for separation dynamics that describes the distribution of particles of the control component under the influence of convection, mixing and separation fluxes was obtained. The separation flux is expressed as a result of the conjugation of segregation fluxes caused by the relaxation of stresses concentrated on nonuniform particles in local flow conditions and quasi-diffusion separation initiated by the effects of spatial heterogeneity of the gravitational flow [8, 10, 11]. For the case of a two-dimensional flow, the dynamics of the concentration field $c(x, y, \tau)$ of control particles in a gravitational flow is determined as

$$\frac{\partial c(x,y,\tau)\rho_b}{\partial \tau} = -\frac{\partial uc\rho_b}{\partial x} + \frac{\partial}{\partial y}\left(\rho_b\left(D_{\text{dif}}\frac{\partial c}{\partial y} - D_{\text{m}}c\frac{\partial \ln s}{\partial y} - K\Delta Mc\right)\right), \quad (1)$$

where $\rho_b = \rho(1-\varepsilon(y))$ is a local value of the bulk density of the granular medium, kg·m^{-3}; D_{dif} and D_{m} are rate coefficients of quasi-diffusion mixing and quasi-diffusion separation, respectively, which are calculated analytically, m^2·s^{-1}; K is a segregation coefficient, (H·c)$^{-1}$; $u(y)$ is an averaged local velocity value in the shear direction, m·s^{-1}; ΔM is a driving force of segregation, calculated analytically excess moment of gravity, friction and impact impulses

acting on the test particle, N·m [8, 12]; $\varepsilon(y)$ is a volume fraction of voids, $m^3 \cdot m^{-3}$; x, y are coordinates in the direction of the slope and in the direction of the normal to the base of the flow, respectively; τ is time, s; $s(\varepsilon)$ is a local value of the average distance between particles, m.

It is important to note that in equation (1) the only kinetic parameter that requires experimental determination is the segregation coefficient K [8, 11, 12]. Research carried out in [12] made it possible to propose a method for experimentally determining the coefficient K as the relative velocity of the transverse movement of a control particle in a gravity flow of granular material per unit of excess moment of the forces acting on it. Moreover, it has been established that the segregation coefficient determined in this way exhibits the properties of a kinetic constant for a fairly wide range of changes in the properties of particles and flow parameters.

The complex of kinetic parameters (ΔM, D_{dif}, D_{m}), which determine the intensity of mixing and separation fluxes in equation (1), is expressed analytically as functions of particle properties, structural and kinematic parameters of the gravity flow based on the concept of a granular medium under conditions of the fast shear flow as "gas of solid particles" [1, 4, 13]. The quasi-diffusion separation coefficient for a binary mixture of cohesionless spherical particles having diameters d_i, masses m_i, restitution coefficients for collisions of uniform particles k_i is calculated by determining the ratio of the velocities of quasi-diffusion movements of nonuniform particles

$$D_{\text{m}} = \frac{\overline{m}(c)(\overline{V'})^2}{2F\overline{k}}\left(\frac{d_1^2 k_1}{m_1 \overline{d}^{-2}} - \frac{d_2^2 k_2}{m_2 \overline{d}^{-2}}\right), \qquad (2)$$

where F is an average value of the frequency of particle collisions in local conditions of their interaction calculated from the dissipation energy value [5, 8, 11] subject to the law of conservation of energy generated by gravity shear, s^{-1}; $\overline{V'} = F\,s$ is an averaged value of the local value of the velocity of particle fluctuations, $m \cdot s^{-1}$; $\overline{d}(c)$ is an average particle diameter, m; $\overline{m}(c)$ is an average particle mass, kg; $\overline{k}(c)$ is an average value of the restitution coefficient upon collision of mixture particles [8, 11].

The coefficient of quasi-diffusion mixing is calculated as a function of the averaged values of the local values of the distance between particles and the rate of their fluctuations [8, 11] by analogy with the molecular kinetic theory [14]

$$D_{\text{dif}} = \frac{1}{3}\overline{s}\overline{V'}. \qquad (3)$$

The analysis of dependencies (1) – (3) indicates a significant dependence of the kinetic parameters of the processes of mixing and separation of nonuniform particles in a fast gravity flow on its structural and kinematic parameters. In this case, determining role in the formation of distributions of nonuniform particles is played by the shear rate and the volume fraction of voids in the flow, which, according to the equation of state of the granular medium under conditions of fast gravity flow [8], are in mutual correlation. Dilatancy (volume fraction of voids) and shear kinetic stress in the flow increase in proportion to the square of the shear rate. As a consequence, the shear rate directly affects the magnitude of the driving force for segregation [12]. At the same time, it is obvious that the rate of particle fluctuations also increases in proportion to the shear rate, which, together with an increase in the volume fraction of voids, leads to a significant increase in the diffusion permeability of the medium intensifying the quasi-diffusion effects of mixing and separation.

The extremely high significance of the shear rate is also manifested in its influence on the kinetics of quasi-diffusion separation. The quasi-diffusion fluxes of particles of the mixture components intensify not only due to increasing shear rate, but also due to the special role of the shear rate in the formation of the conditions (driving force) of quasi-diffusion separation [8, 11]. A necessary condition for initiating a quasi-diffusion separation flux is the presence of a gradient in the volume fraction of voids. In a gravity flow, such a condition can be formed under the influence of two factors, one of which is heterogeneity of the shear rate, and the other is heterogeneity of lithostatic pressure.

The above analysis indicates the primary and ambiguous role of shear velocity in the formation of separation and mixing flows in a fast gravity flow of granular material. In this case, not only the magnitude of the shear rate is of great importance, but also the nature of its change in the flow. This is largely confirmed by the results of the analytical study presented in [15], on the basis of which we developed a comprehensive research method aimed at finding ways to intensify the effects of particle separation by size and density with active variation of the shear rate in the gravity flow.

2. Research Methods and Model Materials

To purposefully vary the shear rate in the fast gravity flow for increasing the efficiency of particle separation by size and density, it is necessary to determine not only the direction of exploratory research, but also the method of identifying structural and kinematic parameters under unusual flow conditions. In this regard, it is advisable to use the results and methodology of the study [15], carried out in the form of a virtual experiment. The experiments in experiment [15] were carried out with virtual variation of speed profiles. In this case, the void fraction profile, which is missing for a complete flow characteristic, was determined taking into account the correlation of flow parameters in accordance with the equation of state of the granular medium under the fast gravity flow. The equation of state describes the relationship between dilatancy $\bar{\varepsilon}$, lithostatic pressure p and temperature of the granular medium (kinetic energy of particles in their mutual movements) taking into account the physical and mechanical properties of the material [8, 15].

Since dilatancy is correlated with the volume fraction of voids, and the temperature of the granular medium is proportional to the square of the shear rate du_x/dy, it seems possible to write the equation of state in the following form [15]

$$\bar{\varepsilon} = \frac{\psi}{p}\left(\frac{du_x}{dy}\right)^2. \qquad (4)$$

Equation (4) includes the coefficient ψ, which, under certain assumptions [15], can be considered a constant, depending only on the physical and mechanical properties of particles.

As part of a virtual experiment, the influence of shear rate on the efficiency of separation in the gravity flow, which was assessed by the value of the variation coefficient of the test component distribution, was studied [15]. The experiment was carried out using the method of mathematical modeling of separation dynamics based on equation (1) under boundary conditions reflecting the absence of transfer of the test component at the base and open surface of the flow and its uniform initial distribution. To add certainty to the results, linear velocity profiles characterized by uniform values of shear velocity in the flow volume, varied in the experiment, were specified. A mixture of glass bead fractions was used as a model material: +3.25–3.5 mm (88 %) – base component; +3.6–3.75mm (12 %) – test component.

The results of the virtual experiment in the form of the dependence of the variation coefficient on the shear rate in the gravity flow are presented in Fig. 1.

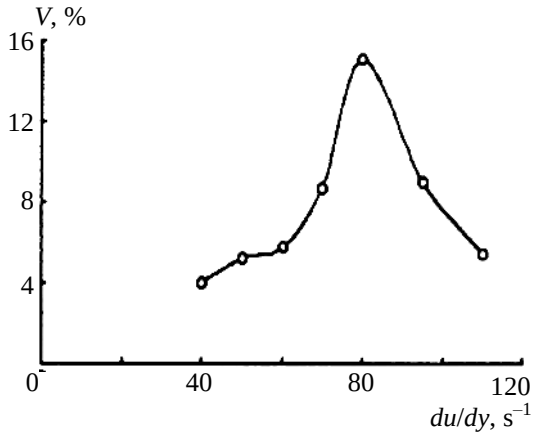

Fig. 1. Coefficient of variation in the composition of a bidisperse mixture of bead particles as a function of shear rate in the fast gravity flow [15]

Alternative options for mathematical modeling of the dynamics of the separation process with and without taking into account the effects of segregation and quasi-diffusion separation allowed us to draw a conclusion regarding the physical nature of the extreme value of heterogeneity in the shear rate range (80 ± 5) s^{-1}.

Modeling options indicate an increasing dominant role of the segregation effect in the ascending section of the dependence of the variation coefficient on the shear rate in the range of its moderate values, when there are sufficiently high values of the volume fraction of the solid phase in the flow. A further increase in the shear rate is accompanied by an increase in the volume fraction of voids in the flow, which creates conditions for the intense occurrence of quasi-diffusion effects and contributes to the transition of the dominant role from segregation to quasi-diffusion separation. Since in most of the gravity flow the effects of quasi-diffusion separation and particle size segregation have the opposite direction, a decrease in the variation coefficient is observed in this region. It is obvious that with a further increase in the shear rate, the nature of the dependence will not change, since the separation effects are increasingly suppressed by quasi-diffusion mixing, the effect of which increases with the increase in the rate of particle fluctuations and the volume fraction of voids in the flow (3).

The analysis of the kinetic laws of separation and the results of a virtual experiment clearly indicate the decisive and ambiguous role of shear rate in the manifestation of the interaction effects between nonuniform particles in the fast gravity flow [15]. The magnitude of the shear rate and the nature of its change along the height of the bed determine the distribution of the void volume fraction in the flow,

the intensity and conditions for coupling the effects of separation and mixing. This conclusion initiated an experimental and analytical study within the framework of this work, the main objective of which is to determine the conditions of the activated gravitational flow that ensures an increase in separation efficiency.

Variation in shear rate is proposed due to the transfer of additional momentum to particles through the open surface of the gravity flow. Additional momentum is provided by placing a conveyor belt with adjustable belt speed above the open surface of the flow. The belt has roughness equal in size to half the diameter of the particles and the lower branch of the tape is in direct contact with the particles on the bed surface. If the speed of the belt is higher than the velocity of the particles on the bed surface, then the particles receive an additional momentum in the direction of the slope, which, under the influence of the effect of pseudo-viscous friction [1], penetrates in the volume of the gravity flow. It is obvious that the magnitude of the momentum and the depth of its penetration into the bed will be determined by the relative speed of the belt and the longitudinal velocity of the particles on the open surface of the flow.

For a comprehensive analysis of the separation effects that are generated as a result of such a momentum action, it is necessary to have information about the corresponding hydrodynamic effects that determine the conditions for the interaction of nonuniform particles in the shear flow. If there is a complex of information in the form of velocity profiles and the volume fraction of voids, it becomes possible to mathematically model the dynamics of particle separation in alternative options that take into account or neglect certain effects of particle interaction in accordance with equation (1).

Mathematical modeling of the dynamics of the process is carried out by integrating equation (4) using a numerical method with the Crank-Nicholson difference scheme [16]. The initial and boundary conditions for the separation dynamics equation (4) are formulated for the case of the gravity flow on a rough chute in the following traditional form [8, 10–12]

$$D_{\text{dif}} \frac{\partial c}{\partial y} = cD_{\text{m}} \frac{\partial \ln s}{\partial y} = Kc\Delta M\big|_{y=0,h} = 0; \qquad (5)$$

$$c(0, x, y) = c_0, \quad c(t, 0, y) = c_0, \qquad (6)$$

where c_0 is an average concentration of the test component in the flow.

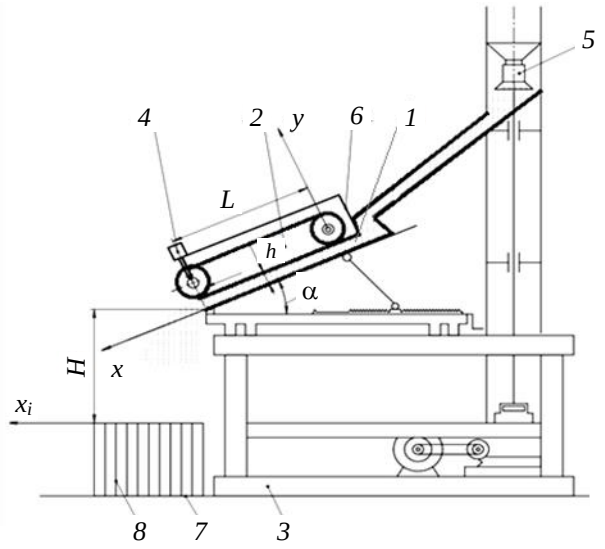

Fig. 2. Scheme of the experimental unit:
1 – rectangular channel with a rough bottom; *2* – conveyor with a rough belt; *3* – frame; *4* – conveyor drive; *5* – feeder dispenser; *6* – reflector; *7* – cuvette; *8* – cuvette cells

In this study, the profiles of the velocity and volume fraction of voids in the activated gravity flow were obtained using an experimental-analytical method [8, 11, 12], based on the analysis of the characteristics of the particle flow at the stage of their fall from a rough chute. These profiles were obtained using the experimental unit shown in Fig. 2.

To analyze the structural and kinematic characteristics of the flow, initial data is required, which includes an experimentally determined distribution function of the material along the horizontal coordinate x_1 with a known particle fall height *H*, layer thickness *h*, distribution formation time, slope angle α, true and bulk density of particles. The correlation of the particle coordinate at the chute threshold *y* with its horizontal coordinate of the material distribution x_1 is carried out using a system of equations [8, 11, 12]: material balance, the law of a freely falling body having an initial velocity, and the equation of state of a granular medium under rapid shear, which in a slightly transformed form is represented by dependence (4).

Unlike the traditional method, according to which a single boundary condition is specified corresponding to the condition of particle adhesion on the rough surface of the slope ($u = 0$ at $y = 0$) when the height of the roughness is equal to half the diameter of the particles, in the presented version of the method it is necessary to write the boundary condition on the upper boundary flow. This condition consists in the equality of the particle velocity at the upper boundary of the flow to the speed u_b of the

rough conveyor belt ($u = u_b$ at $y = h$, where h is the height of the bed).

In addition, in contrast to the traditional condition of zero lithostatic pressure on the open surface of the gravity flow, in the flow activated by additional longitudinal momentum, the particles of the bed, including its open surface, are under the influence of the so-called "dispersion" pressure [17]. Dispersion pressure is due to the presence of a normal component of external momentum action on the shear movement of particles near the open surface of the flow. In this case, the ratio of the longitudinal and normal components of the momentum action is determined by the dynamic coefficient of internal friction. In connection with the problems of identifying the named coefficient at the upper boundary of the flow, the work proposes to determine the dispersion pressure using the equation of state of the granular medium under conditions of the fast shear flow. In accordance with the adapted form of the equation of state (4), we have the following expression for pressure

$$p = \frac{\psi}{\varepsilon}\left(\frac{du_x}{dy}\right)^2 . \qquad (7)$$

If we assume that the value of the coefficient ψ of the state equation remains invariant under conditions of the activated gravity flow, then the dispersion pressure p_d can be represented by a component of the total pressure p. At the upper boundary of the flow, the total pressure will correspond to the dispersion pressure, and with deepening into the bed it will increase by the amount of lithostatic pressure. Thus, the dispersion pressure can be determined using (7) for known values of the shear rate initiated by the rough tape and the volume fraction of voids in the upper boundary zone of the flow. It seems possible to express the shear rate, to a first approximation, as the ratio of the difference in the velocities of the belt and particles on the surface of the flow in the absence of momentum action to the thickness of the bed.

Fractions (+3.25–3.5 and +4.0–4.25 mm) of glass beads (to prepare a binary mixture of particles differing in size) and fractions (+3.6–3.75 mm) of beads and silica gel uniform in size (for preparing a binary mixture of particles that differ in density) were used as model materials.

3. Results and Discussion

3.1. Experimental study of particle size separation in the activated gravity flow

At the first stage of the study, an experiment was carried out, the purpose of which was to assess the influence of momentum action through the open surface of the gravity flow on its structural and kinematic characteristics and the possibility of achieving separation effects with a change in shear rate, similar to those demonstrated as a result of the virtual experiment (Fig. 1).

In the study at this stage, a bidisperse mixture of bead particles was used with a test fine fraction (+3.25–3.5 mm) content of 5–8 % in its mixture with the fraction (+4.0–4.25 mm). The concentration of the mixture was varied in an arbitrary manner in the experiments, due to the high tendency of the mixture to segregate. Figures 3*a* and 3*b* show the profiles of velocity, volume fraction of voids and concentration distributions of test particles in gravity flows on

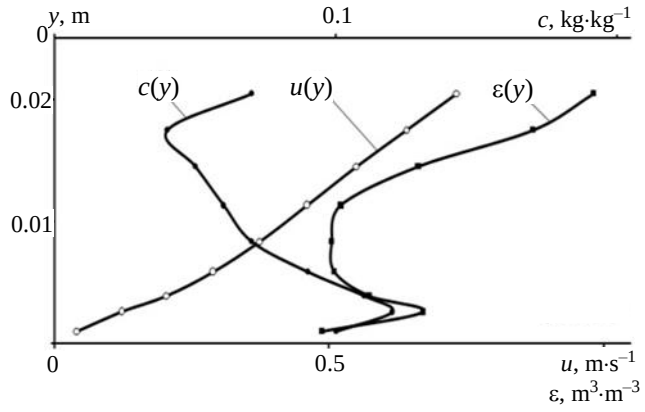

(*a*)

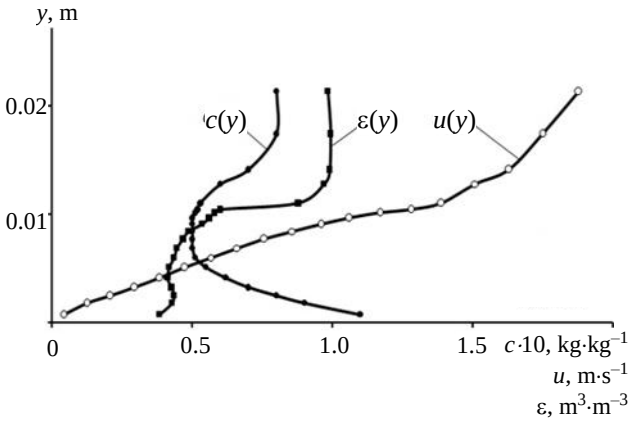

(*b*)

Fig. 3. Profiles of velocity $u(y)$, volume fraction of voids $\varepsilon(y)$ and concentration distribution of test small particles $c(y)$ in a binary mixture of bead fractions (+3.25–3.5 and +4.0–4.25 mm) in gravity flows:
a – in the absence of additional momentum action; *b* – in the activated gravity flow (belt speed 1.9 m·s^{-1})

a rough chute in experiments in the absence of momentum action and when an additional momentum is imparted to the flow. Additional momentum is provided by a rough conveyor belt moving at a speed of 1.9 $m \cdot s^{-1}$.

In order to reduce the random error of the experimental results and its statistical assessment, parallel experiments were performed to check the variation of the samples of measured values using the Student's t-test at a confidence probability level of 95 %. The relative value of the mean square error did not exceed 9 %.

A comparative analysis of the profiles in Fig. 3*a* and 3*b* allows us to detect the following effects of impulse action. Under the influence of the momentum pulse, not only does the shear rate systematically increase along the height of the bed, but also the formation of regions in the flow, the boundary between which runs through the surface with an extreme value of the shear rate. The flow region adjacent to the belt surface and receiving additional momentum from it finds itself in conditions of more intense chaotic movements of particles. As a result, in accordance with the equation of state of the granular medium under fast shear flow (4), the formed regions can be characterized as regions with low (at the base of the flow) and high (at the surface of the belt) temperatures of the granular medium. A similar conclusion should also be made when analyzing the characteristics of the structure of the named flow regions, based on the results of the study [18].

Since the temperature values of the granular medium in the named regions of the flow differ multiple times, then, in accordance with the same equation of state (4), it becomes the reason for an extremely sharp, almost hopping, increase in dilatancy during the transition from the lower region of the flow with a low temperature into the upper flow region having a high temperature. It is quite natural that a sharp increase in dilatancy is accompanied by the formation of a high gradient of the volume fraction of voids in the direction from the base to the surface of the gravity flow, as demonstrated by the corresponding profile $\varepsilon(y)$ in Fig. 3*b*. Due to the fact that the gradient of the volume fraction of voids directly determines the magnitude of the gradient of the average distance between particles, which, in accordance with equation (1), is the driving force of quasi-diffusion separation, the formation of a high gradient leads to a high local intensification of the named effect.

Based on the foregoing, it seems possible to assert that at the boundary of the contact of flow regions with low and high temperatures of the granular medium, a zone that functions similarly to a quasi-diffusion separator with a high degree of activity and localization in the volume of the bed is formed. Under the influence of quasi-diffusion separation in this zone, selective transfer of particles with a high fluctuation rate occurs in the direction of the temperature gradient of the granular medium, i.e. into the flow region with a high volume fraction of voids, where conditions for chaotic movements with a large free path are created for such particles. Under the influence of this effect, particles with a low fluctuation rate move in the opposite direction, i.e. into the flow region with a high concentration of solids.

This conclusion is confirmed by a comparative analysis of the distribution profiles of the concentration of test particles in flows without additional momentum action (Fig. 3*a*) and with momentum imparted by a rough belt (Fig. 3*b*). In the absence of the pulse impact (Fig. 3*a*), the concentration of test small particles systematically, with the exception of boundary values, increases towards the base in almost the entire volume of the flow. This indicates the dominance of the segregation effect in the flow in accordance with the mechanism of shear flow separation [12], formally similar to the mechanisms of percolation and kinetic sieving, on which most developed models of the kinetics of the separation process are based [19–23]. As a result of the momentum effect, the distribution of the concentration of test particles undergoes a significant and fundamental change, indicating a significant contribution of the quasi-diffusion separation effect to the process of distribution of nonuniform particles [8, 10, 11]. First of all, this conclusion is confirmed by an increase in the concentration of test fine particles in the direction from the base of the slope in the flow region covering the zone of intense shear deformation and the region located above it with a high temperature of the granular medium (profile $c(y)$ in Fig. 3*b*). An increase in the concentration of small particles in the direction opposite to the lithostatic pressure gradient, reaching values exceeding their average concentration in the flow, contradicts the segregation effect. At the same time, the coincidence in the indicated region of the directions of the concentration gradients of small particles and the volume fraction of voids makes it possible to explain the fundamental change in the concentration profile under momentum action by the intensification of the effect of quasi-diffusion separation (1).

Thus, based on the analysis of the structural and kinematic parameters of the gravity flow of the

granular medium under conditions of additional momentum action, the following conclusion can be drawn. In contrast to the conditions of the virtual experiment [15], which made it possible to study with sufficiently high certainty the effect of shear rate on separation efficiency (Fig. 1), in this case there are nonlinear velocity profiles, which are characterized by non-uniform values of the shear rate in the flow volume.

The presence of regions with fundamentally different flow conditions in flows between two parallel inclined rough planes that have a relative speed of movement fundamentally distinguishes them from Couette flows [24–26]. It is obvious that the formation of regions in the flow with fundamentally different flow conditions is a consequence of the coupling of momentums generated by gravity and additional activating influence. In this we can note a certain analogy with the evolution of the stress-strain state in the processes of formation of structures of composite mixtures [27–30].

Taking into account the discovered features of the structure of the activated gravity flow, which occur as a result of the formation in its central part of a brightly localized zone with intense shear deformation and a pronounced effect of quasi-diffusion separation, within the framework of the work, it is proposed to use the separation coefficient to reflect the dependence of the separation efficiency on the shear rate. The value of the separation coefficient is determined either by the degree of depletion (depletion coefficient) of particles with a high fluctuation rate from the flow region with a low temperature of the granular medium, or by the degree of enrichment (enrichment coefficient K_e) of these particles in the flow region with a high temperature of the granular medium. It is obvious that the values of the separation coefficient K_s in alternative versions of its definition are the same, i.e. the coefficients of depletion K_d and enrichment K_e are equal to each other: $K_s = K_d = K_e$. These coefficients are determined as follows:

$$K_s = K_d = \frac{c_0 - c_1}{c_0}\left(\frac{G_1}{G_0}\right); \qquad (8a)$$

$$K_s = K_e = \frac{c_2 - c_0}{c_0}\left(\frac{G_2}{G_0}\right), \qquad (8b)$$

where c_0, c_1, c_2 is an average concentration of test particles in the flow as a whole, in the flow region with a low temperature of the granular medium located below the zone of intense shear, and in the region of the flow with a high temperature of the granular medium located above the zone of intense shear, respectively, kg·kg^{-1}; G_0, G_1, G_2 are mass flow rates of material in the gravity flow and in its regions with low and high temperatures of the granular medium, respectively, kg·s^{-1}; $G_0 = G_1 + G_2$.

The findings of the impact of the additional momentum intensity in the gravity flow on the efficiency of particle size separation in it are presented in Fig. 4 in the form of a dependence of the separation coefficient on the shear rate. Taking into account the no-slip condition at the upper and lower boundaries of the flow, the average value of the shear rate in the flow was conventionally determined as the ratio of the belt speed to the bed height. The experimental results shown in Fig. 4 were obtained at belt speeds from 1 to 2 m·s^{-1}.

In order to analyze the effect of additional momentum, the findings on the separation coefficient in the activated gravity flow are presented in comparison with the separation coefficient in the gravity flow without external influence. The average shear rate in the flow without additional momentum action, which is defined as the ratio of the particle velocity on the open flow surface to the bed height, was 36 s^{-1}. In this regard, the experimental value of the coefficient K_s, corresponding to the minimum value of the shear rate in Fig. 3, was obtained for the gravity flow in the absence of additional momentum action. In this case, the boundary between the regions of separated fractions in the flow is established by the average concentration of test particles. In one of the regions, local concentration values are systematically higher (enrichment region), and in the other – lower (depletion region) compared to the average concentration.

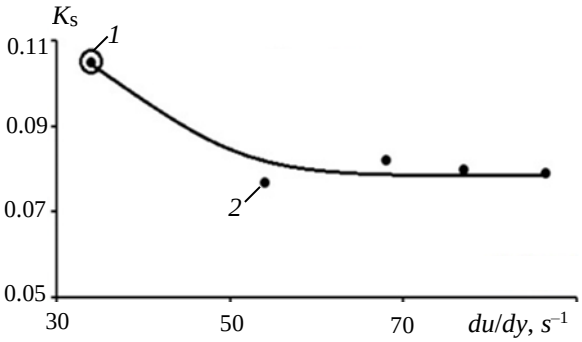

Fig. 4. Dynamics of changes in the separation coefficient of a binary mixture of bead fractions (+3.25–3.5 and +4.0–4.25 mm) depending on the shear rate in gravity flows:
1 – in the absence of additional momentum action;
2 – in activated gravity flows

The resulting dependence $K_s(du/dy)$ demonstrates a decrease in the separation coefficient with increasing intensity of the additional momentum action. This effect is quite fully explained by the results of a previous analysis of the velocity profiles, volume fraction of voids and concentration distributions of test particles shown in Figs. 3*a* and 3*b*. It should be noted that with an increase in the additional momentum effect on the gravity flow, the quasi-diffusion effects of mixing and separation intensify due to the formation of a region with a high temperature of the granular medium in the upper part of the flow. Moreover, for particles differing in size (Fig. 3*b*), the quasi-diffusion separation flux in this region has a direction opposite to the segregation flux, which dominates the separation process in the fast gravity flow without activation (Fig. 3*a*). The counter direction of segregation and quasi-diffusion separation fluxes with increasing intensity of the latter is accompanied by the loss of the dominant role of segregation and a decrease in separation efficiency. In addition, a decrease in separation efficiency is facilitated by an increase in the intensity of the quasi-diffusion mixing flow (3) with an increase in the distance between particles and the rate of particle fluctuations due to an increase in the shear rate and the volume fraction of voids under the influence of additional momentum.

3.2. Separation of particles by density in the activated gravity flow

The analysis of physical mechanisms of transformation of structural-kinematic parameters set out in Section 3.1 and, accordingly, the conditions for generating separation effects in the fast gravity flow under the influence of additional longitudinal momentum allows us to formulate a hypothesis regarding the intensification of the process. According to research, an increase in separation efficiency with this method of flow activation can be achieved in cases where either the direction of the segregation flows and quasi-diffusion separation coincide, or the segregation flow is negligibly small. It is obvious that this type of coupling options for separation flows is provided when the particles differ in density, roughness and elasticity [8, 11]. Under the influence of the quasi-diffusion separation effect, less dense, smooth and more elastic particles will migrate in the direction of the void volume fraction gradient (into the flow region with a high temperature of the granular medium), which coincides with the direction of segregation of such particles.

In order to test this hypothesis, an experimental and analytical study of the dynamics of particle separation by density in the activated gravity flow was carried out as part of the work. A mixture of uniform in size fractions (+3.6–3.75 mm) of beads and silica gel (test component) with a density of 2500 and 700 $kg \cdot m^{-3}$, respectively, was used as a model material. The experimental research technique was fully consistent with that used previously when studying the dynamics of particle size separation. The study of the influence of an additional momentum on the efficiency of separation in the gravity flow of particles of different densities was carried out in the range of shear rates, which was controlled by varying the speed of the rough conveyor belt adjacent to the open surface of the layer from 1 to 2 $m \cdot s^{-1}$.

The results of the study in the form of profiles of velocity, volume fraction of voids and concentration of control particles (silica gel) in gravity flows without additional momentum action and in the case of its activation (belt speed 1.5 $m \cdot s^{-1}$) are shown in Figs. 5*a* and 5*b*, respectively.

A comparative analysis of the profiles indicates fundamental changes in the structural and kinematic characteristics of the gravity flow under conditions of additional momentum action. Such changes were noted earlier in the gravity flow of particles differing in size (Fig. 3). First of all, such changes include the formation in the central part of the flow in a zone with an extremely high intensity of shear deformation, which is part of the above flow region with high temperature values of the granular medium and the volume fraction of voids. Below this zone, a flow region with a low temperature of the granular medium is formed.

Particularly noteworthy is the extremely low value of the volume fraction of voids in the region of the activated gravity flow located below the zone with extremely high shear rates. At first glance, this result seems paradoxical, since the decrease in the volume fraction of voids under the influence of additional momentum to values close to the volume fraction of voids in the stationary bulk bed occurs under conditions of increasing shear rate in the specified flow region. The physical mechanism of the observed effect of contraction of the lower part of the flow under the influence of an additional momentum can be explained by the presence of fundamentally different boundary conditions at the base and upper boundary of the flow.

Under the influence of the pseudo-viscous effect in the fast shear flow of the granular medium, the energy of an additional longitudinal momentum distributed along the upper boundary of the flow penetrates deep into the bed intensifying the mutual

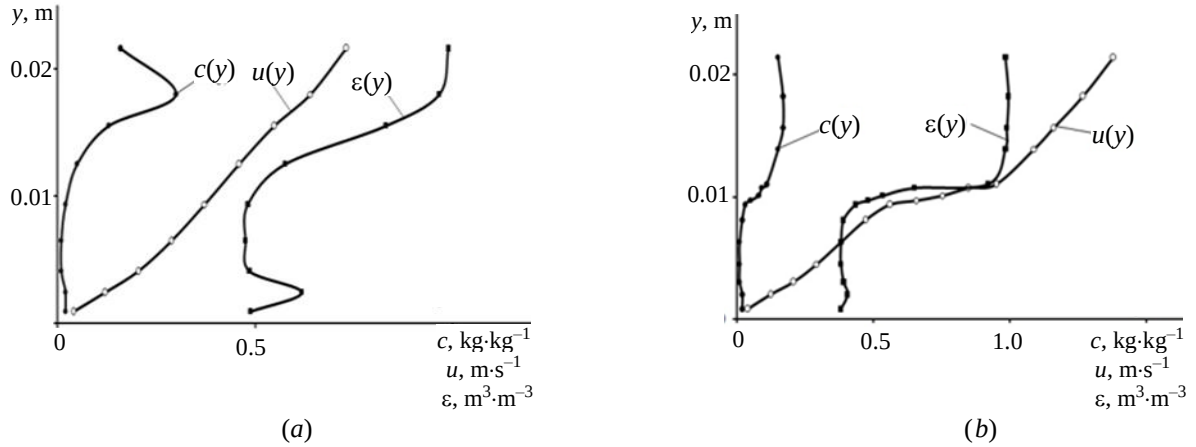

Fig. 5. Profiles of velocity $u(y)$, volume fraction of voids $\varepsilon(y)$ and distribution of test particles concentration $c(y)$ in a mixture of monodisperse particles (+3.6–3.75 mm) of beads and silica gel in gravity flows:
a – in the absence of additional momentum influence; *b* – when activated by longitudinal momentum (belt speed 1.5 m·s^{-1})

movements of particles mainly in the flow region located above the zone of intense shear deformation. In this case, relatively high values of the temperature of the granular medium (the kinetic energy of particles in their mutual movements) are achieved in the named flow region. Due to the condition of sticking at the base of the bed and the dissipation of energy of the additional momentum as it penetrates deep into the layer (according to the effects of pseudo-viscous friction, elasticity and friction), in the flow region located below the zone of intense shear, the temperature of the granular medium turns out to be significantly lower than in the upper part of the flow. The higher temperature of the granular medium in the upper part of the flow leads to effect of "dispersion pressure" [17] causing contraction of the lower part of the flow.

In this regard, it seems possible to assert that the formation of a zone with intense shear deformation is accompanied by the formation of flow regions with an extremely large difference in the volume fraction of voids. Thus, the zone of intense shear deformation is located at the boundary between flow regions characterized by a large difference in the average distance between particles. As a consequence, favorable conditions for the manifestation of the effect of quasi-diffusion separation under the influence of a large gradient of the average distance between particles, i.e. the driving force of this effect, are formed in this zone [8, 11].

The findings in the form of velocity profiles, volume fraction of voids and concentration of test particles (silica gel) in the gravity flow are shown in Figures 6–8 for different magnitudes of momentum action (conveyor belt speed). For the purpose of comparative assessment of the effect of the gravity flow activation, the figures show profiles obtained in the absence of additional impulse action, when the belt speed is zero.

The analysis of the evolution of velocity profiles shows that with increasing momentum action, shear rates increase throughout the entire volume of the flow, but the most significant changes in the rate of deformation of the granular medium are observed in the flow region with a high temperature of the granular medium and, especially, in the vicinity of the zone with extreme values of the shear rate. With increasing momentum action, this zone deepens and expands with an increase in the flow region with a high temperature of the granular medium.

In all cases, even at small values of the additional momentum, fundamental changes in the velocity profiles and the volume fraction of voids are observed. One of the main features of the ongoing profile changes is that together with the formation of an intense shear zone in the flow, there is a sharp decrease in the volume fraction of voids (an increase in the fraction of the solid phase) in the flow area adjacent to its base. This is evidenced by a comparison of profiles 1 and 2 in Figs. 6 and 7. When increasing intensity of the momentum action, the volume fraction of voids increasingly approaches its extreme minimum value, corresponding to the porosity of the repose state of bulk material.

It is important to note that an increase in the volume fraction of the solid phase in the flow region adjacent to its base occurs under the action of a longitudinal momentum with increasing shear rate. A change in the structural and kinematic characteristics in the indicated direction contributes to an increase in stress concentrations on non-uniform particles, which, according to the kinetic laws of segregation [2, 8, 12], directly increases the driving force of the mentioned separation effect. This conclusion is especially clearly confirmed by the results of a study

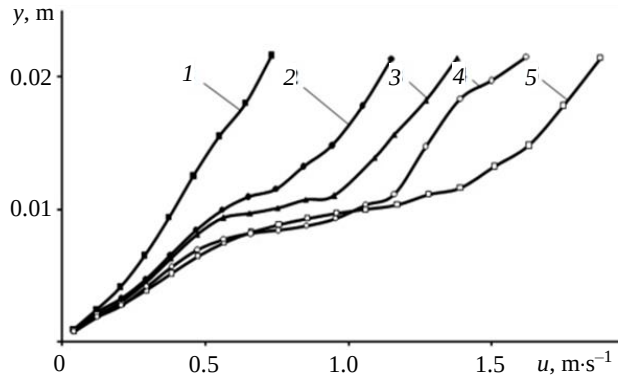

Fig. 6. Velocity profiles in gravity flows of a mixture of monodisperse particles (+3.6–3.75 mm) of beads and silica gel for different values of longitudinal momentum generated at conveyor belt speeds, m·s^{-1}: *1* – 0.0; *2* – 1.2; *3* – 1.5; *4* – 1.7; *5* – 1.9

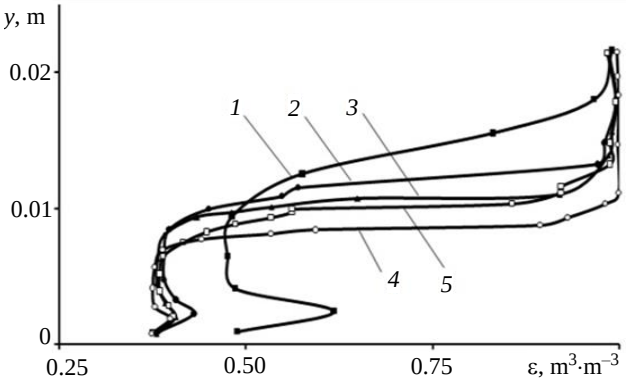

Fig. 7. Profiles of the volume fraction of voids in gravity flows of a mixture of monodisperse particles (+3.6–3.75 mm) of beads and silica gel for different values of longitudinal momentum generated at conveyor belt speeds, m·s^{-1}: *1* – 0.0; *2* – 1.2; *3* – 1.5; *4* – 1.7; *5* – 1.9

of particle size separation in gravity flows in the absence and presence of additional momentum action, presented in Figs. 3*a* and 3*b*, respectively. A comparison of the concentration profiles in Figs. 3*a* and 3*b* shows that in the flow region adjacent to its base, the impact of an additional momentum is accompanied by a significant increase in the concentration gradient of test particles, which indicates intensified segregation.

At the same time, conditions are formed for the intensive occurrence of quasi-diffusion separation in the remaining flow region, in which the momentum action leads to an increase in quasi-diffusion permeability and the gradient of the volume fraction of voids. Thus, it seems possible to highlight two aspects of increasing the efficiency of separation in the gravity flow under the influence of additional longitudinal momentum action. Firstly, the momentum effect helps to intensify the effect of quasi-diffusion separation in the flow region adjacent to the surface of the direct momentum effect. Secondly, the momentum effect contributes to the intensification of segregation in the flow area adjacent to its base.

If, in accordance with the physical and mechanical properties of the mixture particles, the direction of the effects of segregation and quasi-diffusion separation for the test particles coincides, then as a result of the additional momentum action, the separation efficiency increases. For example, for a mixture of monodisperse particles of different densities, segregation of test particles with low density occurs in the direction opposite to the lithostatic pressure gradient, i.e. towards the upper boundary of the flow. This direction coincides with the gradient of the volume fraction of voids in the upper part of the flow, in the direction and under the influence of which quasi-diffusion separation of less dense particles occurs.

Thus, the findings made it possible to obtain the information necessary to theoretically substantiate the feasibility of applying longitudinal momentum to the fast gravity flow of the granular material to increase separation efficiency. The feasibility of using longitudinal momentum should be justified taking into account the conjugation of the direction of segregation and quasi-diffusion separation fluxes and the possibility of intensifying the corresponding effects in the flow volume.

Since the concentrations of test particles were obtained by the direct weight method, the geometric similarity of the distribution profiles of the concentration (Fig. 8) and the volume fraction of voids (Fig. 7) is an indirect, but quite convincing confirmation of the reliability of changes in the structural and kinematic characteristics of the gravity flow that occur under the influence of additional longitudinal momentum. This is explained by the fact that for particles differing in density, the dominant separation effect is quasi-diffusion separation [8, 10, 11], the driving force of which is the gradient of the average distance between particles, proportional to the gradient of the volume fraction of voids. In this regard, particles with a high fluctuation rate are distributed in the flow revealing gradients in the concentration distribution similar to gradients of the volume fraction of voids.

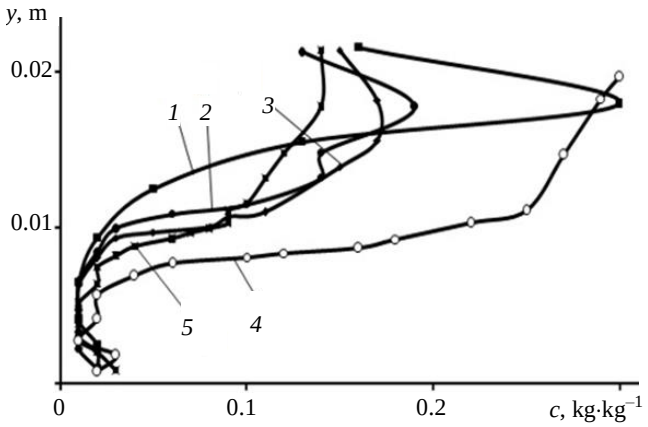

Fig. 8. Concentration profiles of test particles in gravity flows of a mixture of monodisperse particles (+3.6–3.75 mm) of beads and silica gel for different values of longitudinal momentum generated at conveyor belt speeds, m·s^{-1}: *1* – 0.0; *2* – 1.2; *3* – 1.5; *4* – 1.7; *5* – 1.9

In the profiles (Fig. 8) for flows with momentum action, a zone of high concentration gradient of test particles is clearly visible, the dislocation of which in the flow volume completely coincides with the location of zones of intense shear deformation (Fig. 6) and a high gradient of the volume fraction of voids (Fig. 7). With an increase in the intensity of the momentum effect, the zone of extreme values of velocity gradients, volume fraction of voids and concentration of the test component deepens without reducing the magnitude of the gradients (curves *2–4* in Figs. 6–8). However, as the zone approaches the base of the bed at a distance equal to approximately two particle diameters and a further increase in the intensity of the momentum action, signs of impending destruction of the zone are observed (curves *5* in Figs. 6-8). First of all, the destruction of the zone is evidenced by a sharp decrease in the velocity gradients, the volume fraction of voids and the concentration of the test component and a shift in the extreme values of the gradients towards the upper boundary of the flow.

The findings on the impact of the intensity of momentum action on the efficiency of particle separation by density in the gravity flow are presented in Fig. 9 in the form of a dependence of the separation coefficient (8) on the shear rate. The technique for determining the average shear rate and separation coefficient was similar to the technique used in the case of differences in particle size. For a comparative assessment of the effect of momentum action in the separation process, the dependence $K_s(du/dy)$ was constructed taking into account the separation coefficient and the average value of the shear rate in the gravity flow without momentum action. These indicators are determined in full accordance with the procedure used to find them in the gravity flow of particles of various sizes (Fig. 4).

The obtained dependence $K_s(du/dy)$ for particles differing in density (Fig. 9) is fundamentally different from the similar dependence for particles of different sizes (Fig. 4). In the studied range of pulse impact intensity and corresponding shear rates, the values of the separation coefficient exceed the value of the coefficient in the gravity flow without momentum impact. The $K_s(du/dy)$ dependence reveals an extreme value of the separation coefficient corresponding to an average shear rate of 65–70 s^{-1}. If the physical mechanism of the increase in the separation coefficient with an increase in the intensity of the momentum effect was previously explained by the increase in the driving force of the effects of quasi-diffusion separation and segregation, then the mechanism for the decrease in the coefficient after reaching a certain extreme value requires additional analysis and explanation.

A hypothetical explanation for the decrease in the separation coefficient with increasing momentum action may be an increase in the volume of flow with a high temperature of the granular medium associated with a deepening of the zone of intense shear deformation. As the zone deepens, the above-located rarefied flow region expands, in which, due to small values of the gradient of the volume fraction of voids, the role of quasi-diffusion mixing increases. Intense quasi-diffusion mixing of particles in a rarefied region of the flow is facilitated by the high diffusion permeability of the medium, proportional to the average distance between particles and the velocity of their chaotic movements [31].

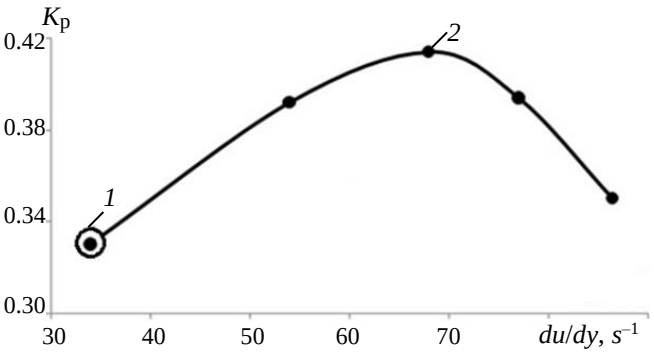

Fig. 9. Dynamics of changes in the separation coefficient of a mixture of monodisperse particles (+3.6–3.75 mm) of beads and silica gel depending on the shear rate in gravity flows: *1* – in the absence of additional momentum action; *2* – in activated gravity flows

It is important to note the similar nature of the dependences of the separation efficiency indicators on the shear rate presented in Figs. 1 and 9. A fairly high degree of analogy of the dependences occurs despite the fundamental difference in the objects to which they relate. In a virtual flow (Fig. 1), the shear rate is uniform throughout the volume of the layer and the particles differ in size, but in a real activated flow (Fig. 9) there is a high heterogeneity of the shear rate and separation of particles by density. In the first case, particle separation occurs predominantly under the influence of the segregation effect, and in the second case, quasi-diffusion separation plays a decisive role. At the same time, the dependences of the efficiency indicators reveal an extreme value of efficiency at close average values of the shear rate (80 and 70 s^{-1}). Taking into account that the physical nature of the decrease in separation efficiency in the cases under consideration is obviously general and is associated with the suppression of separation effects by quasi-diffusion mixing, we can assume the existence of a threshold average value of the shear rate in the gravity flow (70–80 s^{-1}). As the specified shear rate and the corresponding dilatancy of the medium are exceeded, the rate of particle fluctuations and their free path increase so much that quasi-diffusion mixing of particles begins to suppress separation effects.

Thus, the findings made it possible to obtain the information necessary to theoretically substantiate the feasibility of applying longitudinal momentum to the fast gravity flow of the granular material to increase separation efficiency. The feasibility of using longitudinal momentum should be justified taking into account the option of combining the direction of segregation and quasi-diffusion separation fluxes with a certain combination of properties of nonuniform particles.

In order to analytically confirm the reliability of the conclusions based on the results of the experimental study, mathematical modeling of the dynamics of the separation process in the activated gravity flow (belt speed 1.5 $m \cdot s^{-1}$) of beads and silica gel granules of uniform size was carried out. The modeling method and the conditions for its implementation are described in Section 2. Figure 10 shows the concentration distribution profiles of low-density particles in the activated gravity flow. In order to provide conditions for a comparative analysis of separation effects and identify areas of their dominance, modeling was carried out for options with and without taking into account the effect of quasi-diffusion separation. To assess the adequacy of the modeling results, the latter are presented in comparison with the experimentally obtained concentration distribution profile. The velocity and volume fraction of voids profiles presented in Figs. 5, 6 were used as initial data for modeling. The adequacy of the modeling results was established by comparing the variances of adequacy and reproducibility using Fisher's *F* test at a significance level of 5 %.

The analysis of concentration profiles shows that the presence of a zone with a high concentration gradient in the central part of the flow, characteristic of the experimental profile, is detected only when modeling taking into account the flow of quasi-diffusion separation ($D_m \neq 0$).

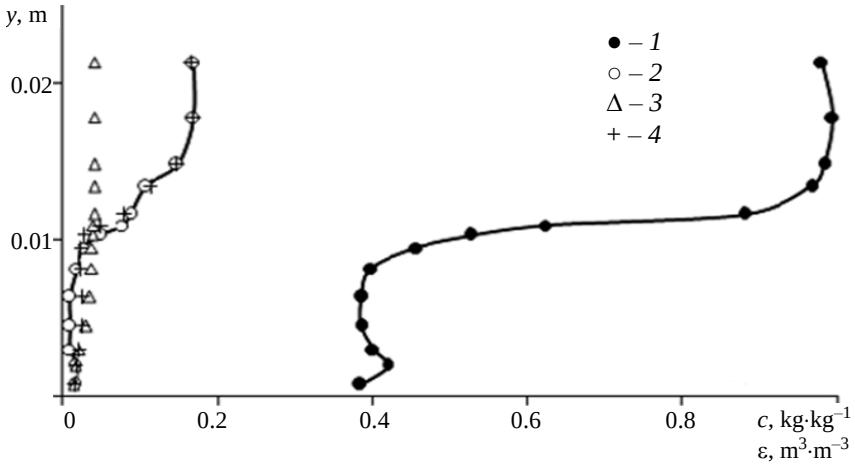

Fig. 10. Profiles of the volume fraction of voids (1) and the concentration of silica gel granules (2) – (4) in the activated (belt speed 1.5 $m \cdot s^{-1}$) fast gravity flow in a mixture with beads:
1, *2* – experimental results; *3* – simulation results based on (1) at $D_m = 0$; $K \neq 0$;
4 – simulation results based on (1) at $D_m \neq 0$, $K \neq 0$

The coordinates of the location of the zone in the bed completely coincide with the coordinates of extremely large gradients of the volume fraction of voids in the flow, which are a condition for ensuring high values of the driving force of quasi-diffusion separation. The combination of the listed features of the profiles presented in Figure 10 indicates not only the dominant role of the effect of quasi-diffusion separation, but also indicates the determining importance of the factor in the formation of a zone of intense shear deformation in the distribution of nonuniform particles.

4. Conclusion

An experimental and analytical study was carried out on the effectiveness of particle separation by size and density when activating shear deformations in fast gravity flows of granular materials. Activation is carried out by imparting to the particles on the open surface a flow of additional momentum in the direction of the slope using a rough conveyor belt. It was established that under the influence of momentum in the central part of the flow a zone with extremely high values of shear rate, gradient of the void fraction and, as a consequence, the intensity of the quasi-diffusion separation effect is formed. Below the zone there is a flow region in which the momentum action is accompanied by a decrease in the proportion of voids and an increase in the shear rate with a corresponding intensification of particle size segregation. In the flow region located above the zone of intense shear, the momentum effect leads to an increase in the proportion of voids and the temperature of the granular medium and, as a consequence, to the intensification of the quasi-diffusion effects of mixing and separation.

Momentum action increases separation efficiency if the direction of quasi-diffusion separation and segregation fluxes for the test component coincides (for example, density separation). Momentum action reduces the efficiency of particle separation by size, for which the direction of the said fluxes is opposite. With increasing shear rate, the zone of intense shear deepens, and the efficiency of density separation increases reaching its maximum value when the zone deepens by 0.5–0.55 of the layer thickness. With a further increase in the intensity of the momentum action, the separation efficiency decreases due to the expansion of the flow region in which the effect of quasi-diffusion mixing dominates. The results of mathematical modeling confirm the decisive role of the quasi-diffusion separation effect in the zone of intense shear of the activated gravity flow in the process of particle separation by density.

5. Funding

The study was supported by the RFBR grant No. 09-08-97521.

6. Conflict of interests

The authors declare no conflict of interest.

References

1. Forterre Y, Pouliquen O. Flows of dense granular media. *Annual Review of Fluid Mechanics.* 2008;40:1-24. DOI:10.1146/annurev.fluid.40.111406.102142

2. Savage SB. Granular flows down rough inclines – Review and extension. In: Jenkins JT, Satake M. (Eds.) *Studies in Applied Mechanics.* 1983;7:261-282. DOI:10.1016/B978-0-444-42192-0.50028-1

3. Goldhirsch I. Rapid granular flows. *Annual Review of Fluid Mechanics.* 2003;35:267-293. DOI:10.1146/annurev.fluid.35.101101.161114

4. Brennen CE. *Fundamentals of Multiphase Flows*. Cambridge: Cambridge University Press; 2005. 410 p. DOI:10.1017/CBO9780511807169

5. Shen HH, Ackermann NL. Constitutive relationships for fluid-solid mixture. *Journal of the Engineering Mechanics Division.* 1982;108:748-763. DOI:10.1061/jmcea3.0002868

6. Hill KM, Fan Y. Granular temperature and segregation in dense sheared particulate mixtures. *KONA Powder and Particle Journal.* 2016;33:150-168. DOI:10.14356/kona.2016022

7. Domnik B, Pudasaini SP, Katzenbach R, Miller SA. Coupling of full two-dimensional and depth-averaged models for granular flows. *Journal of Non-Newtonian Fluid Mechanics.* 2013;201:56-68. DOI:10.1016/j.jnnfm. 2013.07.005

8. Dolgunin VN, Kudi AN, Tuev MA. Mechanisms and kinetics of gravity separation of granular materials. *Physics Uspekhi.* 2020;63(6):545-561. DOI:10.3367/ UFNe.2020.01.038729

9. Gray JMNT, Thornton AR. A theory for particle size segregation in shallow granular free-surface flows. *Proceedings of the Royal Society A: Mathematical, Physical and Engineering Sciences.* 2005;461(2057):1447-1473. DOI:10.1098/rspa.2004.1420

10. Dolgunin VN, Kudy AN, Ukolov AA. Development of the model of segregation of particles

undergoing granular flow down on inclined chute. *Powder Technology*. 1998;96(3):211-218. DOI:10.1016/S0032-5910(97)03376-7

11. Dolgunin VN, Ivanov OO, Ukolov AA. Segregation kinetics of particles with different roughness and elasticity under a rapid gravity flow of a granular medium. *Theoretical Foundations of Chemical Engineering.* 2009;43:187-195. DOI:10.1134/S0040579509020092

12. Dolgunin VN, Ukolov AA, Ivanov OO. Segregation kinetics in the rapid gravity flow of granular materials. *Theoretical Foundations of Chemical Engineering.* 2006;40(4):393-404. DOI:10.1134/S0040579506040099

13. Nagel SR. Experimental soft-matter science. *Reviews of Modern Physics*. 2017;89(2):025002. DOI:10.1103/RevModPhys.89.025002

14. Ferziger JH, Kaper HG, Gross EP. Mathematical theory of transport processes in gases. *American Journal of Physics.* 1973;41(4):601-603. DOI:10.1119/1.1987312

15. Ivanov OO, Dolgunin VN, Tarakanov AG, Zhilo AA, Pronin VA. Evolution of separation effects under variable conditions of gravity flows of granular materials. *Journal of Advanced Materials and Technologies*. 2022;7(3):181-191. DOI:10.17277/jamt.2022.03.pp.181-191

16. Marchuk GI, *Methods of numerical mathematics. Applications of mathematics*. New York: Springer-Verlag Publ.; 1975. 510 p.

17. Bagnold RA. Experiments on a gravity free dispersion of large solid spheres in a newtonian fluid under shear. *Proceedings of the Royal Society of London. Series A. Mathematical and Physical Sciences.* 1954;225(1160):49-63. DOI:10.1098/rspa.1954.0186

18. Campbell CS. Granular material flows – an overview. *Powder Technology*. 2006;162(3):208-229. DOI:10.1016/j.powtec.2005.12.008

19. Xiao H, Deng Z, Ottino JM, Umbanhowar PB, Lueptow RM. Modeling stratified segregation in periodically driven granular heap flow. *Chemical Engineering Science*. 2023;278:118870. DOI: 10.1016/j.ces.2023.118870

20. Duan Y, Peckham J, Umbanhowar PB, Ottino JM, Lueptow RM. Designing minimally segregating granular mixtures for gravity-driven surface flows. *AIChE Journal*. 2023;69(4):18032. DOI:10.1002/aic.18032

21. Duan Y, Umbanhowar P, Ottino J, Lueptow R. Modelling segregation of bidisperse granular mixtures varying simultaneously in size and density for free surface flows. *Journal of Fluid Mechanics*. 2021;918. DOI:10.1017/jfm.2021.342

22. Umbanhowar PB, Lueptow RM, Ottino JM. Modeling segregation in granular flows. *Annual Review of Chemical and Biomolecular Engineering.* 2019;10:129-153. DOI:10.1146/annurev-chembioeng-060718-030122

23. Gray JMNT. Particle segregation in dense granular flows. *Annual review of fluid mechanics*. 2018; 50:407-433. DOI:10.1146/annurev-fluid-122316-045201

24. Stephens DJ, Bridgwater J. The mixing and segregation cohesionless particulate materials: Part I. Failure zone formation. *Powder Technology*. 1978;21:17-28. DOI:10.1016/0032-5910(78)80104-1

25. Conway SL, Liu X, Glasser BJ. Instability-induced clustering and segregation in high-shear Couette flows of model granular materials. *Chemical Engineering Science*. 2006;61(19):6404-6423. DOI:10.1016/j.ces. 2006.05.049

26. Varsakelis C, Papalexandris MV. Stability of wall bounded, shear flows of dense granular materials: the role of the Couette gap, the wall velocity and the initial concentration. *Journal of Fluid Mechanics*. 2016;791:384-413. DOI:10.1017/jfm.2016.65

27. Nazarov VI, Makarenkov DA, Retivov VM, Popov AP, et al. Features of the pyrolysis process of waste batteries using carbon black as an additive in the construction industry. *Construction Materials and Products.* 2023;6(6):4. DOI:10.58224/2618-7183-2023-6-6-4

28. Klyuev AV, Kashapov NF, Klyuev SV, Zolatareva SV, et al. Experimental studies of the processes of structure formation of composite mixtures with technogenic mechanoactivated silica component. *Stroitel'Nye Materialy i Izdeliya = Construction Materials and Products*. 2023;6(2):5-18. DOI:10.58224/2618-7183-2023-6-2-5-18 (In Russ.)

29. Klyuev AV, Kashapov NF, Klyuev SV, Lesovik RV, et al. Development of alkali-activated binders based on technogenic fibrous materials. *Stroitel'Nye Materialy i Izdeliya=Construction Materials and Products*. 2023;6(1):60-73. DOI:10.58224/2618-7183-2023-6-1-60-73 (In Russ.)

30. Novoselov OG, Sabitov LS, Sibgatullin KE, Sibgatullin ES, et al. Method for calculating the strength of massive structural elements in the general case of their stress-strain state (kinematic method). *Stroitel'Nye Materialy i Izdeliya=Construction Materials and Products*. 2023;6(3):5-17. DOI:10.58224/2618-7183-2023-6-3-5-17 (In Russ.)

31. Chuyev AS. On the inconsistency of definitions of physical quantities dynamic and kinematic viscosity. *Zakonodatel'naya i prikladnaya metrologiya.* 2012;1:54-60. (In Russ.)

Information about the authors / Информация об авторах

Oleg O. Ivanov, Cand. Sc. (Eng.), Associate Professor, Regional Development Advisor, ANO "Vdokhnoviteli", Korolev, Moscow region, Russian Federation; ORCID 0000-0002-9868-5487; e-mail: iooc4@mail.ru

Viktor N. Dolgunin, D. Sc. (Eng.), Professor, Tambov State Technical University, Tambov, Russian Federation; ORCID 0000-0002-6227-5224; e-mail: dolgunin-vn@yandex.ru

Konstantin A. Kudi, Line Manager, PJSC "MTS Bank", Moscow, Russian Federation; ORCID 0009-0009-5068-2234; e-mail: kostya.kudi@mail.com

Иванов Олег Олегович, кандидат технических наук, доцент, советник по региональному развитию, АНО «Вдохновители», Королев, Московская область, Российская Федерация; ORCID 0000-0002-9868-5487; e-mail: iooc4@mail.ru

Долгунин Виктор Николаевич, доктор технических наук, профессор, Тамбовский государственный технический университет, Тамбов, Российская Федерация; ORCID 0000-0002-6227-5224; e-mail: dolgunin-vn@yandex.ru

Куди Константин А**ндреевич**, руководитель направления, ПАО «МТС-Банк», Москва, Российская Федерация; ORCID 0009-0009-5068-2234; e-mail: kostya.kudi@mail.com

Received 20 December 2023; Accepted 22 February 2024; Published 26 April 2024

Reviews
Nanostructured, nanoscale materials and nanodevices

УДК 004; 531-2; 535; 620-22 DOI: 10.17277/jamt.2024.01.pp.060-074

Technologies for controlled synthesis and characteristics of thin-layer topological nanoobjects and nanoclusters under laser irradiation on solid targets: algorithms and modeling, quantum bistability in 1D-microstructuresand analogy with carbon nanotubes

© Dmitry N. Bukharov[a], Timur A. Khudaiberganov[a], Alexey G. Tkachev[b], Sergei M. Arakelian[a]✉

[a] *Vladimir State University named after Alexander and Nikolay Stoletovs, 87, Gorky St., Vladimir, 600000, Russian Federation;*
[b] *Tambov State Technical University, Bld. 2, 106/5, Sovetskaya St., Tambov, 392000, Russian Federation*

✉ arak@vlsu.ru

Abstract: The paper presents the results obtained from the studies of the processes of controlled laser synthesis of nanocluster / island nanofilms of different topological configurations of tens and hundreds of nanometers. The findings on structures with lead telluride (PbTe) and quantum bistability in a polariton-exciton system are considered separately. The analysis of the algorithms and computational models used to solve these problems are carried out, and a number of obtained and observed images for different surface nanostructures are presented. These issues are also considered in terms of the topological configuration influence, e.g. on the surface electrical conductivity of the samples under study, as well on other functional characteristics. The phenomenon of quantum bistability in the model of excitonic polaritons and the corresponding modes of its manifestation in 1D-columnar-type semiconductor microcavities, which can be considered as analogues of systems with carbon nanotubes, are also briefly discussed. It is modern advances in the technology of their production on an industrial scale, including bundles and threads of nanotubes, that allow talking about the possibility of their widespread usein micro-nanoelectronics, in particular, as elements of logic devices of various types, as well as sensitive universal sensors for various applications.

Keywords: topological nanostructure; thin films; surface electroconductivity; laser experiment; models and algorithms; quantum bistability in 1D-system; analogy with carbon nanotubes.

For citation: Bukharov DN, Khudayberganov TA, Tkachev AG, Arakelian SM. Technologies for controlled synthesis and characteristics of thin-layer topological nanoobjects and nanoclusters under laser irradiation on solid targets: algorithms and modeling, quantum bistability in 1D-microstructuresand analogy with carbon nanotubes. *Journal of Advanced Materials and Technologies*. 2024;9(1):060-074. DOI: 10.17277/jamt.2024.01.pp.060-074

Технологии управляемого получения и характеристики тонкослойных топологических нанообъектов и нанокластеров при лазерном воздействии на твердые мишени: алгоритмы и моделирование, квантовая бистабильность в 1D-микроструктурах, аналогии с углеродными нанотрубками

© Д. Н. Бухаров [a], Т. А. Худайберганов[a], А. Г. Ткачев [b], С. М. Аракелян[a]✉

[a] *Владимирский государственный университет им. Александра Григорьевича и Николая Григорьевича Столетовых, ул. Горького, 87, Владимир, 600000, Российская Федерация;*
[b] *Тамбовский государственный технический университет, ул. Советская, 106/5, пом. 2, Тамбов, 392000, Российская Федерация*

✉ arak@vlsu.ru

Аннотация: Приведены результаты исследований процессов управляемого лазерного синтеза нанокластерных / островковых нанопленок разной топологической конфигурации в десятки и сотни нанометров. Отдельно рассмотрены результаты по структурам с теллуридом свинца (PbTe) и квантовой бистабильности в поляритонно-

экситонной системе. Проведен анализ используемых алгоритмов и расчетных моделей для решения данных задач и приведен ряд полученных и наблюдаемых изображений разных поверхностных наноструктур. Такие вопросы рассмотрены и в аспекте их влияния, например, на поверхностную электропроводимость исследуемых образцов, а также и на другие их функциональные характеристики. Конспективно обсуждается явление квантовой бистабильности в модели экситонных поляритонов и соответствующие режимы ее проявления в полупроводниковых 1D-микрорезонаторах столбчатого типа, которые могут быть рассмотрены как аналоги систем с углеродными нанотрубками. Именно современные достижения в технологии их производства в промышленном масштабе, включая пучки и нити нанотрубок, позволяют говорить о возможности их широкого применения, в частности в микро- и наноэлектронике, как элементов логических устройств разного типа, а также чувствительных универсальных сенсоров разного предназначения.

Ключевые слова: топологические наноструктуры; тонкие пленки; поверхностная электропроводимость; лазерный эксперимент; модели и алгоритмы; квантовая бистабильность в 1D-системах; аналогия с углеродными нанотрубками.

Для цитирования: Bukharov DN, Khudayberganov TA, Tkachev AG, Arakelian SM. Technologies for controlled synthesis and characteristics of thin-layer topological nanoobjects and nanoclusters under laser irradiation on solid targets: algorithms and modeling, quantum bistability in 1D-microstructuresand analogy with carbon nanotubes. *Journal of Advanced Materials and Technologies*. 2024;9(1):060-074. DOI: 10.17277/jamt.2024.01.pp.060-074

1. Introduction

When synthesizing island nanocluster structures on a solid surface with the required/controlled topology/morphology and functional characteristics, the occurring physical processes of a diffusion nature have a decisive influence on the topological features that determine the formed functional properties. In this case, it is necessary to analyze the algorithms and models used to solve these problems and obtain images of different nanoconfigurations. This affects the surface electrical conductivity of the samples under study.

Under certain synthesis conditions, such structures can have a disconnected topology with a large number of isolated nanoclusters/islands. Samples with a connected topology with the presence of objects united with each other in the form of clusters of a certain type can also be obtained. It is in this aspect that specific features of methods for laser-induced controlled production of nanocluster structures of different classes should be considered in comparison with other technologies used.

Nanocluster structures/island films are defined as granular nanostructures with frame object sizes from 10 nm to 20 μm [1, 2] and, for example, according to electrophysics, with a surface resistance from 10^6 to 10^{13} Ohm·cm^{-1}. Such structures may have unique electrical properties due to size effects [2–5].

Thus, in nanostructures consisting of a system of quantum dots [2], depending on the distance between them, the implementation of various mechanisms of electrical conductivity is possible – from the tunnel effect to the thermionic mechanism [6, 7]. All these features make it possible to widely use semiconductor and metal nanocluster/island structures for problems in the micro-nanoelectronics industry, science and technology, based on new physical principles [8–12]. Here, the emphasis is on obtaining modes with quantum bistability in the model of excitonic polaritons in semiconductor-type excited 1D-microcavities, which can be considered as analogues of systems with carbon nanotubes with different periodic inhomogeneities, i.e. superlattices, with different elemental inclusions/vacancies.

Carbon materials are important in the development of new technologies, especially with 1D-structures in different configurations [13]. Special attention should be paid to carbon nanotubes and threads, which make it possible to obtain 1D-carbon structures of record length [14] with unique capabilities for practical use in a variety of fields. Moreover, the presence of both single-walled and multi-walled carbon nanotubes in structure has its own specific areas of application [15–17]. Therefore, in connection with such a wide demand for such objects, their large-scale production, which has been mastered on an industrial scale for many years, is relevant. First of all, the developments and achievements presented in [18, 19]should be mentioned. The analysis of the state and development trends of nanoindustry objects carried out in these works allows us to conclude that, indeed, one of the most promising areas of nanotechnology is the synthesis of carbon nanomaterials – fullerene-like structures, which are a new allotropic form of carbon (compared with [19]) in form of closed framework, macromolecular systems. In carbon nanotubes, which, having a diameter of 1–50 nm and a length of up to several microns, form a new class of quasi-one-dimensional nanoobjects with the implementation of a number of unique properties due to the ordered structure of their nanofragments: good electrical conductivity and adsorption properties, the ability for

cold electron emission and gas accumulation, diamagnetic characteristics, chemical and thermal stability, as well as high strength combined with high elastic deformation values. It is important to note that at the same time many fundamental scientific problems have been solved, which contributed to such world-class results [20, 21]. A fundamental role plays the choice of the appropriate catalyst during the pyrolysis process, which is not at all an easy task because the selected material, due to its active surface, becomes unusable and has to be renewed, stopping the technological process. If the technological problem of its production has already been practically solved by now in the mentioned works, then the field of their application with different implemented functional modes for optoelectronics problems is still only at the initial stage.

Indeed, recent studies [22] have shown that the creation of new, more efficient catalysts with improved properties is possible with metal atoms with a nonzero total electronic spin moment.

Therefore, the study of polariton states and spin effects in 1D-nanostructures makes it possible to develop various multifunctional devices, in particular, spin transistors and other products, including elements of a quantum computer [23]. This interdisciplinary topic also has its own interest in terms of the optimal method for obtaining the necessary additives/modifiers that improve functional characteristics and quality of various alloys, including high-entropy ones [7, 13, 16, 19].

In this aspect, the use of nanotechnology in electronics makes it possible to create innovative devices of a new class with higher technological and consumer characteristics [24, 25]. This is especially promising for systems with different surface shapes, in particular, spherical and cylindrical. It is some modification of the technology for the production of carbon nanotubes that apparently makes it possible to obtain such elements in terms of the implementation of the corresponding advanced technical processes.

In this work, the emphasis is on using the achievements of nonlinear dynamics and quantum technologies to solve problems of controlled production of topological nanoobjects, including thin-layer cluster structures on a solid surface under laser irradiation of targets of various types. The intensity of the laser radiation used, the scanning speed of the laser beam over the surface being processed, the number and duration of laser pulses affecting the material are the key control parameters in such technologies for synthesizing the topological features of the formed nanostructured configurations. At the same time, we analyze the most suitable algorithmic approaches for implementing modeling and predicting the expected characteristics of such objects. This corresponds to modern world priorities with a variety of model-theoretic and experimental methods, both for the development and for studying the properties of such structures for widespread implementation. Huge financial resources are being invested in this industry to achieve competitive commercialization, which is very important for our country when solving the problems of technological sovereignty. And first of all, we are talking about the production of carbon 1D-structures such as nanotubes, which, due to their configuration and different fillers, have a large dipole moment and high electrical polarizability in one preferred direction. This should make it possible to obtain structures with unusual electrical characteristics under conditions of real phase transitions with symmetric modification and rearrangement of electronic states. These issues are also discussed in this paper.

2. Methods for laser-induced synthesis of nanocluster structures with controlled topology

Among the wide variety of modern methods for the controlled synthesis of nanocluster/island films, laser methods can be considered as a simple and practical alternative that allows obtaining samples of the required quality on various surfaces [26]. For example, using the well-known laser ablation method, it is possible to quite conveniently and efficiently synthesize a nanocluster/island film on a solid substrate due to the deposition of a vapor-gas cloud with nanoparticles and/or nanoclusters [27–29]. Indeed, using the limited laser ablation mechanism, considered in [27–29], in the case of an effective penetration of radiation depth of a smaller film thickness, makes it possible to obtain samples with an increase in efficiency up to 10 times compared to the standard laser ablation process. Moreover, it was shown in [29] that such laser synthesis in the field of high-power femtosecond laser pulses made it possible to conveniently control the surface anisotropy of the resulting samples and, under certain conditions, to form new physical properties in them, for example, treated silicon samples showed an increase in the film conductivity by 3 orders of magnitude compared to the conductivity of untreated amorphous hydrogenated silicon.

In the future, a two-stage process can be implemented – first, the process of laser ablation of the target in a liquid to obtain a colloid, and then deposition from it using laser irradiation and implementation of the synthesis of nanoclusters and

their required distribution on the surface of another solid-state sample, i.e. a substrate placed in a colloid. This is done in a controlled manner using another laser beam [29–31], when varying the initial profiles of the energy density of laser radiation, the duration of its pulse, the speed and trajectory of their scanning in a certain interval, as well as the realized pressure in the vapor-gas cloud above the surface, depending on the scheme laser experiment, makes it possible to obtain samples with the required topological configuration.

Thus, such generation-recombination deformation and defect-deformation instabilities on a solid surface can be induced by controlling parameters of the applied laser radiation. These instabilities disrupt the order of surface and bulk structures [32, 33] and make it possible to synthesize samples with the required topology, including extended structures such as nanotubes, and achieving the required functional/structural characteristics.

The discussed nanocluster structures using laser ablation in liquid are now widely used. A group of these methods is based on the fact that, on the one hand, extreme conditions can locally arise in a liquid due to non-stationary and unstable processes in the laser field, which leads to phase transitions (in particular, micro-nanodiamonds can arise from a graphite target [13]. On the other hand, when exposed to continuous laser radiation on the colloid obtained as a result of ablation, ensembles of nanoparticles with a narrow bimodal size distribution can appear on the surface of, for example, a semiconductor sample [32–34], which makes it possible to control the dimensional quantum electronic states of materials.

Laser methods are also characterized by important features in the production of multilayer thin films of complex compounds on a substrate, which under normal conditions do not form compounds with each other. At the same time, laser-induced nanocluster structures are characterized by chemical purity, with a minimum amount of impurities. These methods for obtaining nanostructures of different configurations and topologies with a spatial distribution on the surface are quite simple and technologically advanced, and their main feature is the possibility of flexible control of the shape and size of the resulting nanostructures, determined both by the properties of the medium and spatiotemporal (up to micrometers and femtoseconds, respectively) laser radiation parameters and in various laser experiment schemes.

As a modified method in the laser ablation scheme, deposition of nanoclusters from a colloid using droplet technology can be applied, followed by evaporation of the liquid component [35]. This method makes it possible to form the required both compact and extended structures in a controlled manner, which is associated with the dependence of the morphology of the deposited layer on the properties of the liquid fraction, colloid particles, temperature of the drop and substrate, as well as the rate of evaporation of the liquid component.

All this allows us to confidently conclude that laser synthesis is a fairly simple, technologically advanced and convenient method that makes it possible to obtain nanocluster structures with the required, often new and unique properties in a controlled manner.

Next, we will present some of our results on laser technologies for producing nanocluster topological structures of various configurations on the surface of a solid body in a controlled manner, both experimentally and with justification within the framework of a number of model approaches used.

2. Models and algorithms for obtaining nanocluster systems with controlled functional characteristics (electrophysics and optics)

2.1. Topological fractal structures

The use of a mathematical/computer modeling apparatus to obtain a system of nanoclusters makes it possible quite conveniently and with the required accuracy to evaluate and describe the geometric features that determine a number of their properties (electrophysical, optical, thermodynamic).

In this case, all models can be conditionally divided into the four classes below [36].

1. Models of atomic mobility.
2. Structural models of the cluster.
3. Electronic shell models.
4. Models of self-organizing clusters (fractal models).

It is convenient to describe the geometric features of nanocluster samples obtained by laser methods within the framework of models from the fourth class. These models of self-organizing clusters (fractal models) [37], which we will consider, are used to describe the geometric features of nanostructures during cluster aggregation, when a decrease in the average density of matter in the volume of the material with clustering [38] is observed during the self-assembly process. The most popular models in this approach are diffusion-limited aggregation (DLA) and cluster-cluster aggregation (CCA) [39].

Using fractal methods, which involve calculating fractal dimensions, it becomes possible to classify the resulting surface nanofilms according to their structure. We used this approach to calculate the fractal dimensions of the resulting nanocluster structures in comparison with their sizes with standard fractals classified in nonlinear dynamics [40–42].

To assess the possibility of synthesizing structures with the required topology, we compared the relief of the obtained samples and their fractal dimensions with the measured parameters of laser radiation at which they were realized.

The study of AFM images (obtained using an atomic force microscope) demonstrates the fractal nature of nanocluster films, which is determined by comparing the fractal dimensions of the samples with the dimensions of standard fractals with fairly good accuracy, when their difference does not exceed a value of the order of 10 %.

Let us present a number of examples obtained structures (both in experiment and in modeling) for the semiconductor material of lead telluride PbTe in the circuit shown in Fig. 1. The system of nanoclusters was synthesized by laser irradiation of epitaxial PbTe films obtained by industrial method. For irradiation, a YAG: Nd^{3+} laser with a Gaussian beam profile (at a wavelength of 1.06 μm) with an optical absorption length $h_{abs} \sim 10^{-5}$ cm was used, operating in a continuous scanning mode over the film surface with its speed varying from 40 to 160 μm·s^{-1} [43, 44]. Scanning of the laser beam over the sample surface was carried out by moving the coordinate table on which the sample was located. The laser radiation power ranged from 5 to 12 W, the intensity (I_l) varied from 10^4 to 10^6 W·cm^{-2}, respectively. The laser beam diameter varied from 30 to 100 μm.

With the used laser radiation power and good heat removal of the silicon substrate and with a large thickness (1.5–2.5 μm) of the irradiated film, it was possible to synthesize nanoclusters in the solid-phase laser nanomodification mode. For power values outside this range of values, the PbTe surface was either not modified at all (Fig. 2*a*) or melted (Fig. 2*b*).

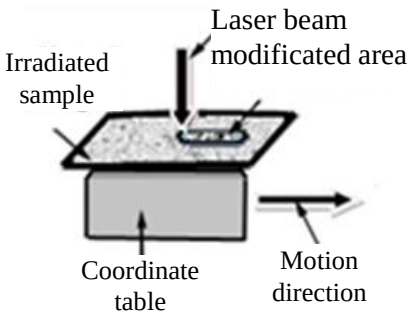

Fig. 1. Experimental scheme of PbTe nanoclusters laser synthesis

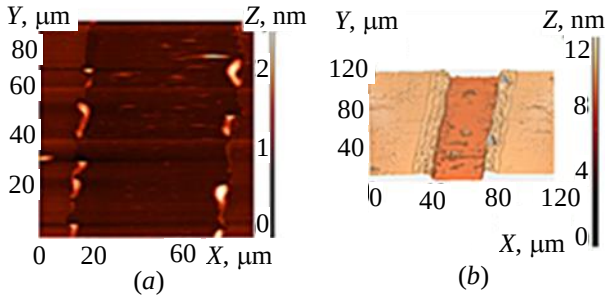

Fig. 2. AFM image of the PbTe epitaxial film surface after laser exposure from a source with power of 5 W (*a*), 12 W (*b*)

Modification of the laser experiment conditions made it possible to identify the most convenient synthesis mode in terms of the relationship between the heating area, the diameter of the laser beam, and its scanning speed over the film surface. This mode was achieved at a scanning speed of the laser beam over the surface of 80 μm·s^{-1} while varying its diameter from 30 to 100 μm.

This allowed synthesizing samples with different topological surface characteristics (Figs. 3, 4).

Figures 3*a*, *b* show examples of systems of dendritic nanoclusters, the shape of which can be described in terms of DLA fractals. Figures 3*c*, *d* show ensembles of nanoclusters that arose through the percolation mechanism of their formation in a laser field.

Dendritic nanoclusters were synthesized at laser powers of 7 W (Fig. 3*a*) and 8 W (Fig. 3*b*), when the scanning speed of the laser beam was 80 μm·s^{-1}, while maintaining the laser beam diameter the same for both powers – 50 μm. The calculated fractal dimensions for these images were 1.737 and 1.834, respectively.

Systems of nanoclusters with a percolation relief were synthesized at a laser radiation power of 6.5 W (Fig. 3*c*) and 6 W (Fig. 3*d*) at a laser beam scanning speed of 75 μm·s^{-1} with the same diameter of 50 μm. An assessment of their fractal dimensions gave values of 1.841 and 1.867, respectively. The indicated accuracy of the fractal dimension values corresponds to that accepted for the classification of fractals [39].

Figure 4 shows images of samples of a system of PbTe nanoclusters with a structure comparable to a labyrinth [43, 44]. It is these labyrinthine structures that are close in geometry to nanotubes of different elemental/chemical compositions.

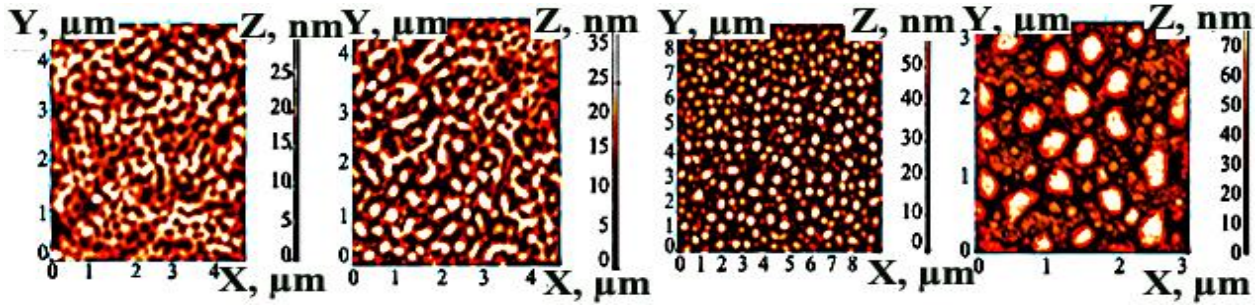

(*a*) (*b*) (*c*) (*d*)

Fig. 3. AFM images of PbTe cluster structures: samples with dendritic (*a*, *b*) and percolation (*c*, *d*) reliefs

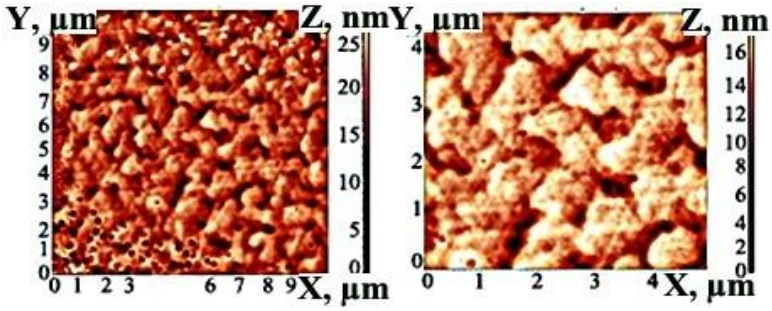

(*a*) (*b*)

Fig. 4. AFM images of PbTe cluster structures with a labyrinthine relief: radiation power 8.5 W, motion speed 70 μm·s^{-1} (*a*); radiation power 9 W, motion speed 60 μm·s^{-1} (*b*)

To obtain them, a laser radiation source with a beam diameter of 50 μm was used. For the sample from Fig. 4*a*, the power was 8.5 W, the motion speed of the coordinate stage (laser beam scanning) was 70 μm·s^{-1}. For the sample from Fig. 4*b*, the power was 9 W and the speed was 60 μm·s^{-1}. The estimated fractal dimensions did not exceed 1.972 and 1.994, respectively.

A study of fractal dimensions calculated for AFM images of samples obtained at different stages of synthesis shows that they increase with increasing laser exposure time, and the structure of objects passes from percolation to dendritic and then to labyrinthine. Thus, from a system of isolated clusters with a disconnected topology, a unified configuration structure with a connected topology is formed.

The above data adequately describe the obtained samples, images of which are shown in Fig. 3, with an error of no more than 10 %, which also does not contradict the theoretical models involved. Thus, the percolation structure with fractal dimension $D = 1.737$ from Fig. 3*b* was obtained during irradiation time $t = 0.29$ s. Similarly, a dendritic system with a larger fractal dimension $D = 1.867$, shown in Fig. 3*c*, was synthesized over a longer irradiation time – 0.31 s. In the case of the formation of a labyrinthine sample with an even larger fractal dimension $D = 1.972$ (Fig. 4*a*), the laser exposure time increased to 0.36 s.

Thus, a connection between physical processes and synthesis mechanisms caused by laser exposure and the formed geometric features and corresponding fractal characteristics has been established.

Standard fractal models, for example, such as DLA, in the case of constructing a horizontal projection, do not allow taking into account the heterogeneity of the relief of the model system of nanoclusters in height. This limitation can be avoided by labeling the model cells according to the height of the actual granules in AFM images. Such labeling can be done using cluster analysis for different bead colors corresponding to different heights for AFM images. This procedure was implemented using the K-means algorithm in the MATLAB environment [45–48]. Thus, the model particles received height values with given probabilities proportional to the sizes of the formed granules. Figure 5 shows a cluster film model obtained according to the above approach. In this case, Fig. 5*a* shows a sample of a PbTe film; Fig. 5*b* shows the distribution of heights as a result of clustering; and Fig. 5*c* shows the model structure of the cluster system built in the DLA approximation, taking into account the color marking of the relative heights of the forming granules. Thus, the specified structure was built with the probability of aggregation/adhesion $s = 0.1$. This probability s determines the process of agglomeration of nanoparticles into the corresponding ensembles. The fractal dimension was $D = 1.89$ and differed from the dimension of the sample as a whole by an amount of the order of $2 \cdot 10^{-2}$.

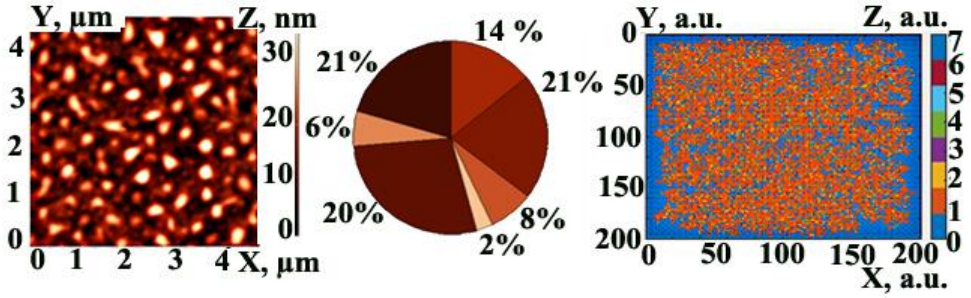

(*a*) (*b*) (*c*)

Fig. 5. DLA model of a nanocluster structure taking into account the height of the resulting nanoclusters: AFM image (*a*); distribution of shares of colors that determine heights (*b*); DLA model: 0 – substrate, 1–8 particles/nanoclusters heights (*c*)

The given parameters are important when it is important to know the local characteristics leading to gains, for example, in the local functional parameters of the electric field at the edge of emerging in homogeneities.

Thus, the proposed method for classifying nanocluster samples, as well as selected models that allow quantitative comparison with the results of experimental synthesis, show fairly good adequacy and can be used to describe the geometric features of a fairly wide class of laser-induced structures.

2.2. Models of electrical conductivity of nanocluster/island films

One of the fundamental factors that has a noticeable effect on the electrical conductivity of nanocluster/island films is the topology of their structure, but it does not even always depend on their elemental/chemical composition. Indeed, the nature of the location, distance, formation and size of individual nanoclusters form the original topology of their ensemble on a solid surface, which determines one or another type of electrical conductivity. In particular, it is customary to distinguish three types of basic models:

1) dielectric model [49];
2) percolation model [50];
3) metal model [51].

In the case of samples with a connected cluster topology, percolation or metallic type approximations are applicable to describe electrical conductivity. To describe the electrical properties of structures with a disconnected topology, a dielectric model can be used.

Particularly important for various applications is the low-temperature thermal activation mechanism of electrical conductivity, which is hopping conduction referring to the tunneling of electrons between neighboring localization centers (clusters) [52].

The hopping conductivity model allows estimating the average electrical conductivity of the system or the diffusion coefficient of nanoparticles. Electrical conductivity in such systems is realized through the description of random walks of electrons along randomly located localized impurity centers [52]. To estimate the conductivity, a semi-phenomenological method based on the Miller–Abrahams random grid of resistances [53] and percolation theory [54] is used. The microscopic approach, which consists in describing the wandering of a particle through random nodes, is also popular [55]. These models can be used as first approximations and make it possible to achieve agreement between experimental measurements and calculated values at a qualitative level; quantitative agreement is achieved by introducing correction values into them, which allow achieving satisfactory errors not exceeding 10 %.

Subsequently, the basic model of tunneling charge transfer was improved [56]. It takes into account the decrease in the potential barrier caused by the polarization interaction between granules and the tunneling electron, which allows evaluating the effect of the substrate on conductivity through a description of electron tunneling along the dielectric substrate due to the thermal activation effect.

This approximation makes it possible to achieve good modeling accuracy for nanofilms consisting of small ellipsoids with dimensions of the order of 4 nm and slightly smaller average gaps between them.

In the case of a distance between nanoclusters of more than 10 nm, it is preferable to carry out modeling taking into account the influence of the substrate.

In addition, further improvements to the basic model consider the influence of the sizes and shapes of granules, when charge transfer from a larger charged granule to a smaller neutral granule is realized due to the effect of thermal activation.

Nanocluster ensembles, in which there are systems of elongated interconnected structures, have lower resistance than rarefied samples. In this aspect,

single carbon nanotubes with a significant decrease in electrical resistance due to their high polarizability along a preferred direction (1D structure [12]) are of particular interest. Their electrical conductivity is generally described by percolation models based either on lattice approximations or random displacements, which make it possible to take into account the distribution of an ensemble of structures, including in the 1D-configuration, on the substrate.

Thus, today there are many works where the electrical properties of semiconductor nanostructures are studied with an emphasis on the heterogeneity of the structure [57, 58] and fractal structures [3, 59, 60]. A number of fairly universal model approximations have also been developed with the ability to quantify the accuracy of calculations, allowing to take into account the features of the simulated systems and their connections with the parameters of the models and experimental synthesis schemes.

Such systems define new possibilities in electrophysics using nanostructured materials, which is promising for the development of micro-nanoelectronics base elements operating on new physical principles.

3. Microstructures for quantum states of a system with quasiparticles in 1D-columnar-type microcavities

Let us consider structures with 1D-type microcavity elements with quantum characteristics for excitation of excitonic polaritons which are important in terms of possible application [61, 62].

Excitonic polaritons were discovered in various microcavity structures (planar, microwires and microcolumns) with different active fragments – quantum wells, quantum dots [63–65]. In this section we will briefly consider the formation of excitonic polaritons in semiconductor (GaAs, ZnO, GaN, etc.) low-dimensional structures: 1D-semiconductor microcavity – microcolumn and/or microwires. Such models can also describe carbon nanotubes with a certain structure along their length – both single-core and double-core with a certain quantum connection between them.

To create excitonic polaritons, it is necessary that excitons continuously interact with coherent photons, and the energy of this interaction exceeds the energy of dissipation in the system. For this purpose, microcavities/micropillars, such as Fabry-Perrot optical resonators but of subwavelength sizes, are used. In this case, excitons are formed in low-dimensional quantum structures of the Bragg type (with quantum wells or quantum dots) installed in the antinode region of the standing wave of the microcavity [66]. The microcavity structure is shown in Fig. 6 in the form of a microcolumn.

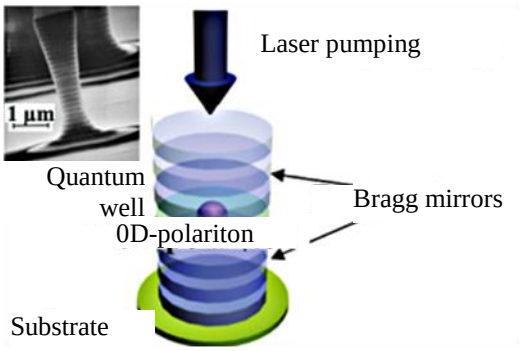

Fig. 6. Schematic of the microcolumn/micropillar design. The inset on the left is a micrograph of a GaAs/AlAs-based microcolumn with a nominal diameter of 1.3 μm and a length of 6 μm

Such structures of columnar microcavities are obtained from a semiconductor material by etching [67], and approaches to their quantum description are considered in [68–70].

Numerical modeling of the main kinetic equation of the problem was carried out using the qutip computer library in Python [65].

The excitation of polariton states in a microcolumn was carried out by a coherent laser, the frequency of which ω_d is close to both the photonic ω_{ph} and exciton ω_{ex} resonances in the microcolumn. In the model Hamiltonian (see below (1)) of two coupled oscillators, the cubic type nonlinearity on one oscillator – the exciton mode (nonlinearity parameterα) was taken into account, and external coherent control of the second oscillator – the photon mode was accepted.

The Hamiltonian $\hat{H}_C$ of the exciton-polariton system (the creation operators $\hat{\varphi}^+$ and annihilation $\hat{\varphi}$ for the photon and, accordingly, for the exciton – $\hat{\chi}^+$ and $\hat{\chi}$) in the rotating wave approximation has the following form [66, 67]:

$$\hat{H}_C = \hbar\Delta_{\text{ph}}\hat{\varphi}^+\hat{\varphi} - \hbar\Delta_{\text{ex}}\hat{\chi}^+\hat{\chi} + \hbar\omega_R\left(\hat{\chi}^+\hat{\varphi} + \hat{\varphi}^+\hat{\chi}\right) + \\ + \hbar\alpha\hat{\chi}^{+2}\hat{\chi}^2 + \hbar E_d\left(\hat{\varphi}^+ + \hat{\varphi}\right), \qquad (1)$$

where E_d is the amplitude of the laser field (pumping) and the following designations for frequency detunings are introduced: $\Delta_{\text{ph}} = (\Delta - \Omega) = \omega_{\text{ph}} - \omega_d$ is detuning of the photon mode frequency from the laser pumping frequency ω_d; $\Delta_{\text{ex}} = (\Delta + \Omega) = \omega_d - \omega_{\text{ex}}$ is detuning of the exciton mode frequency from the pump frequency; $\Delta = \left(\omega_{\text{ph}} - \omega_{\text{ex}}\right)/2$ is half of the exciton-

photon detuning; $\Omega = \omega_d - (\omega_{ph} + \omega_{ex})/2$ is detuning of the pump frequency from the middle between the frequencies of the eigenstates of the exciton-photon system (laser detuning). The third term in Hamiltonian (1) corresponds to the energy of exchange interaction between excitons and photons, i.e. describes the mutual transformation of photons into excitons and, vice versa, at the Rabi frequency ω_R in the strong coupling mode (when the frequency of mutual transformations of excitons and photons exceeds losses in the system). Nonlinearity (the fourth term) in the polariton system arises due to the elastic scattering of excitons in the Coulomb field of the exciton gas.

The basic kinetic equation for the density matrix ρ of an exciton-polariton system in an exciton-photon basis can be written in the following form [68–70]:

$$\frac{\partial \rho}{\partial t} = \frac{1}{i\hbar}\left[\hat{H}_C, \rho\right] + \gamma_{ph}\left(2\hat{\varphi}\rho\hat{\varphi}^+ - \rho\hat{\varphi}^+\hat{\varphi} - \hat{\varphi}^+\hat{\varphi}\rho\right) + \\ + \gamma_{ex}\left(2\hat{\chi}\rho\hat{\chi}^+ - \rho\hat{\chi}^+\hat{\chi} - \hat{\chi}^+\hat{\chi}\rho\right), \qquad (2)$$

where γ_{ph} and γ_{ex} are dissipations into the photon and exciton modes, respectively.

The energy outflow (dissipation of photons or excitons) from the exciton-polariton system leads to the damping of polariton states with a characteristic lifetime of the order of 10–100 ps. Dissipation is compensated by pumping – coherent (laser) or incoherent (electrical injection of hot excitons).

In semiconductor physics, it is more convenient to use energy units in millielectronvolts (meV) and the time scale of processes in picoseconds (ps), which is characteristic of the lifetime of polaritons. Calculations were carried out in the system where $\hbar = 0.658$ meV·ps is Planck's constant. For calculations, the following typical values of the parameters of the exciton-polariton system are used [67–69]: $\hbar\alpha = 0.001$ meV, $\hbar\omega_R = 2.5$ meV, $\gamma_{ex} = 10$ GHz and $\gamma_{ph} = 100$ GHz.

The pump intensity in this conditional parameterized form is related to the real physical value of the intensity of laser radiation incident on the microcavity $I_{in} = I_d \dfrac{\hbar\omega_d}{\gamma}$, γ is the loss of pump radiation on the Bragg mirrors and inside the microcavity; it can be equal to γ = 10 GHz. Then the reduced unit of value 1 ps^{-2} (at laser pump wavelength Λ = 0.850 μm corresponds to a value of 240 $W \cdot cm^{-2}$.

Without dwelling on the details of the calculation [68–69], Figure 7 immediately presents its results with obtaining bistable modes [70]. Such modes are of fundamental importance for applications in micro-nanoelectronics, in particular, when they are implemented, for example, using carbon nanotubes.

The shown diagram of the existence of the bistability effect depending on the exciton-photon detuning Δ and the pump frequency detuning Ω with a color scale corresponds to the pump intensity threshold value, above which the bistability effect appears. The effect of photon mode bistability for the system parameters, shown with an asterisk in Fig. 7*a*, is depicted as a parametric S-loop of the dashed curve in Fig. 7*b*.

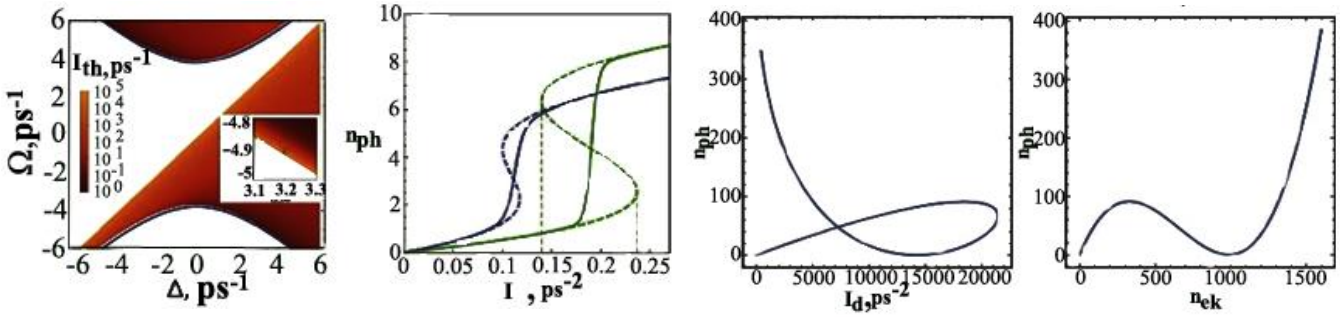

(*a*) (*b*) (*c*) (*d*)

Fig. 7. *a* – diagram of the bistability existence depending on detuning Δ and Ω. The shaded area corresponds to such system parameters when a bistability effect can be observed in the system. The color scale shows the pump intensity threshold $I_d \equiv |E_d|^2 = I_{th}$, at which the bistability of the system under consideration will manifest itself; *b* – photon mode population obtained within the mean field approximation (blue/green dashed curve) and using the quantum solution (blue/green solid curve) for parameters conventionally designated as ps (see in the text of the paper): Δ = 3.2 ps^{-1} and Ω = –4.91 ps^{-1} and Ω = –4.89 ps^{-1} (the values of these parameters are shown with colored dots in panel

(*a*)); *c*, *d* – diagram of stationary values of the number of photons nph depending on the pump intensity I_d (*c*) and the number of excitons n_{ex} (*d*). Parameters: Ω = 0, Δ = 3ps^{-1}

The analysis of the bistability existence showed that there are two ranges of values of the parameters Δ and Ω, where the effect of bistability manifests itself (see Fig. 7*a*). Moreover, both of these regions are limited by natural frequencies – the lower and upper polariton branches $\omega_{LP,UP} = \pm\sqrt{\omega_R^2 + \Delta^2}$ and are shifted upward by a frequency that is proportional to the loss level. Bistability in the region of the lower dispersive polariton branch occurs if the detuning Ω is not less than the blue shift, and also provided that $\Delta > \sqrt{3}\gamma$. It is also worth noting that there is no bistability in the central region, and approaching this region increases the threshold for the onset of the bistability effect.

In a nonlinear multicomponent system in a stationary mode, in addition to the bistability effect, the opposite effect can also be observed at different pumping intensities, but at the same value of the number of photons n_{ph}. In Figure 7*c* this effect is shown in the form of a loop depending on the number of photons on pumping. This effect is explained by the nonlinear dependence of the photon field on the exciton field in the stationary mode (and thus, the more complex ambiguous dependence of the photon field on the pump intensity). Complete depletion of the photon mode is possible at a certain value of the pump intensity (see Fig. 7*c*). In this case, the parametric curve of the number of photons versus the number of excitons shows the opposite effect of bistability, when the same value of the number of photons can be achieved with a different number of excitons (see Fig. 7*d*).

The mean field approximation predicts two dynamic stable stationary states in the bistability region (blue curve in Fig. 7*b*). In classical stability theory, the upper and lower states of the bistability loop are dynamically stable according to Lyapunov [68]. However, this statement is not true in the presence of significant noise. If the noise (quantum, thermal or technical) is sufficiently intense, it causes the system to switch from one stable state to another and vice versa [69].

Although such instability of bistable states to noise may prevent the creation of logic elements with bistable characteristics (for the operation of such logic devices this represents the decoherence time), if the operating time of the device, i.e. switching time, is less than the lifetime on one of the metastable states, then quantum jumps between two metastable states make it possible to implement useful quantum devices. We are talking, for example, about encoding quantum information on two metastable states of a nonlinear oscillator exchanging pairs of photons with its environment. This mechanism can provide stability without causing decoherence processes.

The issue of stochastic switching in systems with bistability has already been considered in the context of a dissipative phase transition in single-mode and multimode systems [68–70].

An analogue of such processes in multi-walled carbon nanotubes can be carried out for various functional phenomena when they are used as logic elements, including extended ones with multiple switching modes.

It is important to note that we also analyzed the correlation spectrum between photons and excitons with a defined/adjustable phase shift. However, we will not present here the rather complicated format of such quantum calculations. We only note that at low intensities of laser radiation acting on the system, the phases of excitons and photons are in antiphase. This effect is of fundamental importance for the development of the phenomena of periodic exchange of energy and information in multi-core spatially distributed systems of large length on new physical principles. It is modern advances in the technology of producing carbon nanotubes with internal structures, including their bundles and threads, that can be promising in this field.

4. Conclusion

This paper presents the results obtained from the studies of the processes of controlled laser synthesis of nanocluster/island nanofilms of different topological configurations within the framework of certain algorithms and models with fractal dimensions. Separately, the results on structures with lead telluride (PbTe) with corresponding models of electrical conductivity and the phenomenon of quantum bistability in 1D-columnar-type microcavities upon excitation of excitonic polaritons are considered. The latter objects allow analogies with carbon nanotubes with a certain internal structure.

Varying the parameters of the applied laser radiation, i.e. power, beam shape, scanning speed across the sample, and duration of laser exposure,

makes it possible to synthesize samples with different topologies, including fractal objects. Their structure can be correlated with a number of standard fractals within the framework of certain models for their production – from diffusion-limited aggregation and percolation to a fractal labyrinth – with the corresponding calculated fractal dimensions.

The analysis and classification of the obtained samples showed that there is a deep connection between the topology of the structure and the physical mechanism for obtaining cluster films of a certain configuration, which is due to nonlinear effects and instability of film growth on the substrate surface. This allows controlling the functional characteristics of synthesized objects using a laser experiment. In this case, additional possibilities are associated with the preliminary preparation of granular structures and powders of different chemical compositions for the subsequent synthesis of nanoparticles of a certain shape and a given dispersion in a femtosecond laser experiment [71, 72].

All this allows us to talk about the development of technology for creating elements and systems, in particular micro-nanoelectronics, with specified functional and structural characteristics for specific tasks of their use, based on new physical principles.

In addition, consideration of some quantum states and correlation dependencies in 1D-column-type microcavity systems under conditions of excitation of exciton-polariton states for quantum bistability allows the implementation of new generation logic elements for various applications. In this aspect, 1D structures, including nanotubes, are of the greatest interest and promise.

Indeed, such systems, as analogues of carbon nanotubes with nonlinear wave interaction, for example, in hollow nanotubes, are devices of a new type for various applications with energy exchange of polariton-photonic states.

We are talking about the use of such non-trivial systems in various applications, using advances in nonlinear dynamics and quantum technologies, including stochastic trigger-type switching devices with hysteresis and controlled photon statistics in exciton-polariton systems.

Further experimental studies using the considered effects and states within the framework of the corresponding algorithms and models will contribute to new achievements in the implementation of a number of tasks for the technological sovereignty of Russia based on the development of high-tech technologies of the new generation. In this aspect, single-walled nanotubes as an example of 1D-carbon systems with unique capabilities for their widespread use are of great interest [15, 16, 19, 73]). The fundamental foundations of these technologies were laid relatively long ago [74–77] and now the stage of their implementation in various directions has come.

In this regard, it is worth mentioning the embedding of two-dimensional films of various nanomaterials, in particular graphene, directly into microchips [78]. Using gold inserts, it was possible to successfully connect substrates made of silicon and a number of polymer materials with films of graphene and molybdenum disulfide. This allowed obtaining a set of high-frequency transistors using just one technological operation. The development of this approach should significantly simplify the production of nanoelectronic elements and, at the same time, improve their quality. Considering that the production of carbon nanomaterials of various types has already reached an industrial scale [19], we can admit their widespread use in relevant micro-nanoelectronics applications, including both logic elements and sensitive universal sensors for various purposes.

5. Acknowledgements

The authors are grateful to Candidate of Physical and Mathematical Sciences I.S. Chestnov and Doctor of Technical Sciences Elena Burakova for fruitful discussions and advice on the subject of the research.

6. Funding

This study received no external funding.

7. Conflict of interests

The authors declare no conflict of interest.

References

1. Sidorova SV, Yurchenko PI. Study of the formation of island nanostructures in a vacuum. *Nano- i microsystemnaya tekhnika*. 2011;5:9-11. (In Russ.)

2. Freik DM, Yurchishin IK, Lisuk YuV. Quantum-size effects in nanostructures and problems of thermoelectricity. *Thermoelectrichestvo*. 2012;2:5-30. (In Russ.)

3. Bukharov DN, Kucherik AO, Arakelian SM. Nanocluster fractal electrical conductivity in thin films on a solid surface: dimensional models of different configurations and demonstration of results in a laser experiment. *Journal of Advanced Materials and Technologies*. 2023;8(3):227-251. DOI:10.17277/jamt.2023.03.pp.227-251

4. Kulbachinsky VA. Semiconductor quantum dots. *Sorosovskiy Obrazovatel'nyy Zhurnal*. 2001;4:98-104. (In Russ.)

5. Roduner E. *Size effects in nanomaterials*. Moscow: Tekhnosphere; 2010. 368 p. (In Russ.)

6. Laucht A, Hofbauer F, Hauke N, Angele J, et al. Electrical control of spontaneous emission and strong coupling for a single quantum dot. *New Journal of Physics*. 2009;11:23-34. DOI:10.1088/1367-2630/11/2/023034

7. Sarkar DK, Zhou X, Tannous A. Growth of self-assembled copper nanostructure on conducting polymer by electrodeposition. *Solid State Communications*. 2003; 125(7-8):365-368. DOI:10.1016/S0038-1098(02)00883-9

8. Gribachev V. Nanosensors. *Componenti i Tekhnologii*. 2009;4(93):21-24. (In Russ.)

9. Kryzhanovskaya NV, Maksimov MV, Zhukov AE. Lasers based on quantum dots and microcavities with whispering gallery modes. *Kvantovaya Electronica.* 2014;44(3):189-200. (In Russ.)

10. Aseev AL. Nanomaterials and nanotechnologies for modern semiconductor electronics. *Rossiyskie Nanotechnologii = Nanobiotechnology Reports*. 2006; 1(1-2):97-110.(In Russ.)

11. Ilyichev EA, Nabiev RM, Petrukhin GN, Rychkov GS, et al. Carbon materials in electronics: status and problems. *Izvestiya Vysshikh Uchebnykh Zavedeniy. Elektronika = Semiconductors*. 2011;5(91):18-35. (In Russ.)

12. Garnov SV, Abramov DV, Bukharov DN, Khudayberganov TA, et al. Electrophysics of carbon 1D structures obtained in a laser experiment. *Uspehi fizicheskih nauk = Physics-Uspekhi*. 2024;194(2):115-137. DOI:10.3367/UFNr.2023.12.039620 (In Russ.)

13. Gryaznov KO, Sineva LV, Asalieva EY, Mordkovich VZ. Comprehensive comparison of high-performance Fischer-Tropsch synthesis cobalt catalysts containing different types of heat-conducting frames. *Catalysis in Industry*. 2023;15(1):21-35. DOI:10.1134/ S2070050423010051

14. Tkachev AG, Mikhaleva ZA, Burakova EA. Study of methods for increasing the activity of catalysts for the production of carbon nanostructured materials. *Himicheskaya tekhnologiya = Theoretical Foundations of Chemical Engineering*. 2009;10(2):81-86. (In Russ.)

15. Burakova EA, Litovka YuV, Nesterov VA, Sypalo KI, et al. The concept of controlling the characteristics of nanotubes by processing a catalyst precursor for their synthesis. *Journal of Computer and Systems Sciences International*. 2022;61(5):843-857. DOI:10.1134/S1064230722050057

16. Burakova EA, Litovka YuV, Nesterov VA, Sypalo KI, et al. The concept of controlling the characteristics of nanotubes by processing a catalyst precursor for their synthesis. *Izvestiya RAN. Neorii i sistemi upravleniya = Journal of Computer and Systems Sciences International*. 2022;(5):102-117. DOI:10.31857/ S0002338822050055 (In Russ.)

17. Burakova EA, Filatova EYu, Burakov AE, Tkachev AG. Effect of ultrahigh frequencies on catalytic systems for the synthesis of carbon nanomaterials. *Himicheskaya tekhnologiya = Theoretical Foundations of Chemical Engineering*. 2011;12(9):539-542. (In Russ.)

18. Burakova EA, Burakov AE, Ivanova IV, Tkachev AG, et al. Study of the activation of metal oxide catalysts for the synthesis of multi-walled carbon nanotubes. *Vestnik Tambovskogo Gosudarstvennogo Tekhnicheskogo Universiteta*. 2010;16(2):337-342. (In Russ.)

19. Mishchenko SV, Tkachev AG. *Carbon Nanomaterials. Production, Properties, Application.* Moscow: Mashinostroyenie; 2008. 320 p. (In Russ.)

20. Burakova EA. The concept of control of complex technical systems for the production of carbon nanomaterials. *Prikaspijskij zhurnal: upravlenie i vysokie tekhnologii = Caspian Journal: Control and High Technologies*. 2023;61:9-18. DOI:10.54398/20741707_ 2023_1_9 (In Russ.)

21. Ashuiev A, Nobile AG, Trummer D, Klose D, et al. *Active Sites in Cr(III)-based Ethylene Polymerization Catalysts from Machine Learning-Supported XAS and EPR Spectroscopy*. ChemRxiv. Cambridge: Cambridge Open Engage; 2023. 400 p. DOI:10.26434/chemrxiv-2023-34wl2

22. Cao G, Wang Y. *Nanostructures and nanomaterials: Synthesis, Properties and Applications*. World Scientific Publishing; 2011. 581 p.

23. Gulyakovich GN, Severtsev VN, Shurchkov IO. Prospects and problems of semiconductor nanoelectronics. *Injenerniy Vestnik Dona*. 2012;2(20):315-319. (In Russ.)

24. Loktev D, Yamashkin E. Methods and equipment for applying wear-resistant coatings. *Nanoindustriya*. 2007;4:18-25. (In Russ.)

25. Zuev DA, Lotin AA, Novodvorsky OA, Lebedev FV, et al. Pulsed laser deposition of thin ITO films and their characteristics. *Fizika i Tekhnika Poluprovodnikov*. 2012;46(3):425-429. (In Russ.)

26. Eroshova OI, Perminov PA, Zabotnov SV, Gongalsky MB, et al. Structural properties of silicon nanoparticles prepared by pulsed laser ablation in liquid media. *Kristallografiya = Crystallography Reports*. 2012;57(6):942-947. (In Russ.)

27. Domke M, Nobile L, Rapp S Eiselen, Sotrop S, et al. Understanding thin film laser ablation: the role of the effective penetration depth and the film thickness. *Physics Procedia*. 2014;56:1007-1014. DOI:10.1016/j.phpro.2014. 08.012

28. Arakelyan SM, Khudaberganov TA, Istratov AV, Osipov AV, Khorkov KS. Topological laser-induced quantum states in nanocluster structures: fundamental effects and possible applications (electrophysics and

optics). *Optika i Spektroskopiya*. 2019;127(7):125-136. DOI:10.21883/OS.2019.07.47939.113 (In Russ.)

29. Shuleiko DV, Potemkin FV, Romanov IA, Parhomenko IN, et al. Femtosecond laser pulse modification of amorphous silicon films: control of surface anisotropy. *Laser Physics Letters*. 2018;15:056001. DOI:10.1088/1612-202X/aaacf9

30. Drampyan R, Leonov N, Vartanyan T. Laser controlled deposition of metal microstructures via nondiffracting Bessel beam illumination. *Nanophotonics VI*. 2016;9884:98841J. DOI:10.1117/12.2227763

31. Emelyanov VI, Zaitsev VB, Plotnikov GS. Formation and evolution of nanostructures on the surface of semiconductors during laser inelastic photodeformation. *Poverkhnost'. Rentgenovskiye, sinkhrotronnyye i neytronnyye issledovaniya = Journal of Surface Investigation: X-Ray, Synchrotron and Neutron Techniques*. 2008;5:80-87. (In Russ.)

32. Emelyanov VI. Defect-deformation theory of the formation of an ensemble of nanoparticles with a bimodal size distribution during continuous laser irradiation of solids. *Kvantovaya Elektronika = Quantum Electronics*. 2011;41(8):738-741. (In Russ.)

33. Arakelian SM, Kucherik AO, Kutrovskaya SV, Osipov AV, et al. Laser-induced nanocluster thin-film systems with controlled topology and composition: the possibility of creating superconducting structures based on new physical principles. *Crystallography Reports*. 2018;63(7):1173-1177. DOI:10.1134/S1063774518070027

34. Fedotov AYu. Modeling of formation processes and properties of nanostructures and nanofilms formed in a gaseous environment. *Khimicheskaya Fizika i Mezoskopiya.* 2017;19(2):230-249. (In Russ.)

35. Suzdalev IP. *Nanotechnology: Physico-Chemistry of Nanoclusters, Nanostructures and Nanomaterials*. Moscow: URSS; 2008. 589 p. (In Russ.)

36. Roldugin VI. Fractal structures in dispersed systems. *Uspekhi Khimii = Russian Chemical Reviews*. 2003;72(10):931-959. (In Russ.)

37. Zyryanov RS. Development of fractal models of aggregation of colloidal particles. *Molodoy Ucheniy*. 2016;24(128):72-76. (In Russ.)

38. Wei H, Eilers H. From silver nanoparticles to thin films: Evolution of microstructure and electrical conduction on glass substrates. *Journal of Physics and Chemistry of Solids*. 2009;70:459-465. DOI:10.1016/j.jpcs.2008.11.012

39. Kronover PM. *Fractals and chaos in dynamic systems. Fundamentals of theory*. Moscow: Postmarket; 2000. 352 p. (In Russ.)

40. Falconer K. *Fractal Geometry: mathematical foundations and applications*. New York: John Wiley & Sons; 2013. 400 p.

41. Mahanta A, Sarmah H, Paul R, Choudhury G. Julia set and some of its properties. *International Journal of Applied Mathematics & Statistical Sciences (IJAMSS)*. 2016;5(2):99-124.

42. Iudin DI, Koposov EV. *Fractals: from simple to complex*. N. Novgorod: NNGASU; 2012. 200 p. (In Russ.)

43. Bukharov DN, AbramovAS, Novikova OA, Samyshkin VD. Fractal models of the PbTe nanocluster structures on a solid surface. *Journal of Physics: Conference Series*. 2022;2316(1):012013. DOI:10.1088/1742-6596/2316/1/012013

44. Arakelyan SM, Bukharov DN, Emelyanov VI, Zimin SP, et al. Bimodal ensemble of nanoparticles on the surface of epitaxial films of lead telluride under the influence of continuous laser radiation. *Poverkhnost'. Rentgenovskiye, sinkhrotronnyye i neytronnyye issledovaniya = Journal of Surface Investigation: X-Ray, Synchrotron and Neutron Techniques*. 2015;11:41-49. DOI:10.7868/S0207352815110062 (In Russ.)

45. Gonzalez R, Woods R, Eddins S. *Digital image processing in the MATLAB environment*. Moscow: Tekhnosfera; 2006. 616 p. (In Russ.)

46. Dyakonov VP, Abramenkova IV. *MATLAB. Signal and image processing. Special reference book*. St. Petersburg: Piter; 2002. 608 p. (In Russ.)

47. Seroklinov G, Goonko A. Comparative analysis of experimental data clustering in MATLAB and Python environment. *E3S Web of Conferences*. 2023;419:20-25. DOI:10.1051/e3sconf/202341902025

48. Chamundeswari G, Pardasaradhi VG, Satyanarayana Ch. An experimental analysis of K-means using Matlab. *International Journal of Engineering Research & Technology*. 2012;1(5):1-5.

49. Boltaev AP, Penin NA, Pogosov AO, Pudonin FA. Activation conductivity in island metal films. *Zhurnal eksperimental'noy i teoreticheskoy fiziki = Journal of Experimental and Theoretical Physics*. 2004;126:945-961. (In Russ.)

50. Rostovshchikova TN, Smirnov VV, Kozhevin VM, Yavsin DA, Gurevich SA. Intercluster interactions in catalysis by nanosized metal particles. *Rossiyskiye nanotekhnologii = Nanobiotechnology Reports*. 2007; 2(1-2):47-60. (In Russ.)

51. Anfimov IM, Kobeleva SP, Malinkovich MD, Shchemerov IV, et al. Mechanisms of electrical conductivity of silicon–carbon nanocomposites with nanosized tungsten inclusions in the temperature range 20–200 °C. *Izvestiya Vysshikh Uchebnykh Zavedeniy. Materialy elektronnoytekhniki = Modern Electronic Materials*. 2012;2:58-60. (In Russ.)

52. Ravich YuI, Nemov SA. Hopping conduction through highly localized states of indium in PbTe and solid solutions based on it. *Fizika i tekhnika poluprovodnikov = Semiconductors*. 2002;36(1):3-23. (In Russ.)

53. Gantmakher VF. *Electrons in disordered media*. Moscow: FIZMATLIT; 2013. 288 p. (In Russ.)

54. Gallyamov SR, Melchukov SA. Percolation model of conductivity of a two-phase lattice: theory and computer experiment. *Izvestiya Instituta matematiki i informatiki Udmurtskogo gosudarstvennogo universiteta*. 2010; 4:112-122. (In Russ.)

55. Bleibaum O, Böttger H, Bryksin VV. Random-resistor network description for hopping transport in the presence of Hubbard interaction. *Journal of Physics: Condensed Matter*. 2003;15:1719. DOI:10.1088/0953-8984/15/10/319

56. Arakelian SM, Bukharov DN, Emel'yanov VI, Zimin SP, et al. Laser nanostructuring of the PbX thin films for creation of the semiconductor devices with controlled properties. *Physics Procedia*. 2014;56(C):1115-1125. DOI:10.1016/j.phpro.2014.08.026

57. Bengfort M, Malchow H, Hilker FM. The Fokker–Planck law of diffusion and pattern formation in heterogeneous environments. *Journal of Mathematical Biology*. 2016;73:683-704. DOI:10.1007/s00285-016-0966-8

58. Cavaliere E, Ferrini G, Pingue P, Gavioli L. Fractal TiO_2 nanostructures by nonthermal laser ablation at ambient pressure. *The Journal of Physical Chemistry C.* 2013;117(44):23305-23312. DOI:10.1021/jp406603q

59. Cavaliere E, Benetti G, Celardo GL, Archetti D, et al. Aggregation and fractal formation of Au and TiO_2 nanostructures obtained by fs-pulsed laser deposition: experiment and simulation. *Journal of Nanoparticle Research.* 2017;19(9):311. DOI:10.1007/s11051-017-4009-1

60. Budaev VP, Khimchenko LN. Fractal nano- and microstructure of deposited films in thermonuclear installations. *Voprosy Atomnoy Nauki i Tekhniki. Seriya Termoyadernyy Sintez*. 2008;3:34-61. (In Russ.)

61. Kavokin A, Baumberg JJ, Malpuech G, Laussy FP. *Microcavities.* Oxford: Oxford University Press; 2017. 500 p.

62. Sanvitto D, Stéphane K-C. The road towards polaritonic devices. *Nature Materials*. 2016;15(10):1061-1073. DOI:10.1038/nmat4668

63. Gerard JM, Barrier D, Marzin JY, Kuszelewicz R, Manin L. Quantum boxes as active probes for photonic microstructures: The pillar microcavity case. *Applied Physics Letters*. 1966;69(449):1-6. DOI:10.1063/1.118135

64. Löffler A, Reithmaier JP, Sęk G, Hofmann C, et al. Semiconductor quantum dot microcavity pillars with high-quality factors and enlarged dot dimensions. *Applied Physics Letters.* 2005;86(11):1-10. DOI:10.1063/1.1880446

65. Galbiati M. Polariton condensation in photonic molecules. *Physical Review Letters*. 2012;108(12):126403. DOI:10.1103/PhysRevLett.108.126403

66. Abbarchi M, Amo A, Sala VG, Solnyshkov DD, et al. Macroscopic quantum self-trapping and Josephson oscillations of exciton-polaritons. *Nature Phys.* 2013;9:275. DOI:10.1038/nphys2609

67. Flayac H, Savona V. Unconventional photon blockade. *Physical Review A.* 2017;96(5):053810. DOI:10.1103/PhysRevA.96.053810

68. Johansson JR, Nation PD, Nori F. QuTiP: An open-source Python framework for the dynamics of open quantum systems. *Computer Physics Communications*. 2012;183(8):1760-1772. DOI:10.1016/j.cpc.2012.02.021

69. McCutcheon D, Dara PS. A general approach to quantum dynamics using a variational master equation: Application to phonon-damped Rabi rotations in quantum dots. *Physical Review B.* 2011;84(8):081305. DOI:10.1103/PhysRevB.84.081305

70. Ohadi H, Gregory RL, Freegarde T, Rubo YG, et al. Nontrivial phase coupling in polariton multiplets. *Physics Review X*. 2016;6:031032. DOI:10.1103/ PhysRevX.6.031032

71. Rodriguez SRK, Casteels W, Storme F, et al. Probing a dissipative phase transition via dynamical optical hysteresis. *Physical Review Letters*. 2017;118(24):247402. DOI:10.1103/PhysRevLett.118.247402

72. Walls DF, Milburm GJ. *Quantum optics*. Dordreht: Springer Science and Business Media; 2007. 370 p.

73. Khudaiberganov T, Arakelian S. Quantum polariton trigger. *IOP Conference Series: Materials Science and Engineering*. 2020;896(1):12-26. DOI:10.1088/1757-899X/896/1/012126

74. Kharkova AV, Voznesenskaya AA, Kochuev DA, Khorkov KS. Influence of laser irradiation parameters on the temperature of the treated surface. *Izvestiya Rossiyskoy akademii nauk. Seriya fizicheskaya*. 2022;86(6):864-868. DOI:10.31857/S0367676522060151 (In Russ.)

75. Kharkova AV, Kochuev DA, Davidov NN. Laser synthesis of a weakly agglomerated aluminium oxide nanopowder doped with terbium and ytterbium. *Journal of Physics: Conference Series*. 2021;2131:052086. DOI:10.1088/1742-6596/2131/5/052086

76. Novikov IV, Krasnikov DV, Shestakova VS, Rogov IP, et al. Boosting CO-based synthesis of single-walled carbon nanotubes with hydrogen. *Chemical Engineering Journal*. 2023;476:146527. DOI:10.1016/ j.cej.2023.146527

77. Alferov ZhI, Aseev AL, Gaponov SV, Kopyev PS, et al. Nanomaterials and nanotechnologies. *Mikrosistemnaya tekhnika*. 2003;8:3-13. (In Russ.)

78. *Physicists have created a simple method for embedding two-dimensional nanostructures into microchips*. Available from: https://www.nanonewsnet.ru/news/2023/fiziki-sozdali-prostoi-metod-vstraivaniya-dvumernykh-nanostruktur-v-mikrochipy [Accessed 15 December 2023]. (In Russ.)

Information about the authors / Информация об авторах

Dmitry N. Bukharov, Senior Lecturer, Vladimir State University A.G. and N.G. Stoletovs, Vladimir, Russian Federation; ORCID 0000-0002-4536-8576; e-mail: bukharov@vlsu.ru

Timur A. Khudaiberganov, Assistant, Vladimir State University A.G. and N.G. Stoletovs, Vladimir, Russian Federation; ORCID 0000-0002-2008-7276; e-mail: thomasheisenberg@mail.ru

Alexey G. Tkachev, D. Sc. (Eng.), Professor, Head of the Department, Tambov State Technical University, Tambov, Russian Federation; ORCID 0000-0001-5099-9682; e-mail: nanotam@yandex.ru

Sergei M. Arakelian, D. Sc. (Phys. and Math.), Professor, Head of Department, Vladimir State University A.G. and N.G. Stoletovs, Vladimir, Russian Federation; ORCID 0000-0002-6323-7123; e-mail: arak@vlsu.ru

Бухаров Дмитрий Николаевич, старший преподаватель, Владимирский государственный университет им. А. Г. и Н. Г. Столетовых, Владимир, Российская Федерация; ORCID 0000-0002-4536-8576; e-mail: bukharov@vlsu.ru

Худайберганов Тимур Алиевич, ассистент, Владимирский государственный университет им. А. Г. и Н. Г. Столетовых, Владимир, Российская Федерация; ORCID 0000-0002-2008-7276; e-mail: thomasheisenberg@mail.ru

Ткачев Алексей Григорьевич, доктор технических наук, профессор, заведующий кафедрой, Тамбовский государственный технический университет, Тамбов, Российская Федерация; ORCID 0000-0001-5099-9682; e-mail: nanotam@yandex.ru

Аракелян Сергей Мартиросович, доктор физико-математических наук, профессор, заведующий кафедрой, Владимирский государственный университет им. А. Г. и Н. Г. Столетовых, Владимир, Российская Федерация; ORCID 0000-0002-6323-7123; e-mail: arak@vlsu.ru

Received 22 December 2023; Accepted 26 February 2024; Published 26 April 2024

Территория распространения – Российская Федерация, зарубежные страны
Distributed is the Russian Federation and foreign countries

Computer layout: Olga V. Mochalina, TSTU, Tambov, Russian Federation
Компьютерный дизайн и верстка: Мочалина О. В., ТГТУ, Тамбов, Россия

Оригинал-макет подготовлен в Издательском центре ФГБОУ ВО «ТГТУ»,
392032, Тамбовская обл., г. Тамбов, ул. Мичуринская, д. 112А

Подписано в печать 15.04.2024. Дата выхода в свет 26.04.2024.
Формат 60×90/8. Усл. печ. л. 9,38. Уч.-изд. л. 9,75. Тираж 100 экз. Цена свободная. Заказ № 012.
СМИ журнал “Journal of Advanced Materials and Technologies”
(Журнал современных материалов и технологий) выпуск 2024. Том 9, № 1